Biomechanical Analysis of a Novel Bioactive Dental Implant

Alexandre Varo Leal Salústio

Thesis to obtain the Master of Science Degree in

Biomedical Engineering

Supervisors: Prof. André Paulo Galvão de Castro

Prof. Paulo Rui Alves Alves Fernandes

Examination Committee

Chairperson: Prof. Maria Margarida Campos da Silveira

Supervisor: Prof. André Paulo Galvão de Castro

Members of the Committee: Prof. Célio Pina

Prof. Jorge Marinho

October 2019

Preface

The work presented in this thesis was performed at the Department of Mechanical Engineering of Instituto Superior Técnico (Lisboa, Portugal), during the period February-October 2019, under the supervision of Professor André Castro and Professor Paulo Fernandes.

Declaration

I declare that this document is an original work of my own authorship and that it fulfills all the requirements of the Code of Conduct and Good Practices of the Universidade de Lisboa.

Agradecimentos

A elaboração da presente dissertação contou com o apoio e supervisão dos Professores André Castro e Paulo Fernandes do Instituto Superior Técnico. A eles, deixo uma calorosa saudação e um profundo agradecimento por me terem acompanhado incondicionalmente ao longo deste desafio. Será sempre uma honra ter feito parte do Instituto Superior Técnico, e espero poder contribuir sempre para o despertar da curiosidade científica das gerações vindouras, replicando o que esta escola tem feito já há tantos anos.

O meu percurso académico foi dividido aguerridamente entre dois pólos geográficos vitais para o meu crescimento enquanto pessoa e engenheiro, Aveiro e Lisboa. Em cada um, cruzei-me com pessoas que, de centenas de maneiras diferentes, me moldaram até ao que sou hoje. Não faria sentido não lhes dedicar um espaço neste trabalho, que não tenho dúvidas ter sido fruto da minha dedicação e esforço, mas que foram sempre alimentadas pelos que me acompanham: ao Ricas, Carolina, Mãe e Pai, por constituírem a base certa para um desenvolvimento ambicioso e desafiante, e me lembrarem sempre que ter uma família com quem contar é uma realidade que quero levar para sempre, e o verdadeiro e mais eficaz laboratório moral; à Inês, que nunca me deixou esquecer a importância de se estar para alguém, e a sorte de ter alguém que está para nós, dando-me o privilégio de viver de perto seis anos da nossa vida, a contar; ao Sindicato do Crepe Congelado, por me enrijecer os vínculos aveirenses, e mostrar que a amizade não se faz de circunstância, mas de disponibilidade, autonomia, intimidade e respeito; aos Tugas pelo Mundo, que sem sombra de dúvida elevaram a fasquia intelectual e filosófica, e ao mesmo tempo convergiram para um grupo crucial para a definição das minhas ambições enquanto pessoa; ao Clã 25 ASM, por se ter intrometido como segunda escola, depois da família, e no qual produzi as memórias mais bonitas e saudosas; e a tantos outros, cuja amizade espero honrar sempre, embora não haja mais espaço aqui.

Por fim, uma palavra de apreço aos últimos conterrâneos que viram de perto, literalmente, o desenvolvimento desta dissertação. Às Scaffoldettes, vulgo Valentina, Mônica, Paulino, Real, Tiago, Rafa e Marta, um enorme abraço, por terem feito parte da sala 2.20, de onde saímos mais perto do tão esperado título de Engenheiro. Foi mais divertido e tranquilo por vossa causa.

Espero que esta dissertação seja uma reflexão de todo o meu caminho até hoje, mas sobretudo um prelúdio para uma vida também continuada de desafios, peripécias, obras e pessoas.

Abstract

Introduction: Dental implants are inserted into the jawbone to support a dental prosthesis in order to replace missing tooth. However, the sensory function of the mechanoreceptors originally located at the root is lost to the implantation surgery, which has been related to health complications and implant failure. A possible solution is the development of a smart implant with an integrated sensor that can read the bite forces.

Objectives: To analyze the relation between the stress distribution and magnitude at twelve points of interest within the implant-abutment interface (IAI) and the bite force angle and magnitude, in order to indicate which of these points are more suited to welcome the sensor.

Methods: Computer-aided design was used to produce a standard implant geometry, that was then imported into finite element software. The model underwent different loading conditions based on the physiology of mastication, and three different scalar stress outputs were measured and compared among the points of interest.

Results: On the one hand, the stress at the points from the top of the IAI was linearly related to the load angle and magnitude, with the most mesial and distal points having a distinctive, sensitive response. On the other hand, the points at the bottom exhibited poor linearity and weak sensitivity compared to the later.

Conclusion: The top of the IAI appears to be more adequate for the placement of the sensor. However, a more realistic geometry of bone and prosthesis is needed to reinforce the applicability of the study by improving the stress predictions.

Keywords: Dental Implant; Finite Element; Crown; Piezoelectric Sensor; Loading Conditions; Implant-abutment Interface; Von Mises; Internal Hex; Moment; Dynamic

Resumo

Introdução: Os implantes dentários são dispositivos médicos utilizados para substituir dentes naturais. A capacidade sensorial dos mecanorecetores originalmente localizados na raíz do dente é perdida após implantação, o que está associado a implicações na saúde e ao insucesso do implante. O desenvolvimento de um implante dentário inteligente com um sensor integrado capaz de medir as forças de oclusão dentárias é uma possível solução.

Objetivos: Analisar a relação entre a distribuição e magnitude das tensões em doze pontos de interesse da interface implante-pilar (IIP) e a direção e magnitude das forças de oclusão, de modo a indicar quais destes pontos é mais propício à introdução do sensor.

Métodos: Modelação geométrica e de elementos finitos de um implante dentário standard e simulação de diferentes condições de carregamento dentro dos limites fisiológicos. Três outputs escalares derivados de tensões foram avaliados e comparados entre os pontos de interesse.

Resultados: A tensão nos pontos da região superior da IIP variou linearmente com o ângulo e magnitude de carregamento, nomeadamente para os pontos nas faces mesiais e distais do implante. Por outro lado, os pontos pertencentes à região inferior demonstraram uma fraca linearidade e sensibilidade ao carregamento.

Conclusão: Prevê-se que a região superior da IIP seja a mais indicada para a localização do sensor. No entanto, uma modelação mais precisa do implante e dos tecidos envolventes é necessária para reforçar a aplicabilidade dos resultados e melhorar as previsões das tensões.

Palavras-chave: Implante Dentário; Elementos Finitos; Coroa; Sensor Piezoeléctrico; Condições Fronteira; Interface Implante-Pilar; Von Mises; Hex Interno; Momento; Dinâmico

Contents

List of Figures

List of Tables

Acronyms

AVGAC	Average absolute compressive
CAD	Computer-aided design
CT	Computed tomography
FE	Finite Element
IAI	Implant-abutment interface
ICP	Intercuspid position
MAXAP	Maximum absolute principal
MEMS	Microelectromechanical system
PL	Periodontal ligament
PMR	Periodontal mechanoreceptor
PSSA	Patient/site specific abutments
SENS	Stress sensitivity

Nomenclature

E	Elastic modulus
ν	Poisson ratio

Chapter 1

Introduction

Dental implants are medical components widely used to overcome edentulism. These structures are implanted into the jawbone and then support a superstructure such as a single crown prosthesis or a more complex bridge or denture to replace missing tooth. Dental implants have been reported with high success rates and good aesthetic and functional outcome in a continuously growing industry [1]. According to the American Academy of Implant Dentistry, the market for dental implants in the US and Europe combined was expected to be valued at more than 4 billion dollars in 2018, and about 500,000 people per year get an implant in the US [2]. However, after the surgical procedure is complete, issues related to anatomical and physiological differences between natural teeth and dental implants continue to move investigators towards the development of more biocompatible, mechanically able and aesthetic implants. An important clinical concern about tooth replacement is the loss of the sensorial ability to detect forces applied on the mouth, because the sensory feedback is done through mechanoreceptors in the periodontal ligaments which are removed during the implantation surgery. Subsequent failing oral proprioception is associated to several health conditions including central nervous system diseases such as Alzheimer and Parkinson, alterations in body posture, and implant overloading which ultimately results in excessive bone strain and consequently bone resorption [3].

1.1 Motivation

The restoration of the sensory function of the periodontal mechanoreceptors (PMRs) by dental implants has not yet been achieved on the market. Although some studies report the placement of sensors within the implant body [1], no evidence on the development of a force detector to be included into the implant, that reads the bite loads exerted on teeth during mastication or in other everyday activities such as speech, was found in literature or in several dental implant brands' websites. Thus, the establishment of a force nano or microsensor that reads these loads and then communicates with the nervous system through the same neural pathways as with PMRs, would represent a breakthrough in the implant dentistry field.

Recently, a study by Pereira *et al* [4] gave the first steps on the design of a prototype of the electronics of such a force sensor and the respective neural stimulation unit. Two separate electronic modules were engineered to convert electrical input from a piezoelectric sensor into discrete biocompatible electric signals, which in turn stimulate the superior and inferior alveolar branches of the trigeminal nerve, mimicking the real sensory pathway involving the PMRs. However, the loading conditions applied on the piezoelectric sensor in that study were ideal and simplistic.

Given that the mechanical environment within the implant during the application of forces is complex and might change brutally with varying force direction and magnitude, a biomechanical analysis of the implant may provide crucial data on the stress distribution, therefore aiding the design and choice of a proper sensor and its location within the implant.

In addition, dental implants are modeled in several different ways in literature, where material properties, loading and boundary conditions, and geometry of the implant and the surrounding tissues are not consensual, but selected accordingly to the objective of the analysis instead. Sometimes the dental implant is simulated without the prosthetic component and the loading conditions are applied to the abutment. Although some studies have alerted for the inaccuracy resulting from this simplification, a more profound numerical study might give precious insight on the real advantages and limitation of such simplification.

1.2 Objectives

The present work conducts a biomechanical study of a standard dental implant using finite element (FE) analysis. The stress behavior in the implant-abutment interface (IAI) is evaluated under several loading conditions and for two models, one including, and the other not including the crown. In summary, this work addresses two main objectives:

1. The main goal of this work was to analyze how different loading conditions affect the stress distribution and magnitude at two target regions of the IAI, in order to choose the most suited location to welcome a piezoelectric sensor.
2. The second goal was to study the influence of both the geometry of the implant system and occlusal area on the stress outcome.

1.2.1 Contributions

The main contributions of the present work to the scientific community, namely the field of structural computational modeling of dental implants are listed below.

1. Study of the relation between the stress magnitude at points of interest within the IAI and the load angle and magnitude.
2. Indication on the location of the piezoelectric sensors at the IAI and how to process and combine their electrical output in order to detect changes in the direction and magnitude of the bite forces.

1.3 Thesis Outline

The present work is divided into eight chapters, namely: “Introduction”, “Human Tooth Anatomy”, “Pressure Transducers”, “State of the Art”, “Methods”, “Validation of the FE Model”, “Results and Discussion” and “Conclusions and Future Work”.

“Introduction” is the first chapter, where the scope of the work is explained, along with its main objectives. Secondly, the “Human Tooth Anatomy” chapter provides relevant background on the anatomy and physiology of the tooth, and more specifically on the processes involved in the bite force transduction done by the PMRs, as well as on health conditions resulting from the failure of these processes. The third chapter, “Pressure Transducers”, reviews the types of pressure sensors and their working principles. In the fourth chapter, “State of the Art”, a thorough review on dental implants is done, followed by a review on finite element models of dental implants in literature. This chapter aims to both provide a comprehensive overlook on dental implant design options and their associated drawbacks and advantages, giving insight on the different approaches of their FE modelling. The succeeding fifth chapter, “Methods”, explains the creation of the model step by step, in the light of the previous chapter. It also includes the rationale for the selection of the target regions and their geometric description and context. The sixth chapter, “Validation of the FE Model”, includes both the convergence analysis and the validation of the model based on a previous *in silico* study. In the seventh chapter, “Results and Discussion”, the results from the stress analysis are shown, and the relation between stress and the load angle is discussed in detail. In the eighth and final chapter, “Conclusions and Future Work”, the most important results are presented, along with suggestions for future work required to continue the development of the smart dental implant.

Chapter 2

Anatomy of the Human Tooth

2.1 Teeth and the Stomatognathic System

The stomatognathic system can be defined as the combination of organs, structures, and nerves involved in speech and reception, mastication, and deglutition of food. It is composed of the teeth, the jaws, the masticatory muscles, the tongue, the lips, the surrounding tissues, and the nerves that control these structures [5]. Teeth intervene in each one of the mentioned processes, but they have a central role in mastication, as their different shapes allow a smart and sequential break down of food for posterior deglutition. A brief summary on tooth anatomy is carried out in the next two paragraphs, as well as an overview of the most important functional features of teeth.

Human teeth (Figure 2.1) are the hardest substance in the human body, and each tooth can be divided in three parts: the crown, which projects onto the mouth, the root, that descends into the jaw, and the neck, that connects the crown to the root. The crown surface is made of enamel, the white rock-hard mineral that is accounted for the teeth hardness. The interior of both crown and root is made of a less hard substance called dentin, which assembles microtubules that, when exposed to cold or heat after enamel loss, cause pain or sensitivity. The root is not covered by enamel, but by a layer of connective tissue, that binds it firmly to the gums and jawbone, called cementum. In turn, dentin is nourished by the pulp, which is the innermost portion of the tooth. The pulp consists of cells, tiny blood vessels, and a nerve, and is used to keep the tooth healthy and alert the organism to dangerous tooth injuries and infections [6]. Lastly, the periodontal ligaments (PLs) are a unique specialized connective tissue between the cementum covering the tooth root and the alveolar bone, being crucial to protect, support and provide sensory input for the masticatory system [7]. Although the internal morphology does not vary from tooth to tooth, they can be divided accordingly to their shape and location within the mouth into four groups: molars, premolar, canines and incisors (Figure 2.2). While molars assist in grinding and crushing food, canines and incisors help tearing and cutting, respectively [8]. Premolars are said to be transitional teeth, as they work to guide food from the anterior teeth to the back of the mouth. One might interpret premolars as hybrids between canines and molars, tearing and grinding food [9].

The PL was defined as the connective tissue between the root and the surrounding alveolar bone. Besides its supportive function, it also serves sensory and nutritive tasks. PMRs are the responsible behind the sensory feature of teeth, acting are extremely sensitive tactile sensors located among the collagen fibers of the PLs [10]. The last three paragraphs of this subchapter will focus on the role of PMRs in the signaling of mouth loads and its medical importance.

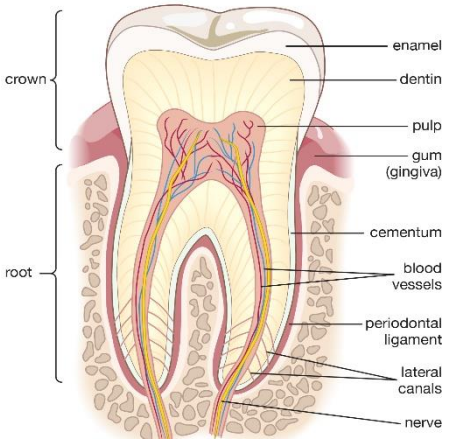

Figure 2.1. Tooth anatomy. Adapted from [6].

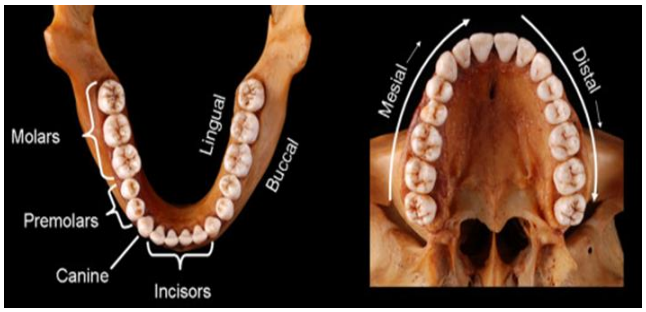

Figure 2.2. Features and directions of the dentition. Adapted from [7].

PMRs are located at the periodontal ligament, which is optimal for detecting functional loads on the teeth, and are involved in mechanotransduction and chewing motor control [11]. Three central purposes of PMRs are 1) to provide information about static jaw positions, 2) signaling forces applied to the teeth and 3) help the development of effective and strong masticatory muscles. The signaling process is dynamic and adaptive, which allows for the protection of the teeth and supporting tissues [12]. The goal of PMRs in mastication is to feed the brain with information about the direction and magnitude of the mastication loads and the information regarding spatial distribution and mechanical properties of the food. Thus, the chewing process is held dynamically and sequentially, from the initial perception of food texture and hardness to its break down into smaller pieces by cutting, tearing, crushing and grinding [13][14]. Each one of the 32 teeth that make a full dentition has PMRs, with posterior teeth (premolars and molars) having a decreased incidence of these receptors [10].

PMRs contact with the central nervous system through two neural pathways, that are illustrated in Figure 2.3 and 2.4: 1) pathways of the primary afferent neurons located in the mesencephalic nucleus of the trigeminal nerve leading to unconscious reflexes via the cerebellum; and 2) pathways of the primary afferents located in the trigeminal ganglion leading to conscious sensation, via the thalamus, to the cortical masticatory area [11]. In conclusion, PMRs in the periodontal ligament are the first structures to signal the loads exerted on teeth and are responsible to send that information to the brain, playing an important role in determining the magnitude, direction and point of application of forces used to hold and manipulate food between the teeth [10]. Thus, the medical importance of PMRs is straightforward.

. Clinical studies have observed that important sensory-motor functions in mastication are lost or impaired in patients whose PMRs were removed [10]. These patients seem to chew with a constant pattern throughout all the mastication sequence, oppositely to the dynamic and adaptative original mastication [11] and demonstrate a deviated jaw movement due to the

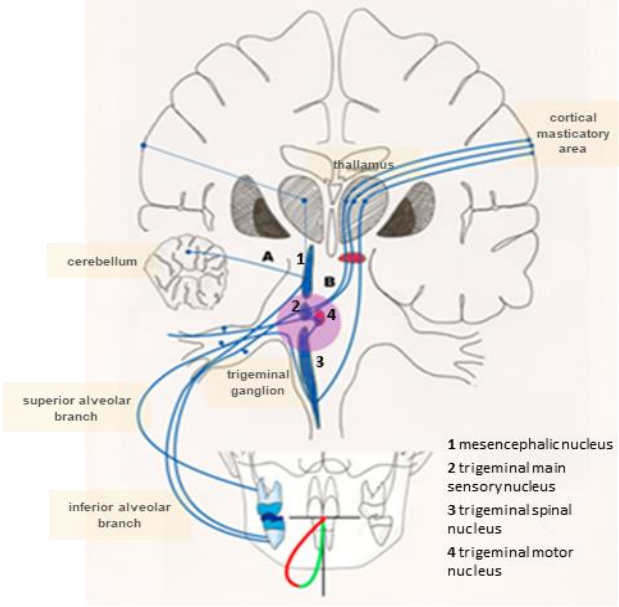

Figure 2.3. Pathways of the sensory inputs from PMRs to the central nervous system. A: via mesencephalic nucleus. B: via trigeminal ganglion to cortical masticatory area, Adapted from [11].

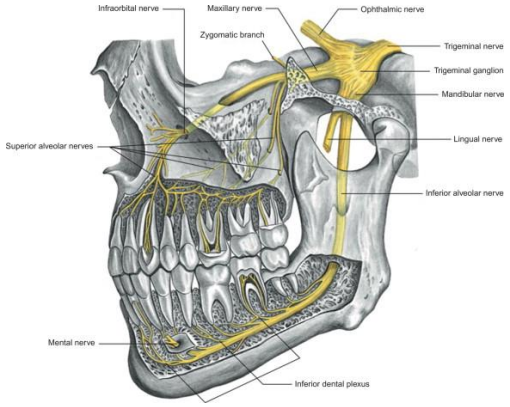

Figure 2.4. Anatomy of the trigeminal nerves. Superior and inferior alveolar branches and trigeminal ganglion are highlighted. Adapted from [15].

impairment [16]. The consequences are more significative when several adjacent teeth are replaced, which may severely limit the respective neural feedback pathways [16].

However, although major consequences are usually assigned to the loss of mastication control, other works studied the effects of a failing stomatognathic system on body posture. Changes in the mandibular position, which may result from changes in the periodontal afferents, might disturb the center of foot pressure[1], hence inducing variations in body posture [18]. Moreover, the reverse mechanism may also happen, and changes in the body posture can affect mandibular position. This alerts once more for the importance of the orofacial proprioception attained in part by PMRs. Tables 2.1.1 and 2.1.2 gather a couple of examples of mechanisms and events that are in some degree mediated by PMRs, as well as possible consequences of their absence.

2.2 Mastication and the Chewing Cycle

One may define mastication as the act of chewing food. It is the very beginning of digestion, having food broken down into progressively smaller pieces. During mastication, teeth are continuously separated and brought together, in a rhythmic and controlled pattern, which can be divided into an opening phase and a closing phase. These two phases together make up the so-called chewing cycle [23].

[1] The center of pressure is defined as the centroid of all the external forces acting on the plantar surface of the foot, and its movement has been used to identify balance control and foot function [17].

Table 2.1.1. Examples of mechanisms and events in which PMRs intervene.

[10] [11] [12]	Perception of the magnitude, direction, point of application and spacial distribution of the bite forces.
[10] [11] [12]	Reflex control of the masticatory system.
[17]	Regulation and adjustment of body posture.

Table 2.1.2. Health conditions that may arise from the absence or damaging of PMRs.

[19]	Absence of trigeminal nerve and cortical area stimulation can lead to dementia, stress and cognitive diseases.
[20]	Overloading due to lack of sensory feedback result in bone excessive strain, in turn causing remodelling deficit and bone loss.
[21]	Alzheimer, Parkinson, brain injury and stroke are commonly associated with tooth loss, periodontal diseases, dysphagia and impaired chewing function.
[22]	A splint induced change of the dental occlusion increases the symmetry of the running pattern.

Figure 2.5 shows the trajectory followed by the lower jaw during one cycle from the frontal view. The opening phase starts with the downward movement of the jaw. It then moves laterally from the midline as the closure phase commences. The closing phase starts with the crushing phase, in which food is trapped between the teeth, and the lateral displacement from the opening phase is lessened, as the lower jaw is moving upwards. The closing phase ends with a grinding

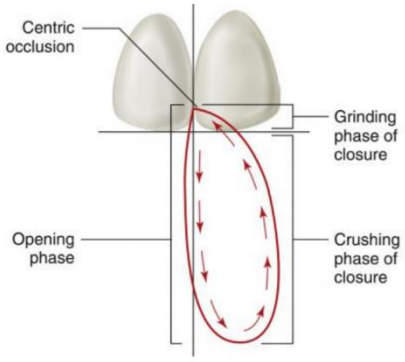

Figure 2.5. The chewing cycle (frontal view). Adapted from [23].

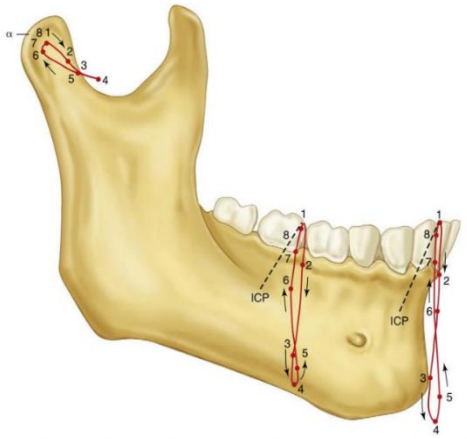

Figure 2.6. The chewing cycle on the working side of the jaw (sagittal view). Adapted from [23].

phase, which starts when teeth are just 3 mm apart and the jaw is displaced 3 to 4 mm from the midline. During the grinding phase, food is grinded and sheared, as the mandible is guided by the occlusal faces of the teeth, back to the midline position, often called intercuspid position (ICP). The chewing cycle in the sagittal plane (Figure 2.6) shows that the mandible moves slightly anteriorly during the opening phase, and then slightly posteriorly during the following closing phase, which in turn ends in an anterior movement back to the ICP. The chewing cycle has not always the shape of a tear as in Figure 2.5, nor it does consistently follow the sagittal trajectory depicted in Figure 2.6. Factors such as the hardness and size of the food may alter the chewing cycle curve to a broader or narrower one. Individual-specific anatomy of the teeth and jaw may also change the cycle significantly, as tall cusps and deep fossae promote a more vertical cycle, whereas flattened or worn teeth will promote a wider cycle. Furthermore, although most observed individuals have a preferred side where the closing phase occurs (left or right), mastication can happen bilaterally, alternating from one side to another [23].

Whether teeth contact directly with each other during mastication or not is uncertain. Some studies speculate that neurofeedback prohibits such contact, while others state that tooth contact increases as the food is broken down though the forces are minimal. Nonetheless, understanding the resting occlusal contacts among teeth may help identify to which regions or points of the crown will the mastication forces be applied. Figure 2.7a shows the typical contact areas among molar and premolar teeth and Figure 2.7b illustrates the first premolars contact. As these areas may change from individual to individual, it is important not to take these examples strictly [23].

The maximal biting force also varies from individual to individual, but males usually can bite stronger that females (Table 2.2). On the other hand, the maximal force that can be applied to a molar is significantly (three to four times) bigger than that which can be applied to an incisor. Moreover, it has also been demonstrated that the maximal biting force can be increased with practice and exercise, such that a person with a diet based on tough food will develop a stronger biting force. Even so, the forces involved in everyday mastication do not correspond to the maximal biting force. The amount of force placed on teeth during mastication is another parameter

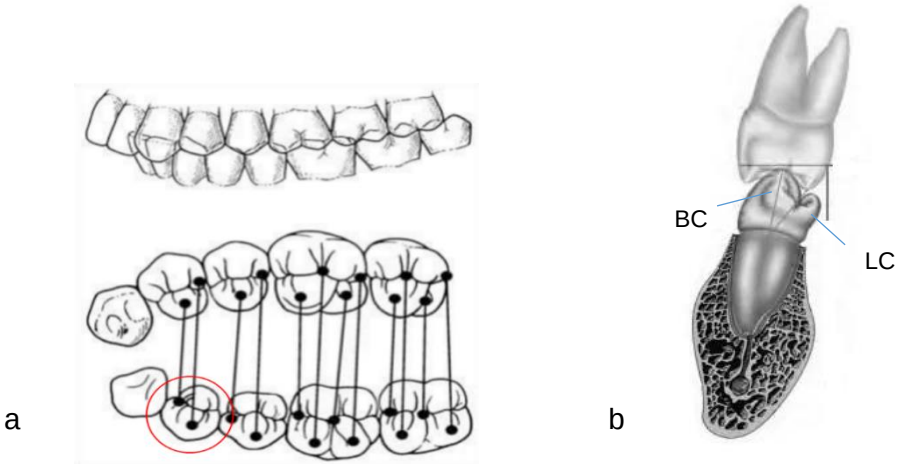

Figure 2.7. Dental occlusion. (a) Buccal and occlusal views of typical contact areas. Black dots indicate contact areas. The mandibular first premolar is highlighted. (b) Lower and upper first premolars. BC – buccal cusp. LC – lingual cusp. Adapted from [23].

that varies from individual to individual and depends on the food. Nonetheless, during mastication the greatest amount of force is placed at the posterior teeth. Table 2.3 shows literature reports for mastication loads at the first molar.

Table 2.2. Men and women maximal biting force.

Reference	Genre	Magnitude (N)
[23]	Female	351 – 440
	Male	526 – 632
[24]	Female	315
	Male	505
[25]	Female	553
	Male	652
[26]	Female	380.2 – 583.1
	Male	732.3 – 823.2

Table 2.3. Mastication loads for different food.

Reference	Food	Magnitude (N)
[27]	Biscuit	39 – 59
[28]	Peanuts	39
	Raisins	64
	Coconut	44
[29]	Meat	71 – 114
	Carrot	118 – 134
	Biscuit	112 – 146
[30]	Various	261

2.3 Relevant topics for the FE modeling

Although this work does not model the natural tooth, basic understanding on its physiological behavior under mechanical loading allows for an insightful modeling of the implant towards a simulation that is as faithful as it can be. Therefore, several features presented on this chapter that should include the computational model are summarized below.

PMRs are lost to the implantation surgery and their original role of sensing the loads exerted on the teeth is no longer active. Consequently, the sensor should be equally able to detect changes in the direction and magnitude of the bite force.

The crown of the mandibular premolar is composed of a protruding buccal cusp and a smaller lingual cusp, separated by a ridge that starts at the mesial fossa and ends at the distal fossa. The buccal cusp and both the fossae are part of the functional occlusion contact areas.

Although the mastication cycle can be ideally described by well-defined curves dictating the movement of the lower jaw and the occlusal surfaces can be roughly estimated, the enormous variability introduced by a set of factors such as the hardness of the food, age and genre, among others, calls into question the generality of these parameters. Thus, the study should include a large range of loading directions and magnitudes within the functional limits on Tables 2 and 3, in order to ensure the repeatability and representativeness of the results and conclusions.

Chapter 3

State of the Art

3.1 Dental Implants

A dental implant (Figure 3.1) is an artificial tooth that is inserted into the jawbone of the patient. It anchors dentures and orthodontic appliances, acting as a substitute of the natural tooth root and crown. Implants are screwed or plugged into the jawbone, and later combine with the surrounding bone to form a solid, load-bearing support unit, in a process called osseointegration – direct and functional linkage of the implant surface and the surrounding bone. A successful implantation is characterized by a clinical, solid, pain- and inflammation-free implant without any signs of peri-implant bone loss. Criteria for determining the implantation success include implant mobility, pain and bone loss; bleeding and suppuration at the tissue level; adequate function and aesthetics over a five-year period; and comfort, global satisfaction and ability to chew of the patient [32]. Factors that affect success include implant design and material, bone quality and quantity, and the implant loading conditions [33]. Nevertheless, dental implants are considered to have revolutionized dentistry due to their high success rate in replacing missing and damaged teeth and remain one of the most chosen approaches to overcome edentulism [34]. This sub-chapter aims to review the current implant design options, as well as the most commonly used materials, and their advantages and disadvantages concerning the just mentioned success criteria.

3.1.1 Implant body design

Most implants consist of three parts (Figure 3.1): the implant body (also called implant), which is the structure buried in the jawbone; the abutment, that connects the implant to the prosthesis, which in turn is the structure projected into the oral cavity. The abutment is usually

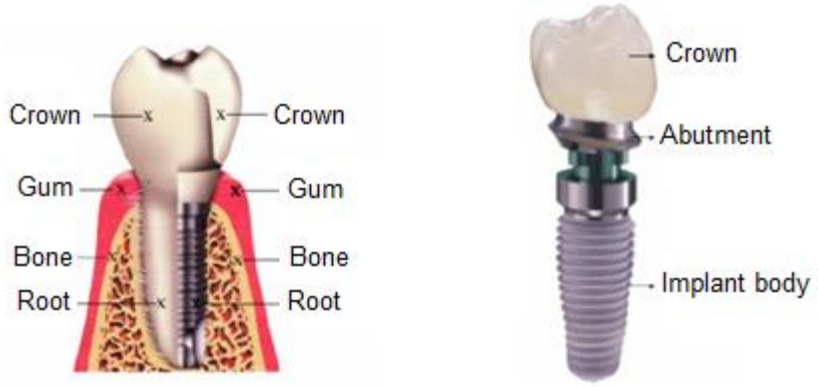

Figure 3.1. Basic structure of a dental implant. (left) Comparison between natural tooth and implant inside bone. (right) The prosthesis is attached to the implant body through an abutment. Adapted from [31].

connected to the implant by a screw. These three parts resemble the root, neck and crown of a natural tooth [35]. The evolution of implants has been made by continuously reinventing each one of its constitutive parts. Re-thinking their design by introducing new features or by adjusting the current parameters that set the geometry of the implant is crucial for progress and for the increase of implant success. Below, a review on different types of implant bodies is carried out, as well as the advantages and limitations of each design option.

Dental implants can be one- or two-piece implants (multi-piece implants with more than two pieces do also exist but are not considered in this review as the one- and two-piece implants are commonly used). One-piece implants, as the name suggests, are formed as a single solid unit. In this case, there is no screw-joint between the implant and the abutment, as the implant and the abutment are manufactured as one piece (Figure 3.2a). On the other hand, two-piece implants consist of an implant to which an abutment is connected, usually, with a screw (Figure 3.2b). One-piece implants are installed with one-stage protocols, whereas two-piece implants may be installed either via one-or two-stage protocols [34]. In two-stage protocol the implant is placed just below the cortical bone and covered with a cover screw in the first surgery. After that, a 3 to 6 months healing period is advised for osseointegration to take place, keeping the implant mechanically unloaded. Then, a second surgery uncovers the implant, the cover screw is withdrawn, and the abutment is inserted and connected to the already integrated implant. The prosthesis is later screwed or cemented onto the abutment. On the other hand, one-stage protocol requires only one surgery, and the implant does not undergo the healing period, as the abutment and prosthesis are immediately placed. The necessity of undergoing the healing period is still a controversial topic. While some studies support that early loading of implants is undesired as it can cause the formation of harmful fibrous tissue between the bone and the implant, others report that immediate loading may induce the formation of more resistive bone [38].

One of the advantages of one-piece implants is the prevention of screw-loosening, which is a limitation of two-piece implants, because micro-motions between the abutment and the implant might occur and cause dangerous fracturing. Other advantage is the reduction of surgeries to one and earlier aesthetic restoration [34]. A major limitation of one-piece implants is that they are not as customizable as two-piece implants. There are two types of customizable abutments: stock

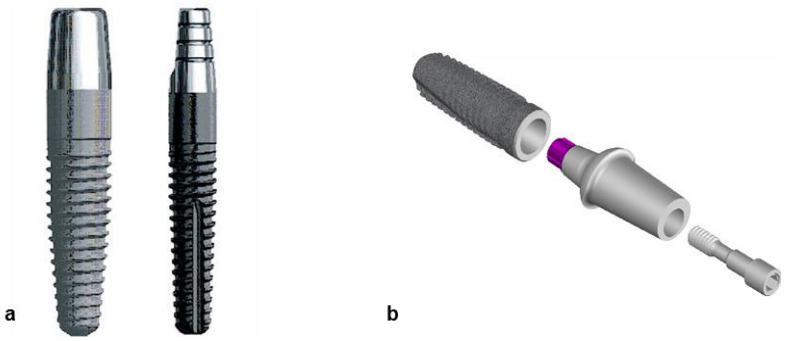

Figure 4.2. Comparison between one-piece and two-piece implants. (a) One-piece implant (Nobel Direct, Nobel Biocare). Adapted from [36] (b) Two-piece implants consist of the implant body, abutment and fixation screw, from *left* to *right*. Adapted from [37].

abutments and patient/site specific abutments (PSSA). Whereas stock abutments are customized via milling processes, drilling out undesired material in the abutment, PSSA are designed and created for a specific implant patient/site from scratch. One-piece implants only allow stock abutments from these two, and because the abutment is part of the implant, milling must be done in the mouth of the patient. Two-piece implants may be added the abutments after the milling is done in a more controlled and safe space such as a laboratory. Moreover, they also allow a choice between the two types of customizable abutments. Nevertheless, one-piece implants could be produced with the same diversity as that of PSSA, although it would be more difficult and expensive[2] [39].

Dental implants are also categorized according to the presence or absence of threads, their shape/outline and the existence of additional macro-irregularities to accentuate or replace the effect of threads [32]. Furthermore, dental implants can have hollow or solid bodies [34]. These design options are reviewed on the paragraphs below.

Nowadays many implant body designs are available: cylinder, press-fit, screw or a combination (Figure 3.3). Cylinder implants are non-threaded and rely on surface microdesign to stay attached to bone through friction [33]. Press-fit implants are usually non-threaded and the fixation into bone relies on the implant diameter being larger than the hole diameter, thus pressure is responsible for their attachment [40]. They were both commonly used in the 1980s because they involved less risk of mechanical failure, due to their positive response to high insertion pressure, that otherwise can lead to bone pressure necrosis. However, fatigue overload and harmful shear loads ultimately resulted in decreased bone-implant contact and a higher chance of failure [33]. The introduction of threaded implants has shown to lessen marginal bone loss and increase bone-implant contact [41] and reduce bone-implant sliding distance [42].

Figure 4.3. Types of implants according to the presence or absence of threads. Implants (a) and (b) are non-threaded cylindrical implants; (c) and (d) are threaded (or screw) implants; and (e) is a combination. Adapted from [43].

[2] Proper abutment customization can be selected after the implant is inserted. Even if the one-piece customized implant is chosen wisely via medical image, the outcome may not be as expected, and certainly harder to achieve than if the abutment is designed only after the implantation, as in the two-piece case [39].

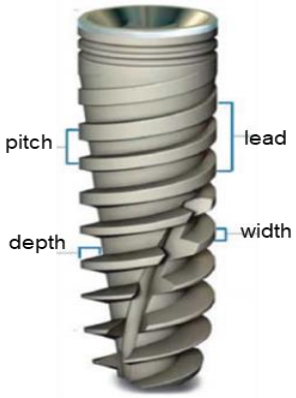

Figure 3.4. Geometric implant thread parameters. Adapted from [33].

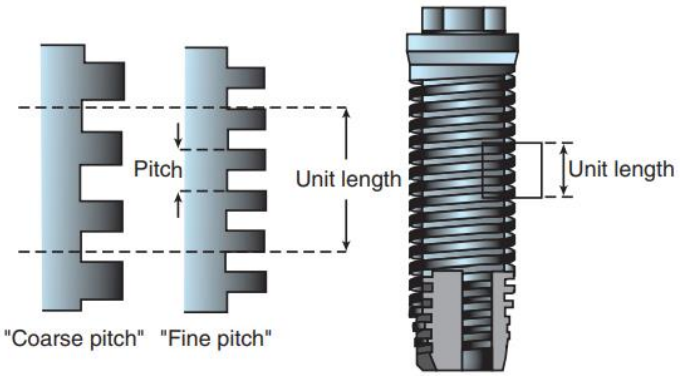

Figure 3.5. Thread pitch. The implant on the left has a larger thread pitch and thus less overall surface area compared to the implant on the right. Adapted from [43].

The rationale for the inclusion of threads in an implant lies on the maximization of initial fixation, enhancing surface area, and easing the dissipation of loads at the bone-implant interface, among others. Thread parameters include pitch, lead, shape, width and depth (Figure 3.4), and the variety of options/combinations by changing each one of these parameters has driven researchers to publish several comparative computational and clinical studies [43]. On the next paragraphs, these parameters are briefly explained along practical examples in the market.

The thread pitch (Figure 3.5) is the vertical distance between two adjacent threads and informs the number of threads per unit length; the smaller the pitch, the greater the number of threads. In turn, increasing the number of threads increases the surface contact area, which reduces the amount of stress after occlusal loading, an advantage in the case of weaker alveolar bone. For example, the pitch of the Straumann ITI implant is 1.5 mm, whereas a pitch of 0.6 mm can be found in Zimmer Screw-Vent or Biomet 3i implants [33].

The thread lead (Figure 3.6) is the axial distance that the implant advances in one revolution; in single-threaded implants, the lead is the same as the pitch, while in double-threaded implants, the lead is double the pitch, and so on. A double-threaded implant inserts twice as fast the single-thread implant. For instance, BioHorizons Maestro implant has a single thread lead whereas some Nobel BioCare implants are multi-threaded [33].

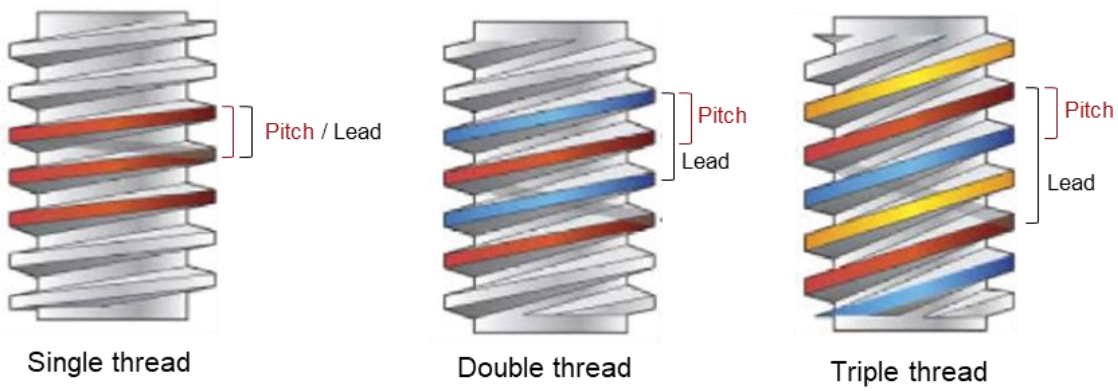

Figure 3.6. Pitch and lead of the thread. The lead is how much the implant advances in one complete revolution, whereas the pitch is the vertical distance between two consecutive threads. Adapted from [33].

The thread depth can be defined as the difference between the major and minor diameter of thread. On the other hand, the thread width is the thickness of the tip of a single thread. Increasing the thread depth increases the surface contact area. However, the deeper the thread depths, the harder it is for the surgeon to insert the implant, and therefore a less deep implant may be selected for the sake of an easier implantation. For example, the thread depth of Nobel Replace implant is 0.24 mm, whereas BioHorizons has a much deeper thread of 0.42 mm [33].

The thread shape (Figure 3.7) should allow the transfer of optimal favorable stresses to bone, while avoiding extremely high and low stresses which lead to bone resorption[3]. Current available thread shapes include V-shape, square shape, buttress, reverse buttress and spiral shape, being the V-shape the most common in industry (e.g., Nobel BioCare, Biomet, Zimmer, Astra) [41]. The face angle (Figure 3.8) is the angle between a face of a thread and a plane perpendicular to the long axis of the implant; it depends on the thread shape. The face angle changes the direction of the loads applied to the prosthesis to a different direction at the implant-bone interface [33]. As implants with square-shaped thread deliver less compressive and shear stress to the bone-implant interface, this design may be more benefic, and has been proven similar success rates in the upper and lower jaw, where bone density varies significantly [41].

In addition to the thread design, the implant dimensions are also a decisive factor in implant design, and they include the implant's length and diameter (Figure 3.9).

Selection of the length considers the available bone height, width and quality. Overall surface contact area and primary stability increase with length, but the increasing of functional surface area is more slowly as the forces are progressively weaker along the implant's length [34]. However, shorter implants can have a bigger functional surface area compared to longer implants if the thread shape is optimized, which recalls for the need of a careful selection of the thread design parameters [44]. Nevertheless, earlier studies show that short implants have higher failure

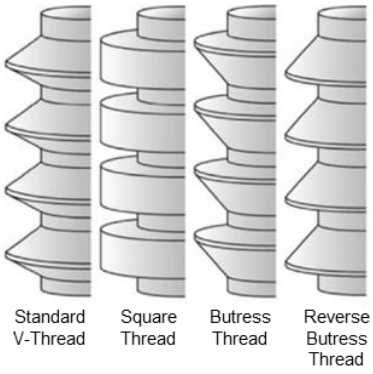

Figure 3.7. The four basic thread shapes for implant design. Adapted from [33]

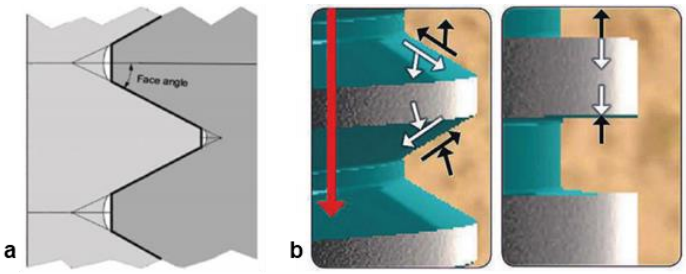

Figure 3.8. Face angle of implant threads. (a) The face angle is formed between the radial axis of the implant and the face of the thread. (b) Direction of forces at the implant-bone interface (black and white) resulting from axial loading (red). Adapted from [33].

[3] Bone is a dynamic tissue whose formation depends on the mechanical loading. It has been shown that extremely small or high stresses lead to bone loss [16].

rates than long implants [41][45]. Implants are classified as short- (6–9 mm), medium- (10–12 mm) and long- (13–18 mm) length implants [46].

On the other hand, the diameter of an implant is measured from the widest to the same point on the opposite side. Implants are classified as narrow- (when diameter is ≤ 3.75 mm), regular- (3.75–5 mm) or wide- (≥ 5 mm) diameter implants [34]. The selection of a suitable diameter depends on the available volume and quality of bone and on tooth type. Wide-diameter implants were introduced to overcome poor bone quality and inadequate bone height, because a larger diameter means an increased bone-implant contact, thus compensating for the lack of height or bone density at certain regions of the jaw. These restrictions usually associate to the posterior jaw, due to either bone resorption after the tooth loss or anatomic limitations. Moreover, the lower blood supply because of minimum existing alveolar bone may be a biological limitation for wide-diameter implants. In contrast, narrower implants are chosen to replace narrower anterior teeth, or when the roots of adjacent teeth are converging and space is a limitation, however their usefulness is restricted by the associated increased fracture risk because of reduced mechanical stability [47]. Higher survival rates have been reported for wider implants [48][49], although those for narrower implants are shouting and could be increased with better implant design and with more practice from the operators [47].

Lastly, there is a class of implants named tapered implants, whose diameter decreases along the implant from the upper to the lower part. An advantage of cylindrical non-threaded tapered implants is that they transfer a component of the compressive load to the bone. The greater the taper, the greater the load delivery, protecting the bone from the lack of stress stimulation. However, the greater the taper, the less the overall surface area, which may undermine the primary stability. In contrast, tapering in threaded implants serves no functional loading delivery as the threads bear a great part of the loads themselves regardless of the taper angle. Moreover, the implant taper may result in higher stress in the crestal region [33]. Tapering

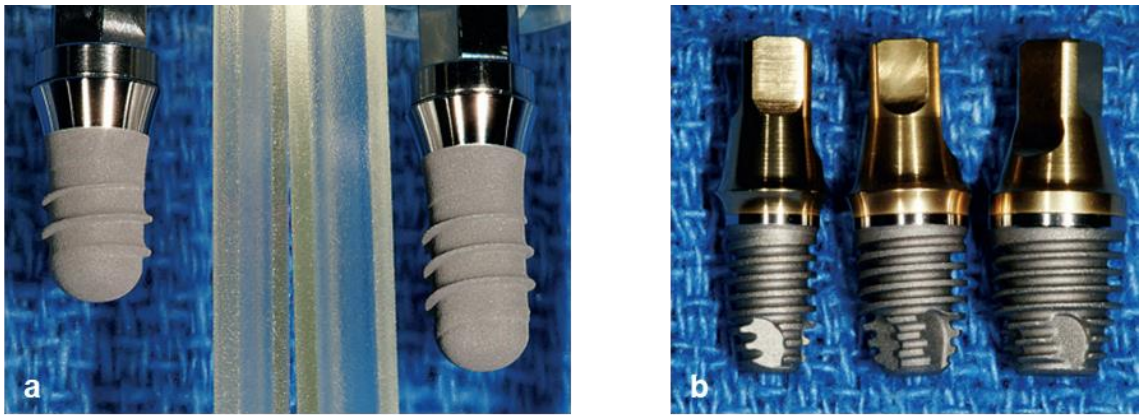

Figure 3.9. Example of implants with different dimensions. (a) The Straumann ITI implant on the left is 6 mm long, and the one on the right is 8 mm long; both implants have constant diameter. (b) The BioHorizons implants are 4, 5 and 6 mm in diameter, from *left* to *right*; the depth of the implant on the *left* is half that of the other two; these are examples of tapered implants, as it can be seen by the slightly decrease in diameter from top to bottom. Adapted from [43].

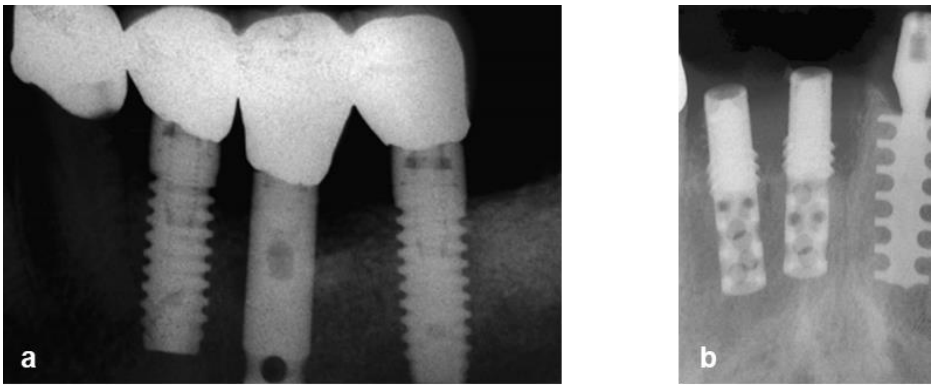

Figure 3.10. Dental implants X-ray images. (a) A hollow cylinder implant (*center*) was splinted to two solid screw implants (*left* and *right*). (b) Two hollow cylinder implants (*left* and *center*) were splinted to a solid plateau implant (*right*). In both cases, after several years, more crestal bone loss was observed on the hollow implants. Adapted from [43].

has a surgical purpose since it helps implantation [43]. Presently, tapered implants have very different taper angles, from 5.4 degrees (Ankylos Implant System) to 60 degrees (Trias Implant System) [50], although some studies discourage taper angles bigger than 30 degrees [43].

Finally, implants categorize as solid or hollow implants (Figure 3.10). Solid implants are compact whereas hollow implants include larger anchoring or contact area due to transverse openings in the walls. Preparing the implant bed is less harmful to bone in hollow implants than in solid bodies. However, implant mobility and peri-implant bone loss have been reported to hollow implants [51]. Moreover, they are more susceptible to mechanical failure, and the wall thickness of the implant body controls the resistance to fatigue [43]. Nonetheless, hollow implants have been proved stable and long-term support of mandibular overdentures [52], and can conduct bone regeneration into the inner architecture, improving stability and enhancing integrity [53].

3.1.2 Implant body materials

Implant materials must be biocompatible, have acceptable wear and corrosion resistance, strength and toughness. The implant design must be compatible with the mechanical and physical properties of its constitutive materials. Most implants today are made of metals and ceramics, and some components may incorporate polymers. Current available dental metals are titanium and its alloys, whereas gold and stainless steel, which are outdated in the implant body industry, may be used in abutments and prostheses. In ceramics, zirconia has been making its way into the industry, although the lack of clinical studies is a major retarding factor [46].

During the first decades of dental implant industry, titanium was the most commonly used material due its biocompatibility, resistance to corrosion, high strength, elasticity and low weight. Resistance to corrosion is given by an oxide layer, and depending on the oxygen content, titanium can be categorized into four grades I-IV: the higher the grade, the higher the oxygen content [34]. In addition, titanium-aluminum-vanadium alloy (Ti-6Al-4V) is the metallic biomaterial with the most attractive combination of biocompatibility, mechanical and physical properties. The stiffness of the four different grades is very similar (103 GPa), and that of Ti-6Al-4V is slightly higher (113

GPa). On the other hand, the alloy is four times stronger than grade I, and almost twice as strong as grade IV [43]. Drawbacks of titanium-based materials include the unaesthetic grayish color, the accumulation of titanium in the adjacent tissues (Figure 3.11) and galvanic side effects after contact with saliva [32]. The release of metallic ions from the titanium surface increases with the surface area, and may interfere with bone remodeling, ultimately leading to implant failure, or induce hypersensitivity in susceptible patients [34].

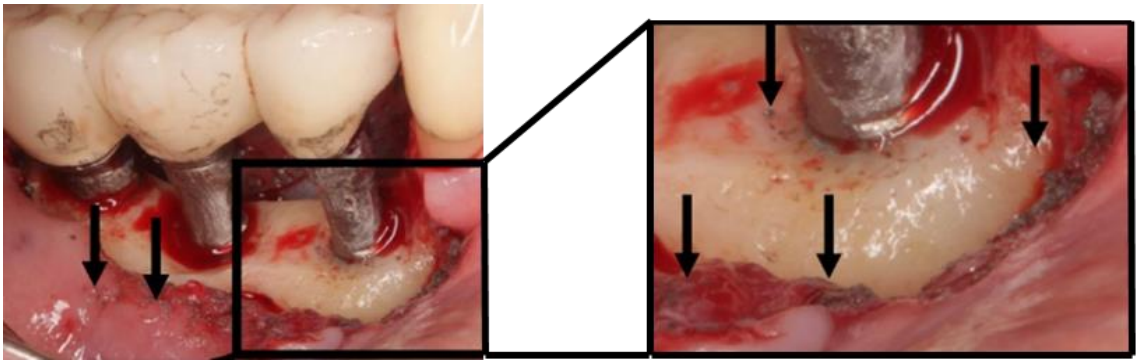

Figure 3.11. Example of titanium release in the peri-implant zone (black arrows). Among mechanisms causing titanium release are friction during implant insertion, corrosion of the implant surface, friction at the IAI and several detoxification methods. Adapted from [54].

The first ceramic implants, made from aluminum oxide (Al_2O_3), had frequent fracture incidences, which led to their substitution by titanium, despite the excellent biocompatibility and adhesion properties. Zirconia (ZrO_2) is a bioinert and non-resorbable metal oxide. It combines the biocompatible aspects of ceramics with metal mechanical properties such as high fracture toughness and bending strength, therefore making it a good alternative to titanium [32]. Moreover, zirconia demonstrates least particle release, the ability to transmit light, and has a tooth-like shading and color, allowing desirable aesthetics [46]. However, the lack of long-term studies on the outcome of ceramic dental implants remains their most important disadvantage [34]. More number of clinical investigations in the form of long-term performance of these implants are needed to truly evaluate their applicability [32][34]. Furthermore, the brittle nature of ceramics and susceptibility to failure in tension and shear may demand geometric designs that are not compatible with anatomical limitations. Also, its stiffness is similar to that of alumina, approximately 33 times as much as that of cortical bone, hence stress shielding may occur, resulting in bone loss and implant failure [43]. However, the fact must be told that zirconia holds great potential to rule the dental implant material industry, attending to the metal-free and aesthetic restorative demands of the patients, and it is presently used in abutments and crowns, giving their satisfactory clinical outcomes in these implant components [34].

3.1.3 Abutments

Abutments are the connective structures between the implant body and the superstructure. Their function is to support and retain fixed or removable prostheses, thus they must be able to

withstand great forces [32]. The abutment is mechanically attached to the implant and preferably should remain fixed throughout life of implant. In addition to that, bacterial leakage through IAI might occur and affect long term stability of the implant [55].

Classification of abutments is made according to two categories: 1) method of retention of prosthesis and 2) implant-abutment connection. Furthermore, they can be classified as straight and angled abutments, according to the axial deviation between the implant body and the abutment, and they can also be classified as stock or custom abutments [55]. An explanation on stock and custom abutments was done in the previous sub-chapter, hence it will not be carried out any further.

Regarding the retention method, abutments may use screws, cement or an attachment device such as magnet O-ring for removable prosthesis. Cement retained prosthesis are the most common due to several factors such as ease of fabrication and cost, passivity of the framework and retention is basically the same as those for natural teeth. Disadvantages of this method include cement dissolution, and low retrievability when the superstructure needs to be removed. In screw retained prosthesis, the screw is torqued to manufacturer's specifications, and the friction resistance developed between the internal threads of the implant and the fastening screw will provide the retention. Verification of precise fits is easier in screw retained restorations as a radiographic examination alone is required. Moreover, screw or cement retained restorations will affect occlusion differently: the area occupied by the access hole for screw retained prosthesis may be mechanically hazardous; in cement retained prostheses, occlusal contacts can be established and remain stable for long periods of time [55].

The implant-abutment connection can be classified as internal or external (Figure 3.12 and 3.13) [34]. The original external design of Branemark Nobel Pharma was merely meant to aid the implantation surgery, engaging the insertion tool, and allowing the implant to be threaded into the bone. Afterwards, the external feature was shown to provide an anti-rotational functionality and to fixate the abutment to one position in single tooth prostheses [43]. Presently, in internal connection systems, the apical part of the abutment is inserted into the implant body, whereas in external systems, a protrusion above the implant is inserted into the apical part of the abutment. The anti-rotational feature of the connection may have, among others, a hexagonal (hex), octagonal or cone-hex shape. Also, the connection usually has a screw but is sometimes screw-

Figure 3.12. Cross sectional view of external (*left*) and internal (*right*) implants. Adapted from [56]

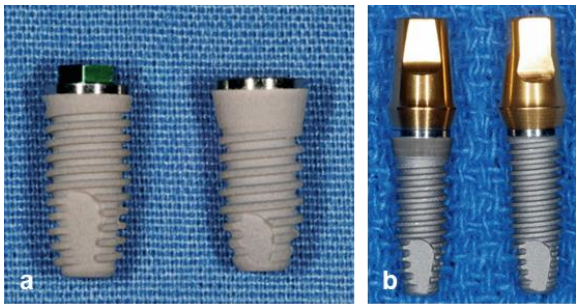

Figure 3.13. Comparison between external and internal implants (a) without abutment and (b) attached to the abutment . Adapted from [43].

less and relies entirely on the friction fit for its stability, such as Bicon dental implant [34]. The difference between the two connection systems is not visible once the abutment is attached (Figure 3.13). The deeper (higher) the internal (external) connection profile, the lesser the load applied to the attachment screw, and consequently the screw loosening is reduced. However, the profile of internal connections is usually deeper within the implant body compared to the height of external connections. Moreover, the larger the diameter at the crestal region, the larger the diameter of the connecting profile, corresponding to stress reduction to the abutment screw during lateral loading. As a matter of fact, the width at the implant-abutment interface is more critical to the stress applied to the screw than is the depth/height of the connecting profile [43]. Screw loosening was reported to be more frequent in external connections, because when the connection is internal, the loads are dissipated through the implant body, thus protecting the screw from the occlusal load [34]. Additionally, the geometry of the implant-abutment connection may affect the bacterial leakage into the internal region of the abutment and implant. External connections are reported to have higher amounts of leakage comparing to internal connections, and reduced amounts have been reported for conical internal connections, however this shape may not prevent abutment loosening completely, and thus allowing bacterial leakage as well [50]. Therefore, internal connections are widely used instead of external connections, although the original connection is available [55].

Sometimes, implant bodies cannot be placed with proper angulation due to either anatomic structures such as the mandibular nerve or the nasal sinus, or to the shape and angle of the alveolar process. Solutions for these problems lie on surgical intervention, repositioning or correcting these blocking structures. Another alternative is to place the implant regardless of the required angulation, and then use angled abutments to achieve the desired orientation. A wide range of pre-angled abutments are available, ranging from 15 degrees to 35 degrees (Figure 3.14). The main concern in using angled abutments is that original axial forces become shearing forces that bend the implant instead of just pushing it, which inherently increases stress at the surrounding bone tissue [55]. However, stress and strain due to angulation are reported to lie within physiological limit of bone [58]. Other study concluded that after a five-year period there

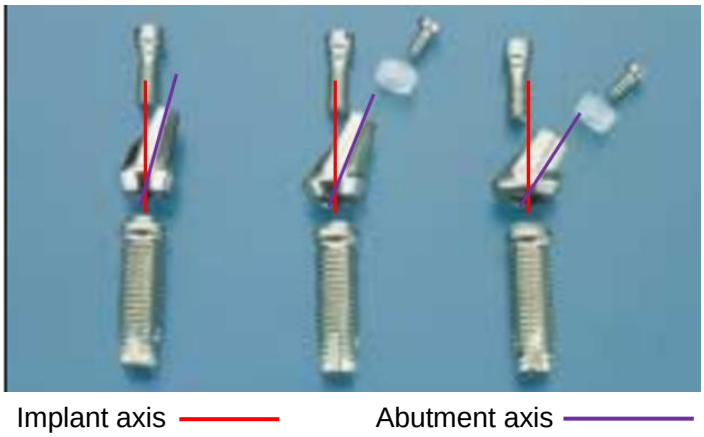

Figure 3.14. Implants with abutments with different angulations. From *left* to *right*, angulations of 15, 25 and 35 degrees. Adapted from [57].

was no difference in the survival rate of implants with angulated abutments ranging from 0 to 45 degrees [59].

The abutment can be made from different materials including alumina, titanium or zirconia. When selecting the material, the most important considerations are aesthetic aspects, fracture resistance and strength value [32]. In a study by Yildrim et al. (2003), zirconia abutments were reported fracture resistance values twice those for alumina. They also registered strength values 15% higher than anterior bite force, and flexion strength of zirconia abutments is greater or close to that of titanium [60]. Studies indicate that ceramic abutment failure is more frequent at the cervical region, near the IAI [32]. The screws which connect the abutment to the implant are usually titanium or gold. The last have smaller friction coefficient allowing them to be efficiently tighten without galling effect[4]. Nonetheless, screws are highly unaesthetic, although their gray or gold color can be softened by adding opaque composite materials, which this is not a concern in cement (screw-less) restorations [55].

3.1.4 Overview of the implant dentistry design

Tables 3.1, 3.2 and 3.3 present a structured summarized overview of this sub-chapter, highlighting the main points of the design of both the implant body and the abutment, and the materials which are commonly used in implant dentistry.

Table 3.1. Highlights of the dental implant materials.

Material	Highlights
Titanium	Corrosion and wear resistant. High strength and elasticity. Good biocompatibility and low weight. Poor aesthetics due to grayish color. Possibility of titanium release and accumulation in adjacent tissues.
Zirconia	Bioinert and biocompatible. High fracture toughness and bending strength. Excellent aesthetics due to light transmission and natural tooth color. Extremely high stiffness may lead to stress shielding. Needs long-term performance evaluation to be used in implant bodies.
Alumina/Gold	Outdated for implant body fabrication. Still used in abutments and crowns.

[4] Galling is a type of wear that occurs when materials that are compressed against one another are put into motion that causes friction. This can create heat sufficient to weld the materials together, which removes material from one material onto the other when they are separated.

Table 3.2. Highlights of the implant body design options.

Design	Highlights
One-piece	One-stage implantation requires less surgery time. Earlier aesthetic restoration. In-mouth customization is unpractical.
Two-piece	In two-stage implantation, the implant remains unloaded during the healing period. Abutment customization is far more convenient. When applicable, there may be screw loosening.
Hollow	Preparing the implant bed is less harmful to bone. Bone regeneration into the inner architecture improves stability and enhances integrity. Implant mobility and peri-implant bone loss are more probable than in solid. Increased susceptibility to mechanical failure and fatigue.
Non-threaded	Attachment to bone via friction or pressure. Positive response to high insertion pressure. Fatigue overload leads to decreased bone-implant contact and bone loss.
Threaded	Increased bone-implant contact and less marginal bone loss. Maximization of primary stability. Easing of force dissipation.
Pitch	The smaller the pitch, the greater the number of threads, and the greater the surface contact area.
Lead	The bigger the lead, the bigger the number of threads inserted in one implant revolution.
Depth	The deeper the thread, the greater the surface area. Deeper threads are harder to insert.
Shape	Allows the transfer of optimal favorable stresses to bone. Eases implantation and increases stability. The V-shaped thread is the standard.
Length	Functional surface area and primary stability increase with length. Short-length implants have bigger failure rates. Depends on the available bone volume and quality, and on anatomical limitations.
Diameter	Wide-diameter implants overcome poor bone quality and inadequate bone height. Narrow-diameter implants replace narrower anterior teeth and have higher failure risk. Tapered non-threaded implants increase delivery of compression load to bone. Depends on the available bone volume and quality, and on anatomical limitations.

Table 3.3. Highlights of the abutment design options.

Design	Highlights
Cement retained prosthesis	Most common. Ease of fabrication and low cost. Passivity of the framework. Concern for cement dissolution. Low retrievability.
Screw retained prosthesis	Easy precise fitting verification. Area occupied by screw hole may be mechanically hazardous.
External connection	Anti-rotational stability. The higher the profile, the lesser the load applied to the attachment screw. Higher amounts of bacterial leakage into the implant.
Internal connection	Anti-rotational stability. The higher the profile, the lesser the load applied to the attachment screw. Lower chance of screw loosening. Hexagonal profile is widely used.
Angulation	Allow correction of poor implant body inclination. Main concern is the transformation of axial forces in lateral shearing forces within the implant.
Stock Abutment	Customization (*e.g.* via milling) is done on a standard abutment. Milling is better performed in a safe, controlled space.
Patient/Site Specific Abutment	The abutment is prefabricated or specifically produced at the time.

3.2 FE modelling of Dental Implants

FE modelling is a numerical method for solving problems of engineering and mathematical physics. It is useful when leading with complicated geometries, loading conditions, and material properties, and analytical solutions cannot be obtained. This method has turned into an unquestionable valuable tool in the biomechanical field, being able to accurately estimate the impact of stress on implants. Axial and lateral loads lead to forces in different directions and moments across the implant. In this field, the way in which stresses are delivered to the surrounding tissues, such as bone, is a key factor for the success or failure of a dental implant. Therefore, many researchers use FE analysis to predict how stress is distributed within implants for different kinds of implant configurations and modelling sets [46].

The greatest obstacle in FE analysis of implant systems is the accurate, faithful recreation of bone and setting the implant-bone interface. The unpredictability of bone's mechanical

behaviour and its structural complexity led researchers to carry out assorted simulations, where differences in material properties, geometry and boundary conditions are undoubtably impactful [46].

In this sub-chapter, a review on the FE modelling of dental implants is carried out, highlighting the implant and bone geometries considered in several studies, as well as their material properties, loads and boundary conditions, surface interactions and meshes.

3.2.1 Geometry

2D models are adopted assuming axial symmetry of loads and geometry. Studies using 2D representation claim that even under this simplification, reasonable insight into the behaviour of the implant-bone system can be achieved. Nevertheless, mechanical behaviour predictions via a 2D model are less accurate than those predicted by the homologue 3D model [61].

FE modelling begins with the portrayal of the implant-bone geometry, which is a vital step of the global procedure, and the features of the model should resemble the physical properties of the original as faithfully as possible. Capturing the detailed properties of living structures such as bone is far more complex than recreating the standardized and regular non-living structures such as implants [62].

Portions of the mandible or maxilla, maxillary sinus region, and temporomandibular joint are the most common anatomical areas used in studies related to implantology [61]. In some 2D studies [63][64], the bone is modelled as a rectangle with the implant. Mandible is also simplified into an arch with rectangular cross-section in some 3D studies [65][66]. Since the 2000s, with the development of imaging techniques, anatomically accurate models are possible to achieve easily, including the direct transformation from 2D to 3D information in image data from computer tomography (CT) or MRI into FE meshes using specialized software [67]. Moreover, specifications from chapters of detailed anatomy books may also be used to obtain realistic models [61]. Figures 3.15 and 3.16 show some examples of 2D and 3D geometries used in literature.

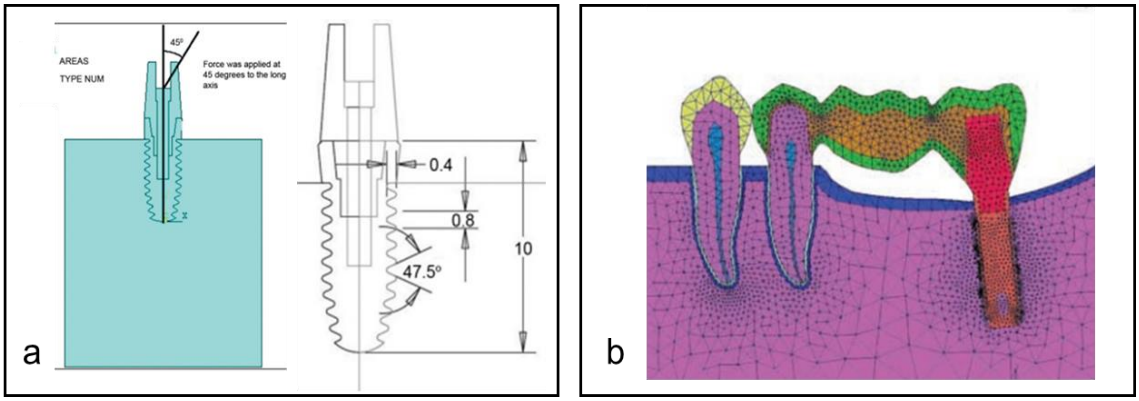

Figure 3.15. 2D geometries from two FE studies of dental implants. (a) Model from Desai et al. (2012). (b) Model from Ozçelik et al. (2007).

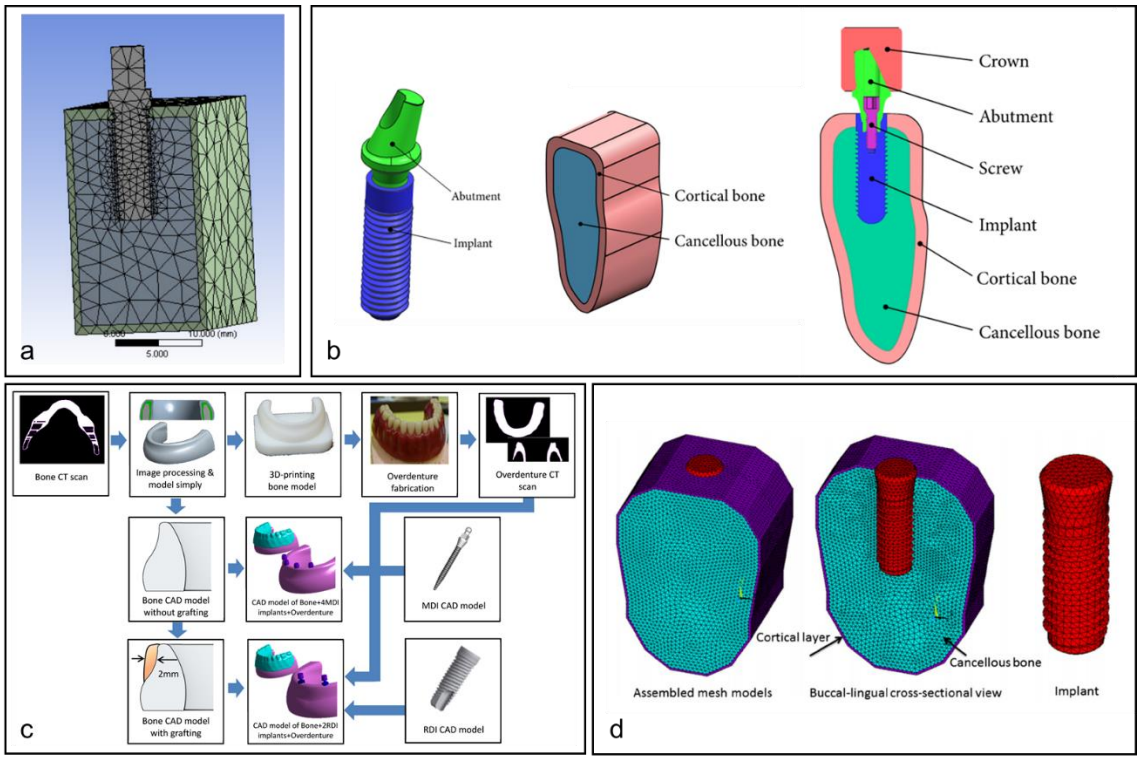

Figure 3.16. 3D geometries from four FE studies of dental implants. (a) Model from NarendraKumar et al. (2018). (b) Model from Zhang et al. (2016). (c) Model flow-chart from Chang et al. (2016). (d) Model from Chou et al. (2014).

To model the implant system, one way is to acquire all the geometric data such as length, diameter, thread design, among others, from the manufacturer. The alternative is to scan the structures and reconstruct them digitally. Either way, a realistic and efficient model may be obtained [62] (Table 3.4). The prosthetic device can be modelled after anatomy books or according to treatment protocols. A simpler option is to treat the superstructure as a rectangle; however, this may interfere with the accuracy of the model [62]. The geometry of the implant and the quality of bone are determinant in the survival rate of the implant. Variations on the geometry can have great impact on the mechanical behaviour of the implant under stress. Modelling assumptions and software limitations might have led to inaccuracies over the years [61]. However, although the usefulness of simplified FE models to obtain accurate absolute results or to compare with other studies is debatable, they can be used in qualitative studies whose objective is to analyse the stress distribution for different loading conditions and geometry parameters [62].

3.2.2 Material properties

The Young modulus (E) and Poisson ratio (v) are commonly used mechanical quantities to describe the mechanical behavior of materials. Whereas Young's modulus, also called elastic modulus, measures the stiffness of an elastic material, the Poisson's ratio is the ratio of the contraction or transverse strain, perpendicular to the applied load. The higher the elastic modulus, the stiffer the material; the higher the Poisson's ratio, the higher the deformation [62].

Table 3.4. Dental implants and bone geometry reference in FE modelling.

Reference	FE Model	Geometry Reference
[68]	Implants embedded in a bone block	CAD: bone block with a cortical layer and cancellous layer was constructed by CAD
[69]	Implants embedded in normal maxilla and cleft maxilla	CT and CAD: CT from a dry skull; palatal cleft, alveolar cleft and complete cleft were designed by computer
[70]	Three-unit bridge fixed prosthesis supported by an implant and a natural tooth, with an adjacent tooth and surrounding bone	CAD: a bone section (2D) was constructed by CAD with a cortical layer and cancellous bone and PDL
[71]	Implant embedded in mandible (cortical and cancellous bone), crown, teeth	CT: in vivo CT of a segment of mandible
[72]	Implant embedded in mandibular right first molar area	CAD: a bone block with a cortical layer and cancellous layer was constructed by CAD
[73]	Implant and abutment together embedded in bovine bone	CT: scan of the models used for the experiment (implant embedded in bovine bone)
[74]	Eight types of implants embedded in bone	CAD: 2D model of the bone block based on a cross-sectional image of the human mandible; and the implants.
[75]	Implant embedded in a bone block	CAD: a bone block with a cortical layer and a cancellous layer was constructed by CAD
[76]	A section of mandible and implant	CT data and 2D FE model used in previous study
[77]	Bone section with embedded implant and prosthesis (metal coping and porcelain), screws	CT: in vitro model (resin bone)
[78]	Dental implant embedded in bone	CAD: create the implant; CT and CAD: reconstruction of mandible
[79]	Ball attachment overdenture (mandible implant and attachment, mucosa and denture)	CT: from a single human mandible (edentulous 65-year-old woman); CAD: implants
[80]	Dental implant placed over mandibular bone,	CT and CAD: mandible was constructed by CAD with aid from a CT image

The material properties have a great impact on the stress distribution in a structure. These properties can be modelled as isotropic (the material properties are the same in all directions) and anisotropic (these properties vary with direction) [61].

Isotropic properties are used widely in FE modelling studies related to implant dentistry, whether for implant materials or for living structures [61][62][67][81]. However, in contrast with non-living structures, bone is hardly homogeneous or linear [61][62][67]. Bone has different values for ultimate strain and elastic modulus when tested experimentally in different directions [67]. Moreover, bone's density is non-uniform, which may also affect the stress distribution. In order to develop more realistic models, more complex studies may acquire the density distribution with aid of advanced data from CT scans, for example [62].

The biomechanical properties of the non-living structures that make the implant are different from the original tissues. The design and production of more adequate and efficient biomaterials is an everyday challenge which will persist in the future [61]. The gold standard material for implants is titanium and its alloys, although the study and use of bio-ceramic materials is growing, as stated in the previous sub-chapter [61].

The major drawback in selecting the material properties is the wide range in literature for Young modulus and Poisson ratio. These differences arise from the fact that the test conditions affect greatly the material property measured [61][67]. For instance, the Young modulus for titanium has been taken from 102 to 114 GPa, and the Poisson ration between 0.29 and 0.25 [61].

In Table 3.5 a selection of nine studies and their chosen material properties is displayed. It is clear that some studies prefer the simpler isotropic approach, while others consider the anisotropy of bone. Furthermore, bone density is also contemplated in fewer studies, where trabecular bone is divided into low- and high- density trabecular bone.

3.2.3 Boundary Conditions

Boundary conditions are applied to regions where the displacements and/or rotations are known. The constraints may be fixed type or allow non-zero specific displacements and/or rotations. These conditions limit the number of degrees of freedom, that is, the directions in which motion is possible. In FE studies, zero-displacement constraints must be applied to some boundaries of the model in order to ensure equilibrium [62]. Ideally, the entire jawbone structure should be modeled along with ligaments, muscles, tendons and other supporting tissue, so that the forces applied to the bone surrounding the implant are also considered [61][81]. Zhou *et al*. simulated the functions of the muscles of mastication and the ligaments involved in the temporomandibular joints by means of cable and compressive gap elements [91]. This, however, is not a practical approach, and most FE studies have only considered a small part of the jawbone surrounding the implant, while keeping the model accurate enough to generate correct information [61][81].

Table 3.5. Material properties in literature. Nine studies were reviewed. Some studies consider the anisotropy or orthotropy of bone (shear modulus not shown). Other studies divide cancellous bone into high- and low-density cancellous bone.

Reference	Part (material)	*E* (MPa)	*v*
[82]	Cortical bone	13 000	0.3
	High-density cancellous bone	1 370	0.3
	Low-density cancellous bone	800	0.3
	Implant, abutment and screw (titanium)	102 000	0.3
	Crown (gold alloy)	95 000	0.3
[83]	Cortical bone	14 700	0.3
	Cancellous bone	490	0.3
	Implant, abutment and screw (Ti-6Al-4V)	114 000	0.34
	Crown (porcelain)	96 000	0.25
[84]	Cortical bone	E_x = 12 700 E_y = 17 900 E_z = 22 800	V_{xy} = 0.18 V_{yz} = 0.28 V_{xz} = 0.31
	Cancellous bone	E_x = 210 $E_y = E_z$ = 1 148	$V_{xy} = V_{xz}$ = 0.055 V_{yz} = 0.322
	Implant, abutment and screw (titanium)	110 000	0.35
	Crown (porcelain)	68 900	0.28
[85]	Cortical bone	$E_x = E_y$ = 12 600 E_z = 19 400	V_{xy} = 0.300 $V_{yz} = V_{xz}$ = 0.253
	High-density cancellous bone	E_x = 1 148 E_y = 210 E_z = 1 148	V_{xy} = 0.05 V_{yz} = 0.32 V_{xz} = 0.01
	Low-density cancellous bone	$E_x = E_z$ = 230 E_y = 42	$V_{xy} = V_{xz}$ = 0.05 V_{yz} = 0.32
	Implant (titanium)	110 000	0.35
[86]	Cortical bone	14 500	0.33
	Cancellous bone	1 370	0.3
	Implant and abutment (titanium)	110 000	0.3
	Crown (Co-Cr alloy)	218 000	0.33
[87]	Cortical bone	13 700	0.26
	Cancellous bone	1 370	0.31
	Implant, abutment and screw (Ti-6Al-4V)	110 000	0.33
[88]	Cortical bone	14 700	0.3
	Cancellous bone	1 470	0.3
	Implant and abutment (Ti-6Al-4V)	113 800	0.342
[89]	Cortical bone	$E_x = E_y$ = 9 600 E_z = 17 800	V_{xy} = 0.55 $V_{yz} = V_{xz}$ = 0.30
	Cancellous bone	E_x = 144 E_y = 99 E_z = 344	V_{xy} = 0.23 V_{yz} = 0.11 V_{xz} = 0.13
	One-piece implant (zirconia)	205 000	0.3
	Crown (porcelain)	68 900	0.28
[90]	Cortical bone	13 700	0.3
	Cancellous bone	1 370	0.3
	Implant (titanium)	110 000	0.35
	Crown (feldspathic porcelain)	69 000	0.3

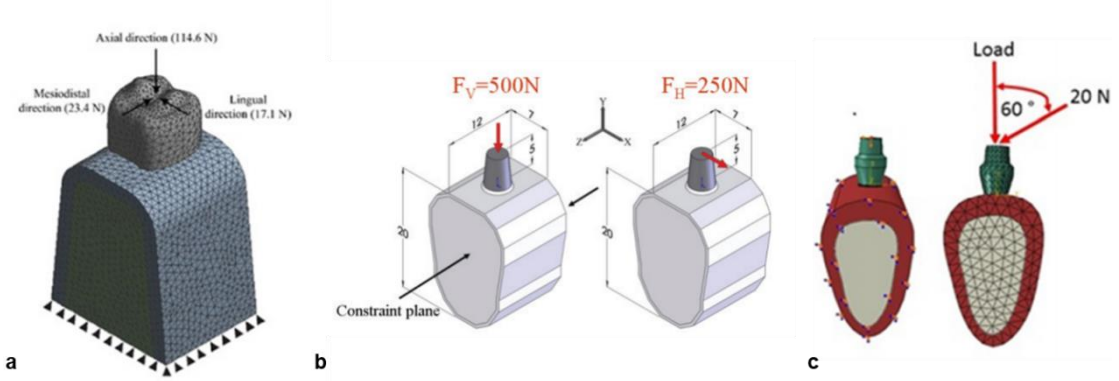

Figure 3.17. Three types of boundary conditions in literature. (a) Bone is fixed only at its bottom. Adapted from [89] (b) Bone is fixed laterally. Adapted from [72] (c) All exterior surface is fixed. Adapted from [88].

A good compromise between including the just mentioned boundary structures and considering solely the surrounding tissue, is to ensure that the constraints are placed far from the regions of interest, to prevent overlap of stress or strain fields arising from reaction forces at the boundary conditions' regions [62][81]. This can be achieved by expanding the domain of the model [62], or by using infinite elements [67]. In their paper on the evaluation of mandibular FE models with different lengths and elements, Teixeira *et al.* concluded that the stress distribution is similar for models with diameter greater than 4.2 mm [92].

In most FE studies of the mandible, the boundary conditions are set as fixed [62][67]. However, some studies may consider spring constraints as opposed to fixed constraints, thus allowing non-linear small displacements [61]. Moreover, if the model is axisymmetric, it can be resumed into a smaller portion, taking off one half of it, for example, and adjusting the loading conditions accordingly [62]. The bone may be fixed only at its bottom (Figure 3.17a), at its mesial and distal surfaces (Figure 3.17b), or all around (Figure 3.17c). In addition, in another study, both bone side plates were considered frictionless, but were allowed normal displacement [78].

3.2.4 Loading Conditions

In order generate a correct implant-bone behavior, it is essential to select realistic forces with meaningful magnitudes and directions. Bite forces can be compressive forces or shear forces. Shear forces tend to harm material integrity and increase stress [62]. Therefore, engineers should design implant-restoration systems that avoid transmitting unfavorable non-axial stresses to the implant body and bone [81].

In actual mastication, bite forces are highly dynamic, and different magnitudes and directions are applied depending on the food status in a cyclical pattern, as discussed in the second chapter. However, these randomized cyclic forces are not easily simulated [62]. In FE models, dynamic loading is occasionally considered. Figure 3.18 displays four different dynamic loading cases in literature. The axial component of the force is always present, and the lingual and mesiodistal components are also included depending on the study. The waveforms have the usual shapes of

squares, sines and triangles. The maximum axial force in these studies is about 120 N, and the mesiodistal and lingual components are about 22% and 16% of the axial component, respectively. Moreover, one or more cycles are simulated. However, as this approach is computationally demanding, most FE studies use static loads which, for realistic simulation, are combined oblique loads [81].

The magnitude of the biting forces depends on the genre, age, tooth and food, which results in many differences in literature. However, a common thought is that the magnitude of the maximum bite force depends on its direction [61]. As with magnitude, the direction of the oblique bite force is not consensual. In static mandible studies, some state that the force is being done in the buccal-lingual direction, while others refer the lingual-buccal direction. Moreover, if the prosthesis is not considered by the FE model, a bending moment should be applied together with the bite forces (Figure 3.19), caused by the original non-axial forces at different points of the restoration [80]. However, the inclusion of the restoration in the model is encouraged, in order to obtain more representative results [62][81]. Typical magnitudes for the premolar region are within 40–600 N, and angles to the longitudinal axis are within 0–45 degrees [81].

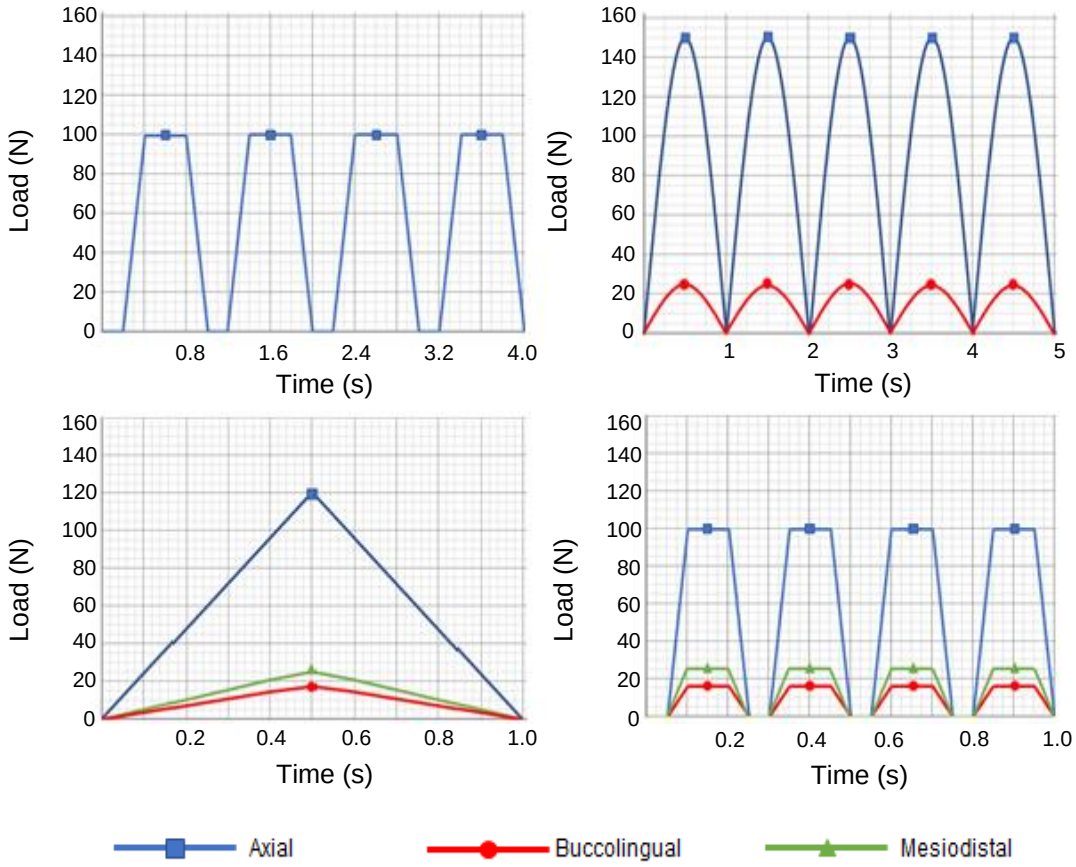

Figure 3.18. Dynamic loading conditions in literature. Maximum force – Mx, Waveform – Wv, Number of cycles – NCyc, Type I (axial), II (axial and lingual), III (axial, lingual and mesiodistal). (a) Mx = 100N, Wv trapezoid, NCyc = 4, Type I. Adapted from [93]; (b) Mx = 150N, Wv sine, NCyc = 5, Type II. Adapted from [94] (c) Mx = 120N, Wv triangle, NCyc = 1, Type III. Adapted from [95] (d) Mx = 100N, Wv trapezoid, NCyc = 4, Type III. Adapted from [96].

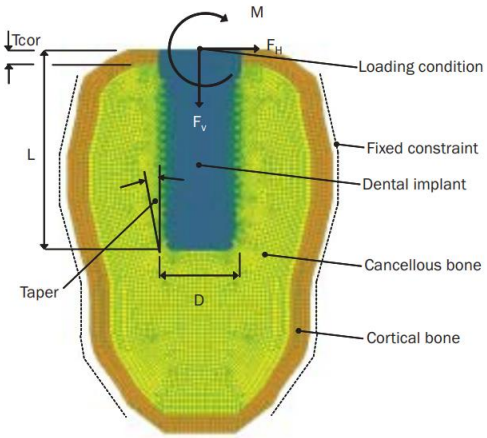

Figure 3.19. Loading conditions of model without restoration – inclusion of bending moment. Adapted from [97].

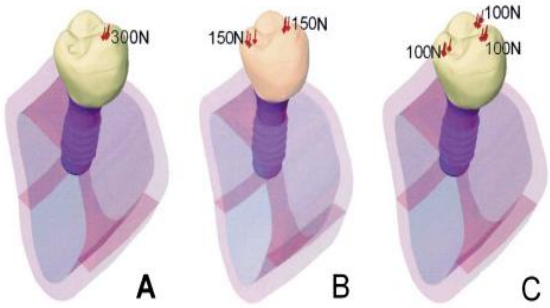

Figure 3.20. Loading conditions of a premolar implant. (a) buccal cusp was loaded; (b) mesial and distal fossae were loaded; (c) combination. Adapted from [98].

If more than one point of application is considered, the global bite force must be split among them. In premolars, the forces are usually applied to the lingual tip of the buccal cusp and on the distal and mesial fossae (Figure 3.20) [98][99], although the application of bite force changes according to the modeling of the restoration [62].

3.2.5 Bone-implant and implant-abutment interfaces

The first formal description of a dental implant included a healing period before the restoration was inserted in the implant body, so that definitive bonding and full osseointegration could occur [81]. Today, most implants have roughened surfaces to increase bone attachment level and bone-implant contact [62].

Many FE studies assume full osseointegration, wherein cortical and trabecular bone and perfectly tied to the implant in all their contact surface [62][67][81]. However, in reality, full osseointegration never occurs [81], due to different levels of bone-implant contact, density and availability of these bone types [62].

The bone-implant interface may be more carefully modeled if friction contact is considered rather than tie contact. Nowadays, FE software provide numerous options for the simulation of contact, and in particular friction contact. Friction is usually fully described by a coefficient (μ), which has to be experimentally determined [67]. Friction contact allows small displacements between the implant and bone, which provokes a change in the contact conditions during the load application, therefore introducing non-linearity in the FE analysis [81].

Moreover, some FE studies where displacements are possible, evaluate the strain energy at the contact surface, and under certain pre-determined thresholds, bone loss is modeled, leading to changes in the density and elastic modulus of bone around the implant [81].

The abutment is usually attached to the implant by a screw or a gluing cement. FE studies assume that this connection is perfect, and a tied contact is often used. As with bone, non-linear

contact is a more realistic approach since micro-motions may happen between the structures composing the implant [81]. Table 3.6 shows different contact conditions in literature involving friction, between bone and the implant, and between the implant and the abutment.

Table 3.6. Friction contact conditions in literature. μ – friction coefficient. *N/A – not available/applicable.

Reference	Bone-implant interface	Implant- abutment interface
[100]	Tie	Friction, μ = 0.3
[101]	Friction, μ = 0.2	Friction, μ = 0.3
[102]	Tie	Friction, N/A*
[103]	Smooth Friction, μ = 0.3 Rough Friction, μ = 0.45 Excessive Rough Friction, μ = 1	N/A*

An alternative to bonded contact is to model a thin surface connecting two structures. For example, Kim *et al.* (2019) simulated the cementum layer between the crown and the abutment in a cementum-retained prosthesis. The 0.1 mm layer had an elastic modulus of around 10 MPa and was tightly bonded to the crown in one side, and to the abutment in the other (Figure 3.21) [104].

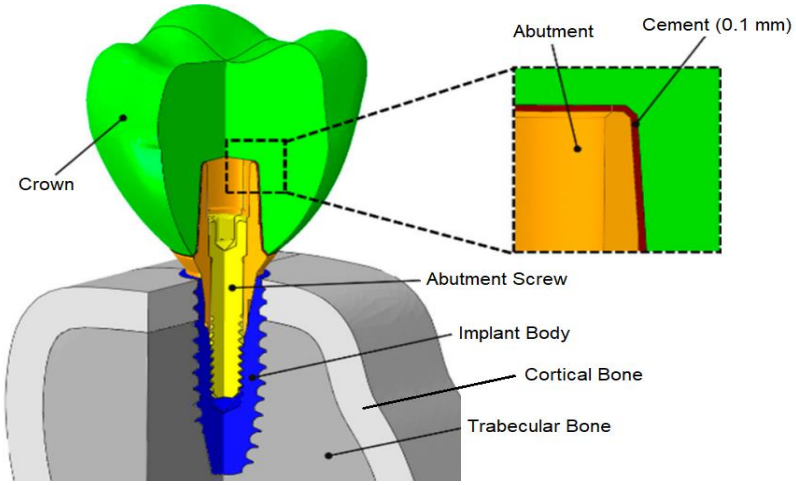

Figure 4.21. 3D model of a molar implant including a cement layer between the crown and the abutment. The cement layer thickness is 0.1 mm. Adapted from [104].

3.3 Simplistic dental implant model by Chun *et al*

Many FE configurations are available to analyze stress distributions in a lower premolar dental implant. This work was inspired in a model that was assumed to properly represent the

geometry and mechanical features of the IAI, which is the target region to analyze in this work. The goal of the study is to evaluate the regions of the inside of an implant considering their ability to welcome a piezoelectric sensor, which is a comparative rather than an absolute analysis. Therefore, on the one hand, the bone-implant interface is not being carefully simulated; on the other hand, the variation of the stress distribution is more relevant than the stress magnitude itself. Moreover, as only a specific condition of the mandible is being investigated, there is no need to visualize and construct a model of entire jaw [62]. Having this in mind, a simpler model might be developed.

Chun *et al.* [105] performed a comparative FE analysis on three different implant systems, among them, the internal hex system, which is widely used in implant dentistry [43]. Its simplified bone and abutment modeling, together with a detailed description of the IAI, made that model a decent starting point for this work's analysis. Moreover, by developing a model based on previous literature, *in silico* validation becomes possible.

Figure 3.22 and Table 3.7 display the geometrical features of this model. Figure 3.22a shows the implant design and its cross section, and Figure 3.22b shows the implant-abutment internal connection in more detail. It is an axisymmetric 3D model that includes the implant body and the abutment. Bone was modeled as a cylinder around the implant, divided into a thinner superior layer and a thicker inferior layer, corresponding to the cortical and trabecular bone, respectively (Figure 3.22c).

The mechanical properties of the constitutive parts of the model are shown in Table 3.8. As observed before for other works in literautre, linear isotropy was assumed in every material. Regarding the boundary conditions and the interface modeling, the outside lateral and bottom surfaces of the bone were set as fixed, and every contact was set as completely bonded except for the IAI, which was assigned a friction coefficient of 0.5, allowing relative motion between the abutment and the implant.

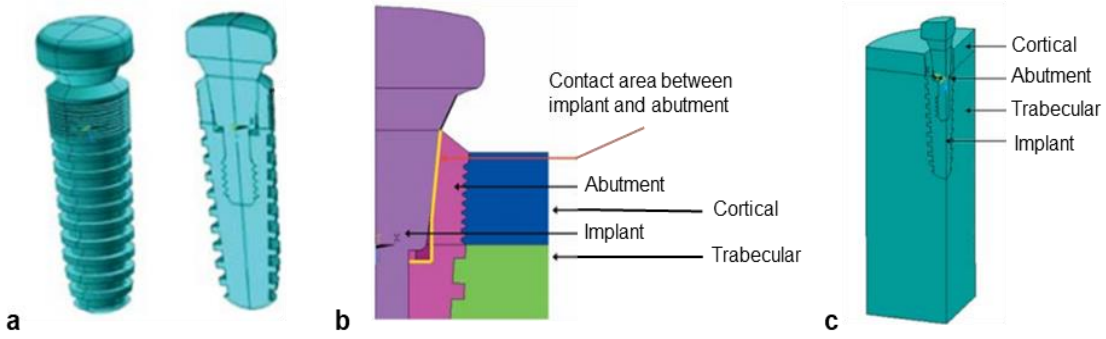

Figure 3.22. Highlights of the implant model by Chun et al. (a) Global view (left) and cross-section (right) of the implant. (b) Detail of the implant-abutment internal hex connection. (c) View cut of the implant and bone. Adapted from [105].

Table 3.7. Geometrical description and dimensions of Chun's dental implant model [105].

Bone	
Diameter	15.3 mm
Cortical bone height	2.0 mm
Trabecular bone height	23.0 mm
Implant length	11.0 mm
Implant	
Diameter	4.3 mm
Taper angle	3.75º
System	Solid two-piece
Abutment connection	Internal hex
Thread	
Thread shape	Square
Thread pitch	0.85 mm
Thread width	0.30 mm
Thread depth	0.30 mm

Table 3.8. Material properties used in Chun's model [105].

Part (material)	*E* (MPa)	*v*
Cortical bone	14 000	0.3
Trabecular bone	1500	0.3
Implant (titanium grade IV)	114 000	0.37
Abutment (titanium alloy)	133 800	0.34

Chapter 4

Pressure Transducers

A transducer is a device that converts a signal from one physical form to a corresponding signal having a different physical form. Therefore, a pressure transducer generates a signal, usually electrical, related to the pressure imposed by the external mechanical system [106]. Pressure is defined as force applied per unit area and in the International System it is quantified in Newton per square meter (N/m^2) or Pascal (Pa). Pressure is measured against a reference, which can be vacuum, atmospheric pressure or a sealed internal reference pressure, therefore leading to three different types of measured pressure: absolute, gage and differential pressure, respectively [107]. A sensor is a transducer specifically used to acquire information by themselves. Different types of pressure sensors have been developed over the years, and they can be classified according to how pressure affects the sensor to produce an electrical signal. There are three types of sensors that, for now, could be used to measure pressure or stress in the implant: capacitive sensors, piezoresistive sensors and piezoelectric sensors.

4.1 Capacitive Sensors

Capacitive sensors for the detection of mechanical quantities all rely on the measurement of displacement [108]. The sensing element typically consists of two conductive plates separated by an insulating dielectric material. One of the plates is fixed and acts as pressure reference while the other moves due to applied pressure, changing the system's capacitance [107]. Therefore, the resulting variable capacitor acts as a detector for pressure changes, and since the value of the capacitor is directly related to its size, and a small capacitor means high noise susceptibility, capacitive sensors should be as large as possible [108].

The capacitance can be calculated by

$$C = e_0 e_r \frac{A}{d} \tag{4.1}$$

where C is the capacitance of the parallel plates, e_0 is 8.854×10^{-12} F/m, e_r is the relative permittivity of the dielectric medium, A is the effective surface area of the parallel plates, and d is the separation distance between the parallel plates of the capacitor. Based on Equation 4.1, the change of any variable parameters (d, A and e_r) due to pressure will change the capacitance value, which is then converted to an electrical output by the detection circuits [109].

This type of sensor has high sensitivity to absolute pressure, low-temperature sensitivity and low power consumption. However, non-linearity at low pressures, complicated signal processing circuitry and dielectric hysteresis are major disadvantages [110].

4.2 Piezoresistive Sensors

These sensors behave as electric resistors whose resistance is affected by some physical quantities [111]. One form of piezoresistive based transducers depends on the piezoresistive effect which occurs when the electrical resistance of a material changes in response to the applied mechanical stress [112]. The electrical resistance (*R*) of a piezoresistor is given by

$$R = \rho \frac{L}{A} \tag{4.2}$$

where ρ is the resistivity of a piezoresistor, *L* is the length of a piezoresistor; *A* is the area of a piezoresistor [111]. Based on Equation 4.2, as stress may affect the geometry, material properties or a combination of these, it induces a change in the resistance, which is then measured and processed to retrieve the original stress value [112]. Strain gauges are based on changes in the factor *L/A*, whereas the parameter ρ is the property of interest in piezoresistive sensors [111].

The underlying principle of piezoresistivity goes back to the energy band structure of the crystal composing the piezoresistive material (*e.g*. silicon). In short, an applied mechanical stress changes the band gap, and depending on the direction of the applied force with respect to the crystal orientation, the average mobility of electrons varies, changing the intrinsic resistivity. Therefore, this type of sensors has anisotropic properties, a crucial consideration if the measurand is expected to vary in direction [111]. In this case, a major difference to capacitive sensors, is that the measured quantity is stress, and not displacement, which can be important when space is a limitation. Most of the times, the resistors are connected in the form of a Wheatstone bridge, which is a circuit system entitled of measuring an unknown resistance, relying on power supply. They can achieve great levels of sensitivity and linearity [112].

4.3 Piezoelectric Sensors

Piezoelectric sensors are the most common dynamic force and acceleration detectors. They produce a voltage when squeezed by a compressive, tensile or torque force, which is proportional to the force applied. After the force is applied, the electrical signal generated by the crystal decays rapidly, which makes these sensors well-suited for measuring dynamic changing forces and pressures [113].

When external physical stimuli such as pressure or force is applied to a piezoelectric material, it is elastically deformed, and its internal charge distribution is rearranged (Figure 4.1) so a net charge is developed [107] (Figure 4.2). This charged piezoelectric crystal is equivalent to a charged capacitor. The balance of the applied force is converted into mechanical energy, as in the case of a compressed spring. When the force is removed from the crystal, it will spring back to its original shape and the electric charge will disappear [107]. Moreover, the associated deformation is in most cases negligibly small, allowing the piezoelectric sensor to be mounted in a robust, static and hermetically sealed package [111]. Quartz and ferroelectric ceramics are

commonly used materials, quartz-based sensors being the less expensive [107]. As in the piezoresistive case, many piezoelectric materials are anisotropic [111].

Although force is the primary quantity that is measured by a piezoelectric sensor, other quantities such as pressure, strain, and acceleration can easily be measured as well, using a proper construction. In a piezoelectric pressure sensor, the pressure to be measured is applied to a thin metal membrane. The total force on the membrane, that is the pressure times the active area of the membrane, is mechanically transferred to the crystal [111].

Some piezoelectric systems use preloading to ensure that the crystals are held in close contact, which increases the linearity and accuracy of the sensor [113]. This means that the physical and geometrical integration of the piezoelectric material in the implant can be tight and the sensor can have direct contact with the implant/abutment even when no force is being applied. Piezoelectric sensors have attractive characteristics including small size, high speed, and self-generated signal [107]. Moreover, they can detect pressures between 0.7 kPa and 70 MPa [107].

As piezoelectric sensors do not need power consumption to retrieve the output signal and have a nearly static geometric response to mechanical stress, they are the preferred sensors to be included in the sensing unit to be placed in the implant.

Over the past decades, several advances have been made in micromachined sensors and actuators. The need for integration of materials into microelectromechanical systems (MEMS) is emerging, and piezoelectric materials are high energy density materials that can be miniaturized without quality loss, thus leading to a growing interest in piezoelectric films for MEMS applications [114]. Piezoelectric sensors with dimensions ranging from a few hundreds of nanometers to tens of micrometers have been reported to deliver great performances [115][116][117], thus they can be integrated within the implant easily.

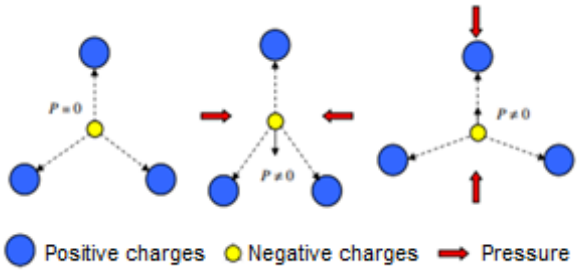

Figure 4.1. Piezoelectricity. Deformation results in a change of electric polarization (*P*): when under compressive or tensile pressure, positive and negative particles are displaced relative to each other, causing a net polarization. Adapted from [111].

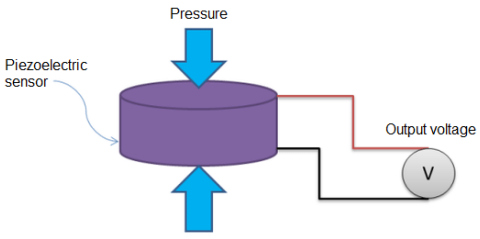

Figure 4.2. Block diagram of a piezoelectric sensor. Adapted from [114].

Chapter 5

Methods

The model of the present study was developed using computer aided design (CAD) and FE software. The CAD program was SolidWorks® (Dassault Systèmes SolidWorks Corp., USA), where the 3D models of the implant system and bone were produced; the FE program was ABAQUS® (Dassault Systèmes Simulia Corp., USA), where the biomechanical stress analysis was carried out. This chapter will explain how the 3D model was generated and in which conditions the analysis was performed, in the light of the previous chapter about FE of dental implants, namely the model by Chun *et al.* [105].

5.1 Implant-bone geometry modelling

SolidWorks was used to design a faithful recreation of the geometry employed by Chun *et al* [105]. Both dimensions in Table 3.2 and screenshots of Figure 3.22 were used to aid the 3D modeling of the implant-bone system, together with commonly used CAD tools such as extrude, revolve, fillet, cavity, dome, spline, among others. Moreover, smart dimensioning and mating operations ensured the integrity of the model and its symmetry along the designing process. Only the bottom screw of the abutment was not included in the model, and it was replaced by a regular cylinder instead.

The crown restoration was not considered in Chun's work, however its importance on the simulation has been discussed. Therefore, a whole new crown was sketched from the bottom after anatomic images and specifications for the lower premolar. The complexity of the tooth's geometry, which involves irregular cusps and ridges, makes it difficult to recreate a faithful copy using CAD software alone. However, a simple version of the crown was produced, considering the buccal cusp and the mesial and distal fossae, and then splinted to the abutment.

Figure 5.1a shows each single part of the final assembly of this study's model, Figure 5.1b overlooks the internal connection design, Figure 5.1c shows the bone sub-assembly and Figure 5.1d shows the implant system. The cortical and trabecular bone, the implant and the abutment are symmetric about the buccolingual and mesiodistal axes, whereas the crown is symmetric only about the mesiodistal axis.

The assembly containing all five parts and the one containing every part except the crown were saved into two different geometric models, corresponding to the model with and without the crown, respectively. Then, each model was converted into an STL file to be imported into ABAQUS, where the stress analysis was carried out.

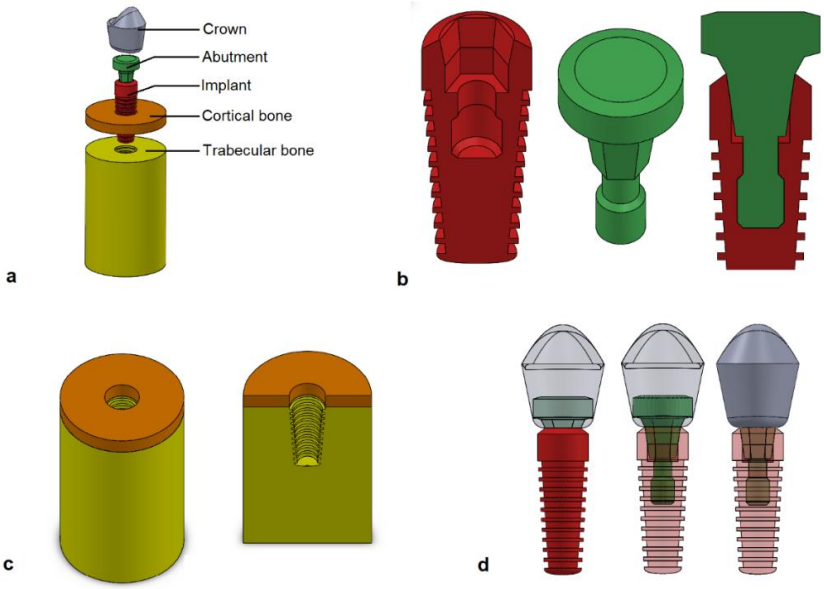

Figure 5.1. 3D model of the present study. (a) Global view with separated parts. (b) The implant-abutment internal hex connection. (c) Bone sub-assembly (d) Implant sub-assembly.

5.2 FE modelling

ABAQUS is a FE software that allows the mechanical simulation of complex systems involving a variety of material properties, different loading conditions and a great set of contact and boundary conditions. Its interface is divided in modules, each on responsible for the setting of parameters related to a specific aspect of the simulation. A comprehensive visit through each module is carried out further ahead, in parallel with the overview of the development of the FE model of the implant. For the sake of simplicity, the model that is going to be considered is the one including the crown, except when it is said explicitly otherwise.

5.2.1 Part Module

In this module, surface and line partitions were created for each part, and the resulting surfaces and points were comprehensively labelled. This step was crucial to keep the whole modelling process clean and comprehensible. The labelled surfaces include those who participate in contacts, boundary conditions, occlusion, etc. On the other hand, the labelled points include points of application of forces, points used in the convergence analysis, points of interest for the output analysis, etc. The partition operation had in mind the preservation of symmetry, that is, every time a partition was created in one face, a symmetric partition was created in the opposite face. This ensures that the model remains as symmetric as possible after meshing.

5.2.2 Property Module

Bone and implant materials were the same used by Chun *et al* (Table 3.3). The crown material was modeled after Liang *et al* [89], where linear isotropy was also considered, with an elastic modulus of 68.9 GPa and a Poisson ratio of 0.3. The anisotropy of bone was not considered assuming that it does not affect the stress distribution, given the regularity and symmetry of the geometries involved in the simulation, and therefore increasing the simulation's efficiency. In this study, every part was considered solid and homogeneous.

5.2.3 Step Module

In this study, a general static step was created, with time period equal to 1 and considering non-linearities from great deformations and displacements, that may arise from the sliding allowed by the friction contact in the IAI. The arbitrary choice of 1 second comes from the fact that there are not time-dependent material properties; hence, the step period is just a time scale factor.

5.2.4 Interaction Module

This model has several surfaces interacting with each other during the mechanical analysis. The implant body is attached to bone through the thread, the crown is cemented onto the abutment, which in turn is screwed into the implant body, and cortical bone is fixed to trabecular bone by a biological structural continuity. Friction contact was assigned to the IAI to simulate the inevitable screw loosening due to the everyday loading; the friction coefficient was set to 0.5 to match that used by Chun *et al*; also, separation after the initial contact was allowed. The remaining interfaces were considered fixed; hence tie constraints were assigned to the implant-bone and cortical-trabecular bone interfaces. Moreover, the bottom cylinder of the abutment was also tied to the implant, to function as a screw, which exist in the original model, but was not introduced because of the modeling complications involved with the micro-dimension of its thread.

5.2.5 Load Module

The last step before meshing is to define the boundary and loading conditions. Displacement and rotation were set to zero at nodes belonging to the lateral outer surface of both cortical and trabecular bone and to the bottom surface of trabecular bone.

Loading was done in four distinct configurations named LC1, LC2, LC3 and LC4, which are graphically displayed on Figure 5.2. F_{MD} is the mesiodistal component, F_{Ax} is the axial component, and F_{BL} is the buccolingual component of the resultant force at each point of application. LC1 and LC2 are used in the model without crown, whereas LC3 and LC4 are used in the model with crown. LC1 consists of applying the force at the center of the abutment. In LC2, an additional

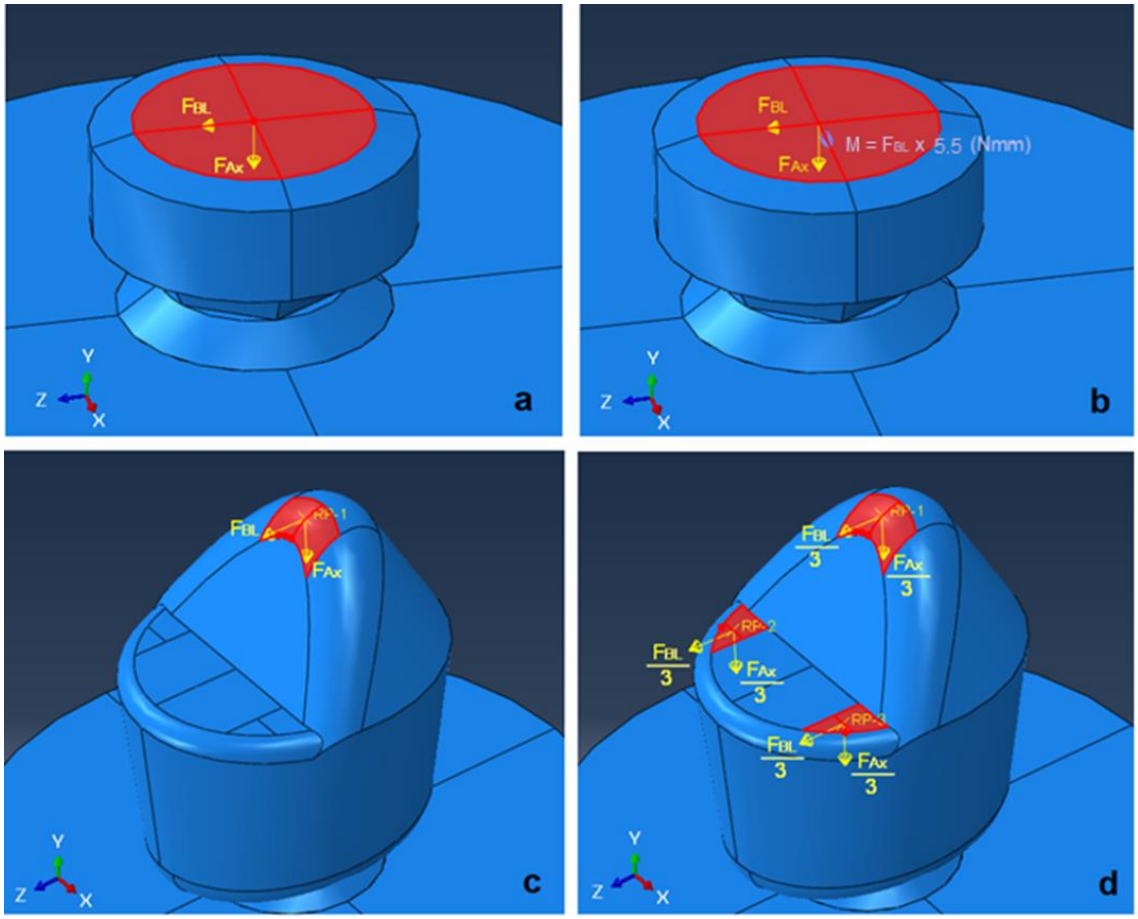

Figure 5.2. Loading conditions used in this study. Four different modes were considered: (a) LC_1 – used in the model without crown; no inclusion of moment; (b) LC_2 – used in the model without crown; inclusion of moment; (c) LC_3 – used in the model with crown; loading on buccal cusp only; (d) LC_4 – used in the model with crown; loading on buccal cusp, and both mesial and distal fossae.

moment equal to F_{BL} (N) times 5.5 mm is applied around the mesiodistal axis and its orientation agrees with that of the F_{BL} component. 5.5 mm is the distance from the center of the top surface of the abutment to the top of the buccal cusp. On the other hand, LC3 considers loading just at the buccal cusp, whereas LC4 considers also the mesial and distal fossae. Moreover, because the force was distributed among three surfaces instead of one in LC4, the force at each surface is divided by three, so that the resultant force remains the same as in LC3.

F_{MD} was set to zero in the light of the study by Eskitascioglu *et al*. also on a premolar [98]. Moreover, forces could be either static, where $\mathbf{F_S} = (0, F_{Ax}, F_{BL})$; or time-dependent (dynamic), where $\mathbf{F_D}(t) = (0, F_{Ax}(t), F_{BL}(t))$. A more thorough understanding of the spatial meaning of these components is portrayed on Figure 5.3. Moreover, forces can be described by their magnitude and buccolingual angle. For instance, a static 1 N force with a ±45º angle is the same as having $\mathbf{F_S} = (0, -\frac{\sqrt{2}}{2}, \pm\frac{\sqrt{2}}{2})$ (N).

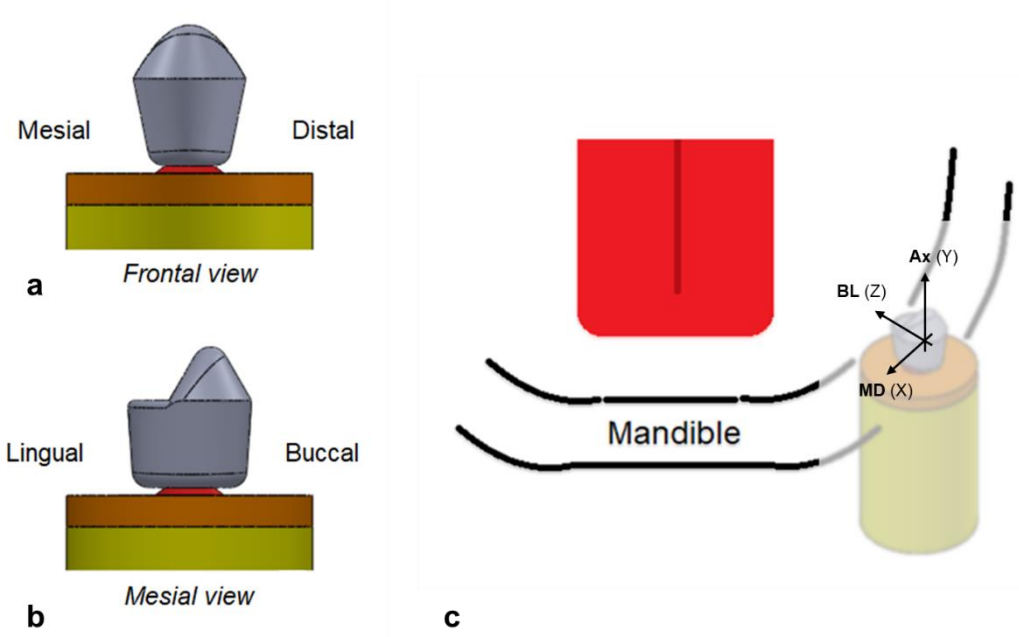

Figure 5.3. Orientation of the developed implant model. (a) Frontal and (b) mesial views of the crown. (c) Spatial context of the left lower premolar implant-bone model of the present study; the red structure is the tongue, and the black lines show the mandibular arch; global axis is included with the same orientation as in ABAQUS.

5.2.5.1 Dynamic force simulation

Dynamic loading was considered only for LC4 in the final part of this work to assess the selection of the points of interest to welcome the sensor. Two dynamic loads were modeled, dynamic load 1 (DYN_1) and 2 (DYN_2). Both loads angles varied from -90º to +90º. DYN_1 had a static magnitude of 200 N, whereas DYN_2 magnitude varied with the angle. The time plot of the load is displayed on Annex I. In order to simulate the preload applied to the implant at the time of insertion [118], an extra step was added before the occlusion, and an axial 200 N load was applied. The rationale for considering preloading resides in the non-linearity of the model introduced by the friction contact at the IAI.

5.2.6 Mesh Module

The models of the present study were meshed with tetrahedron quadratic elements, giving a total of 161016 elements and 174981 elements for the model with and without crown, respectively. These were achieved after a convergence study where maximum Von Mises stress and Von Mises stress at two points of interest were analyzed for models with meshes of different size. The results are presented in the sub-chapter 6.1. The approximate global size of the elements was 0.4 mm, and 0.3 mm at the implant-bone thread interface as proposed by Geng *et al*. [67], and curvature and minimum size controls were used in order to increase mesh quality: minimum deviation factor, which is the ratio between the height and width of the element triangular

faces, was set to 0.2, to promote the generation of unedgy, bulky tetrahedrons; and the fraction of global size was set to 0.5, thus forcing the elements to be generated with approximately similar size.

The trabecular bone is by far the most voluminous part, and a great fraction of it is not involved in the interactions with the implant system. In order to avoid the creation of an over-meshed trabecular bone, interior element growth was increased in 20% compared to ABAQUS default. This decreased the number of elements by a half in the trabecular bone part, without compromising the accuracy of the results.

The geometric model is highly symmetric, and it is important that the meshing process does not interfere with the symmetry, which could result in inaccurate stress distributions. One way to avoid the inherent asymmetry introduced by the meshing process is to reduce the size of the elements until it is negligible compared to the order of magnitude of the model, however this is very computational costly. A good alternative is to partition the geometry, ensuring that the vertices of the elements are uniformly distributed over the boundaries of the surfaces composing the model, and selectively refining surfaces of interest, allowing a finer mesh at edgier regions of the model, which grants a smoother and continuous stress transmission (Figure 5.4). The surfaces where it was more important to ensure symmetry were those comprising the implant-abutment interface, given the goal of this study. However, all parts of the model underwent this process, and the outcome was a neat, nearly symmetric mesh.

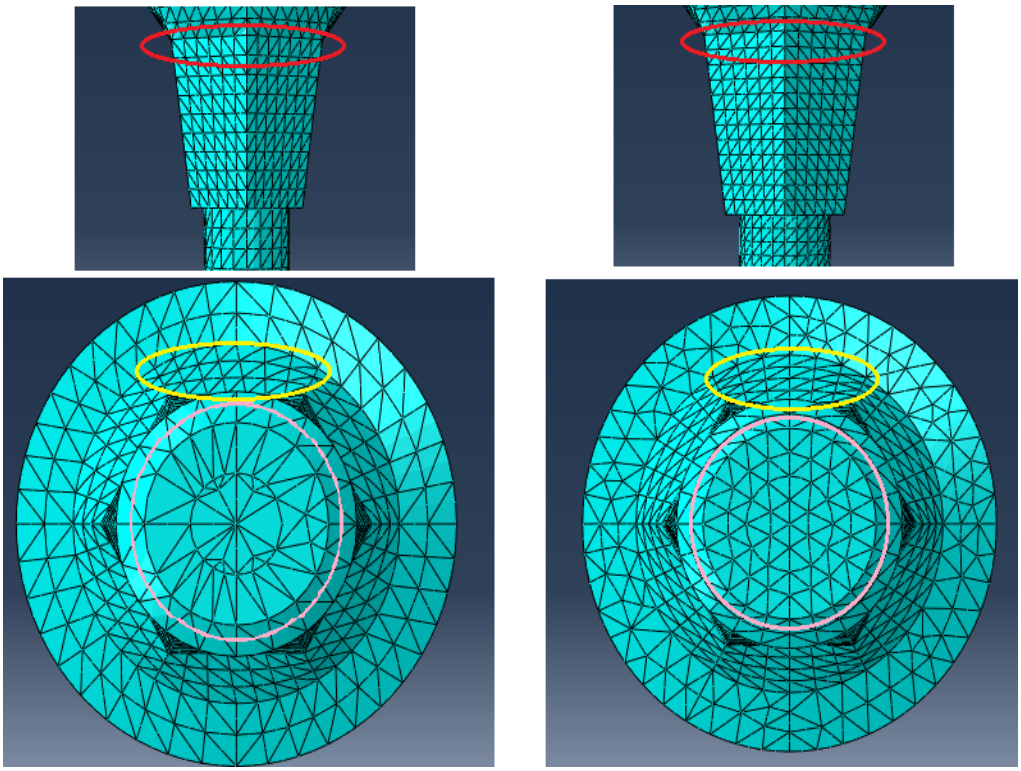

Figure 5.4. Importance of partitioning and selective refinement in meshing. (*left*) Before and (*right*) after partitioning. The colored circles show the regions where this was more visible. (*top*, red) the number of columns is not equal face to face; (*center*, yellow) non-uniform element size; (*bottom*, pink) the bottom surface of the implant-abutment interface.

5.3 Target regions and points of interest

The interface between the abutment and the implant has many surfaces that could be able to welcome the piezoelectric sensor at first sight, as the sensor alone is assumed to have micro dimensions. Nonetheless, the associated circuitry for the signal processing increases the volume availability requirements. Also, faces with small area that are relatively near sharp corners may be involved with poor stress distribution. Moreover, as the bite forces are most frequently axial forces, the sensor should be preferably place at faces that are perpendicular or oblique to the axial axis of the implant, so that the sensor can effectively read the compressive component of the force at its location. Figure 5.5 shows an implant cross section and highlights the IAI, with different colors for faces that are suited and not suited to welcome the sensor accordingly to the just mentioned criteria.

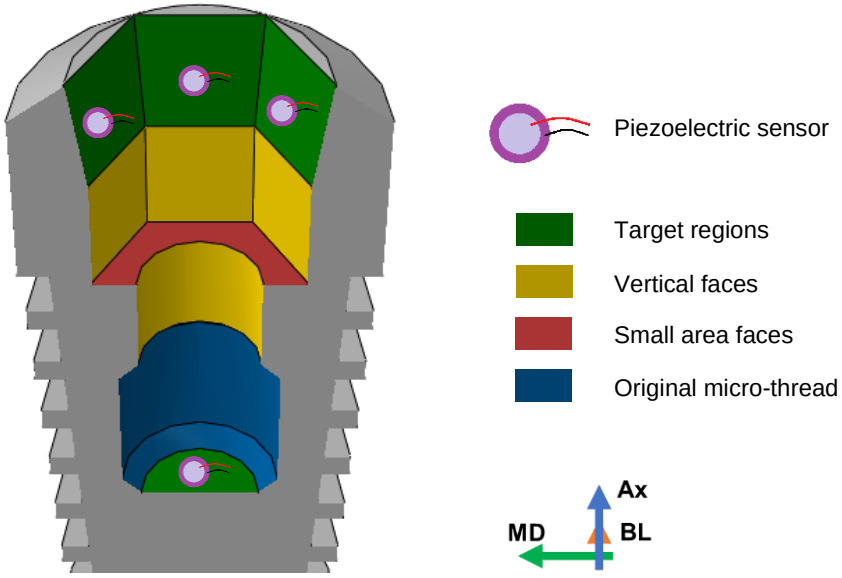

Figure 5.5. Criteria for the selection of the target regions. Piezoelectric sensors are included for clarity. Green-colored faces are the target regions considered on this study; yellow-colored faces are parallel to the axial axis of the implant; the red-colored face has small area; blue-colored face correspond to the original screw thread of Chun's model.

Seven faces from the implant-abutment interface were selected as target regions to welcome the piezoelectric sensor. The center of each one of the top six faces was considered a point of interest, and six points hexagonally distributed on the bottom face were also considered points of interest, giving a total of six top points of interest and six bottom points of interest. Figure 5.6 shows the distribution of these points along the implant and their labels, which were smartly assigned so that points with the same number correspond to axially related points, and points with smaller numbers are more lingual, except for the pairs {2,3} and {4,5} which have the same buccolingual coordinate.

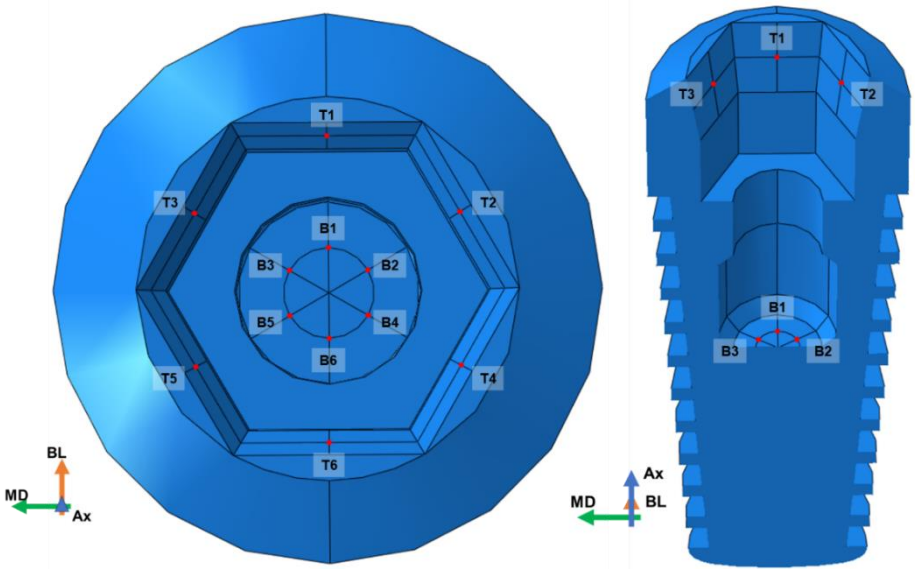

Figure 5.6. Target regions and points of interest of the study. (left) occlusal view of the implant; (right) buccal view cut of the implant. T- labeled points are those at the top faces of the implant-abutment interface, whereas the B- labeled points are at the bottom face of the interface. A great number means that the point is more buccal, whereas a small number means more lingual instead.

5.4 Scalar stress outputs used in the analysis

Stress is described by a multidimensional tensor at each point, thus several scalar outputs can be derived from its components and different meanings and interpretations can be assigned to each output depending on its definition. This work uses three scalar stress outputs, namely Von Mises stress, average absolute compressive (AVGAC) stress and maximum absolute principal (MAXAP) stress.

Von Mises is widely used in FE studies, combining all nine components of the Cauchy stress tensor; therefore, it was the first choice for stress analysis in the present work.

Secondly, AVGAC stress includes the normal components of the tensor, and it is defined as

$$AVGAC = \frac{|\sigma_{11}| + |\sigma_{22}| + |\sigma_{33}|}{3} \tag{5.1}$$

where σ_{11}, σ_{22} and σ_{33} are the normal stresses for each one of the three dimensions. As piezoelectric sensors commonly read normal rather than shear stress, this scalar output intends to give more meaningful insight on the stress state at a given point, contrarily to the more general Von Mises stress. The modulus is included in order to avoid the axis-dependence of the stress sign; thus, compressive stress at two oppositely oriented faces have the same sign (positive). Moreover, the stress tensor components are determined with respect to a default global coordinate system. For instance, in the present work, σ_{11}, σ_{22} and σ_{33} are the normal stress with respect to the mesiodistal, buccolingual and axial axes, in that order. This coordinate system is

thus useful to study the stress state at faces that are oriented along one of the coordinate planes, which happens for the bottom target region on Figure 5.5. However, the six faces composing the top target region are slightly inclined and make a 7º angle with the axial axis, meaning that the normal stresses are rotated 7º from the global coordinate system, and the normal stresses of the tensor do not correspond to the normal stresses at those faces. This could be solved by using rotation matrixes so that local stress tensors would be derived for each face according to its orientation. This process is rather complicated and involves extra computational cost. In addition, the 7º angle can be assumed as small enough that using the global coordinate system will not deliver misleading results. Furthermore, the inclusion of all three normal components in the AVGAC stress equation (Equation 5.1) also reduces the error that could arise from this simplification.

Lastly, MAXAP stress is simply the principal stress with the greatest absolute value at a given point, which informs on the maximum normal stress that can be measured if the sensor is oriented at a specific direction. The reasoning for considering MAXAP stress lies on the fact that the sensor can be re-oriented in each face, as illustrated in Figure 5.7b, thus being under the maximum stress possible at that point. If the direction of the principal stress is significantly different from the normal of the sensor, one alternative is to select piezoelectric sensors that detect shear stress instead (Figure 5.7c). However, this kind of sensors is not as common in MEMS as normal stress sensors, therefore the later should be preferred.

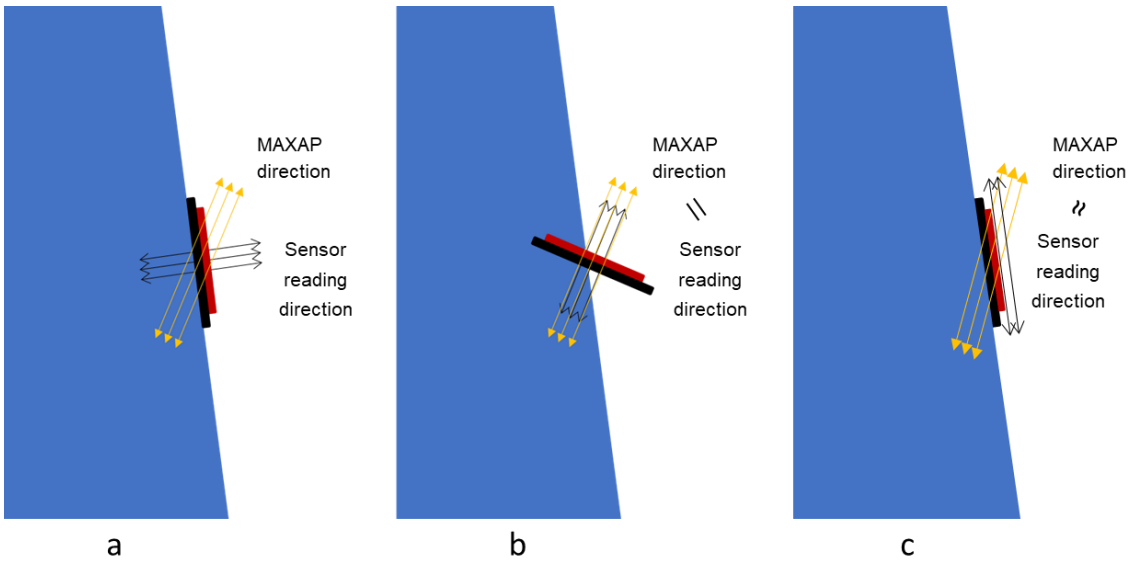

Figure 5.7. Schematic relation of the piezoelectric sensor orientation and the maximum principal stress. The sensor is represented as two rectangles. a) The sensor reading direction does not match the maximum stress direction; (b) the sensor was re-oriented in order to match the maximum stress direction; (c) shear stress sensor captures the MAXAP stress more effectively than in case (a).

Chapter 6

Validation of the FE Model

The model without crown and loading conditions of the type LC_1 were used to validate the study. These are described in the previous chapter. The model with crown and the remaining loading conditions were automatically assumed to be validated after this. The first step of the validation is to perform a convergence analysis to find the best mesh size for the model, followed by a comparison between the resulting model and the one from Chun *et al* [105], on which this was inspired.

6.1 Convergence Analysis

Mesh convergence is an important issue in FE analysis, which is related to how small the elements need to be so that the results of the analysis are not affected by changing the size of the mesh. In this study, the quantity used in the convergence analysis was the equivalent Von Mises stress. Five mesh sizes were analyzed: with 28,958; 66,170; 84,776; 158216 and 181,343 elements. Figure 1 and 2 show the evolution of the maximum stress in each part of the model, and in two points of interest of the implant and the trabecular bone, respectively.

Several metrics can be employed to measure convergence and then decide a correct mesh size to use. In this study, the relative variation of the stress when the mesh size increased was used. The equation for the relative variation ε is

$$\varepsilon = \frac{\sigma_{i+1} - \sigma_i}{\sigma_i} \tag{1}$$

where σ_i is the stress at the i^{th} mesh size. The used metric was ε<10% for all curves. Looking at Figures 6.1 and 6.2, it is possible to see that this happens overall when the size is equal to 158,216 elements. In order to improve the stress distribution at some regions with more pointy edges and sharp angles between surfaces, a selective additional refinement was done, which resulted in similar stress distribution and magnitude, and in a final mesh size of 161,061 elements. The model with crown had 174,981 elements.

6.2 Comparison with literature

In addition, a comparative study of the maximum equivalent Von Mises stress in cortical and trabecular bone between this model and the one from Chun *et al.* [105] was done, in order to validate the geometry recreation and the FE parameters described in the previous chapter.

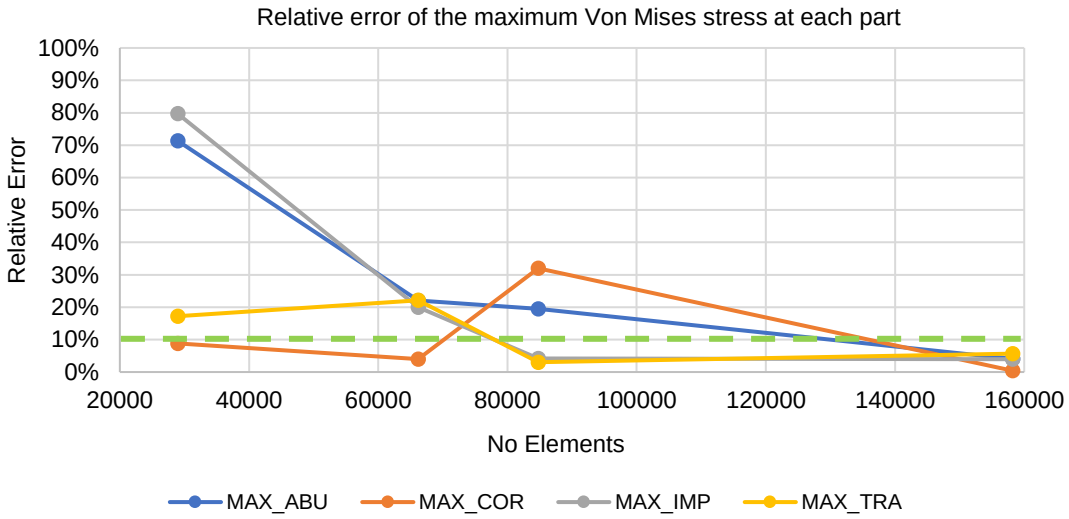

Figure 6.1. Convergence analysis of the FE model – relative error of the maximum equivalent Von Mises of each part of the model. Dashed line marks 10%. Every curve is under 10% at 158216 elements.

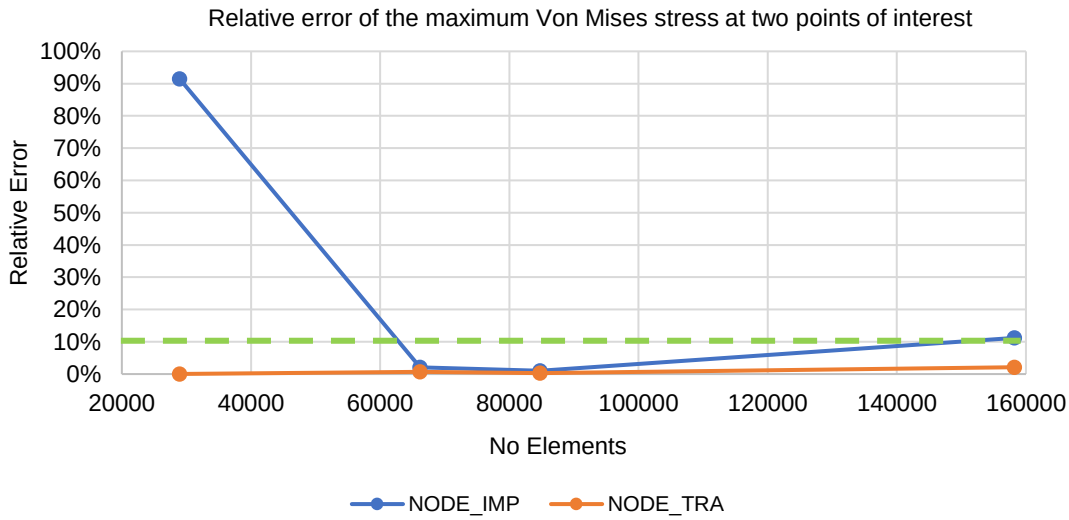

Figure 6.2. Convergence analysis of the FE model – relative error of the equivalent Von Mises at two points of interest. NODE_IMP is the center point of the bottom surface of the implant-abutment interface; NODE_TRA is the center point of the bottom surface of the implant-bone interface. Dashed line marks 10%. Both curves are under 10% at 66170 elements.

The model was loaded with a static force of 100 N, with loading angles of 0º, 15º, 30º and 60º (Figure 6.3). For both models the maximum Von Mises stress increased with the loading angle, in both cortical and trabecular bone. However, the model from the present study has slightly higher stresses and the increase with the loading angle is also a little bit steeper. Nevertheless, the order of magnitude is the same. Moreover, the stress distribution was very similar between the two models. These similarities are shown on Figure 6.4: the interface between the cortical bone and the implant is the bone region with highest stress; trabecular bone between the threads is shielded by them; and the middle part of the abutment just before the screw accumulates more stress.

Because this study addresses a qualitative approach rather than an absolute approach, it is safe to assume that this model is adequate for further analyses. The differences in the stress outcome between the models appear to lie especially on the stress magnitude, whereas great similarity between the stress distribution can be observed. Even if this study's model cannot predict accurately the absolute value of the stress components at the points of interest, it does offer reliable insight on the stress variation along the model, and under different loading conditions, which is sufficient to achieve the goals of the study.

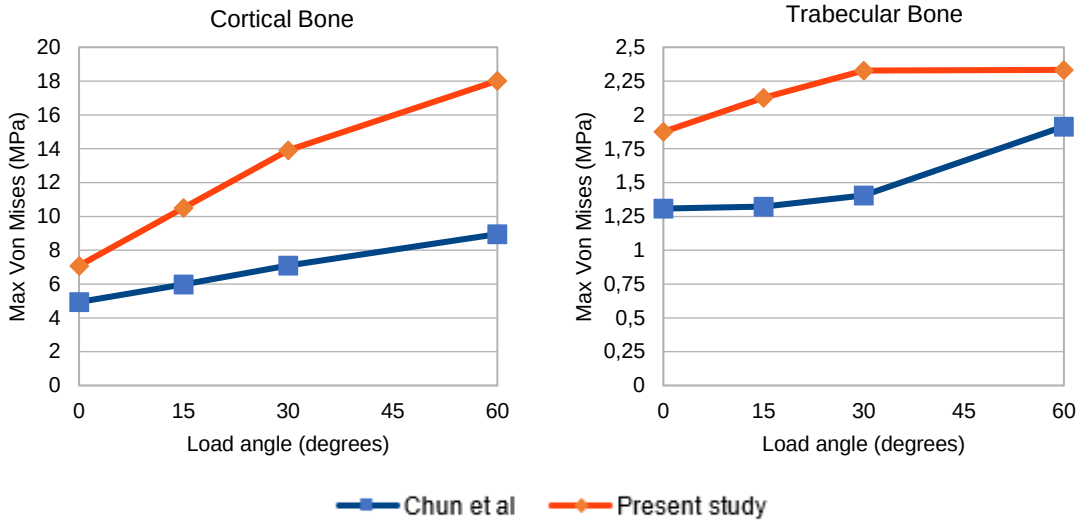

Figure 6.3. Maximum Von Mises stress in bone in the model of the present study and in the one from Chun et al. [105]. Von Mises stress was evaluated under different loading angles. In both cortical and trabecular bone, maximum Von Mises stress increases in both models. The curve respective to this study's model has a positive offset compared to that of Chun et al. Both curves have the same order of magnitude.

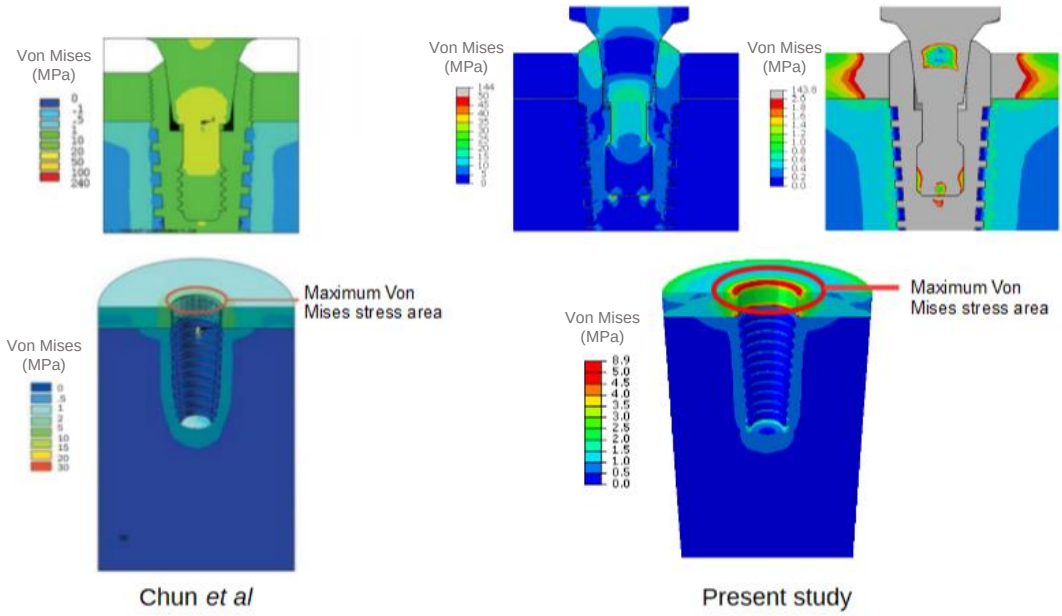

Figure 6.4. Von Mises stress distribution in the model from Chun *et al.* [105] (*left*) and in the present study's model (*right*). Both models were loaded with an axial force of 100 N. Upper row: detail of the implant-abutment interface; lower row: stress distribution in bone.

Chapter 7

Results and discussion

The main goal of this study is to analyze which regions within the IAI are best suited to welcome a piezoelectric sensor, in order to detect changes in the direction and magnitude of mastication forces. However, the analysis of the effect of the implant geometrical features on the stress outcome is done in the first place to better comprehend the stress distribution along these target regions.

The loading conditions models LC1, LC2 and LC3 with the same resultant force were compared in order to assess analyze the effect of the crown in the model, and the validity of replacing it by a bending moment. Moreover, a brief comparison between models LC3 and LC4 is done, allowing some insight on the effect of loading different areas of the crown on the stress distribution at the IAI. In addition, there are two ways to position the hexagonal abutment: two of the six edges of the hexagon can be either perpendicular or parallel to the buccolingual axis. The difference between orientations was also assessed.

After the first part of the results, loads with different directions and magnitudes were applied to the model LC4 in order to select the best implant regions to read detect changes in these properties of the mastication forces. Finally, a dynamic force modelling the inherent variation of load angle and magnitude within mastication was applied, and the three stress-based scalar outputs described in chapter 5 were measured at the chosen target regions, in order to assess the scoring method and to confirm these points can competently detect the mastication forces.

7.1 Validity of using a moment to replace the crown component

The models in LC1, LC2 and LC3 were loaded with a 100 N static force with angles equal to 0º, ±45º and ±90º. Figure 7.1 illustrates the LC3 case and offers a more comprehensive look on the angles and their spatial meaning. Figure 7.2 displays the LC2 model for the +90º force,

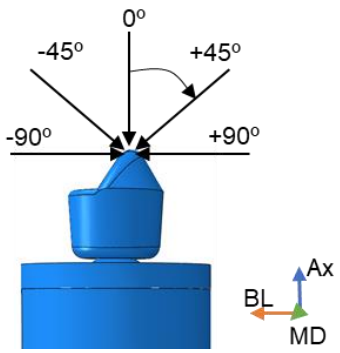

Figure 7.1. LC3 configuration for the moment inclusion test. Force vectors are displayed, along with the global axis on the right.

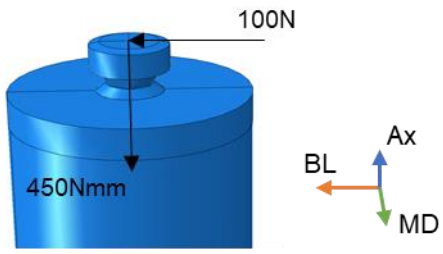

Figure 7.2. LC2 configuration with 100 N force at +90º. The moment is parallel to the MD axis. Global axis is displayed on the right.

including the bending moment around the mesiodistal axis. Table 1 shows the Von Mises stress at the 12 points of interest for each loading condition model and for each angle.

Table 7.1. Von Mises stress (MPa) at the twelve points of interest when the model is under a 100 N load with different angles and loading conditions. LC2 is, by definition, equal to LC1 for axial forces, hence it was not considered. The top points are separated from the bottom points for the sake of clarity.

	-90º			-45º			0º		45º			90º		
	LC1	LC2	LC3	LC1	LC2	LC3	LC1	LC3	LC1	LC2	LC3	LC1	LC2	LC3
B1	6.7	14.9	15.4	1.9	7.2	8.4	5.2	4.0	7.6	12.6	12.3	5.4	11.1	11.6
B2	4.1	8.9	9.2	1.9	3.5	4.2	5.4	4.5	5.4	7.2	7.1	3.0	5.7	6.0
B3	4.4	9.1	9.4	1.5	3.6	4.2	4.9	4.2	**5.1**	**6.7**	**6.6**	2.6	5.2	5.4
B4	2.6	5.2	5.4	5.1	6.7	7.0	4.8	5.0	1.7	3.5	3.4	4.3	9.0	9.3
B5	2.6	5.4	5.6	**5.0**	**6.9**	**7.3**	5.0	5.3	1.4	3.9	3.7	4.7	9.7	10.0
B6	5.6	11.1	11.6	7.5	11.6	12.6	5.5	6.1	2.8	7.5	7.2	6.9	14.8	15.3
T1	**35.1**	**73.5**	**72.7**	21.2	49.5	47.9	12.8	30.4	20.5	64.1	64.2	44.0	99.4	100.4
T2	44.2	95.2	108.1	29.2	65.6	83.9	12.9	33.8	51.5	129.2	115.3	97.5	197.7	194.2
T3	43.7	93.7	106.1	28.9	64.8	82.1	13.1	35.6	53.6	132.5	111.9	99.2	201.6	191.6
T4	101.4	204.2	191.3	54.2	135.2	130.1	12.9	36.6	28.9	65.3	73.6	43.8	94.7	105.8
T5	99.6	201.7	198.2	53.5	133.3	137.8	12.9	32.3	29.2	65.3	73.4	43.7	94.4	106.1
T6	45.4	103.0	93.8	20.5	66.7	68.1	12.9	33.9	21.3	50.4	42.2	**35.2**	**74.1**	**74.9**

There are different interesting phenomena regarding the evolution of stress from point to point at a given loading condition and angle, discussed hereafter. Firstly, the top points of interest have greater stress than those at the bottom, due to their closeness to the applied loads. On the other hand, the symmetry about the buccolingual axis of the models is clear, as nodes located at the same buccolingual coordinate (points {B/T2, B/T3} and {B/T4, B/T4}) have similar stress in general. In addition, symmetry about the mesiodistal axis is also observable, although less obvious. Buccal points have nearly the same stress under negative angles as lingual points under the opposite positive angles. For example, point T1 under a -90º load has similar stress to point T6, standing in the opposite side, under a +90º load. On the other hand, point B3 under a +45º load has similar stress to point B5 under a -45º load. These two cases are highlighted in Table 7.1. This stress symmetry happens for the model without crown due to the geometric symmetry of the model. However, this is not entirely true for the model with the crown (which is symmetric only about the buccolingual axis). In this case, the apparent symmetry about the mesiodistal axis comes from the fact that the loads are transferred from the crown to the abutment, whose neck is small compared to the crown, and only then to the implant; hence, crown's asymmetry becomes negligible at this level.

The main goal of the comparison among LC1, LC2 and LC3 was to analyze the effect of including the bending moment in the model without crown. This can be done either graphically or numerically, as showed further.

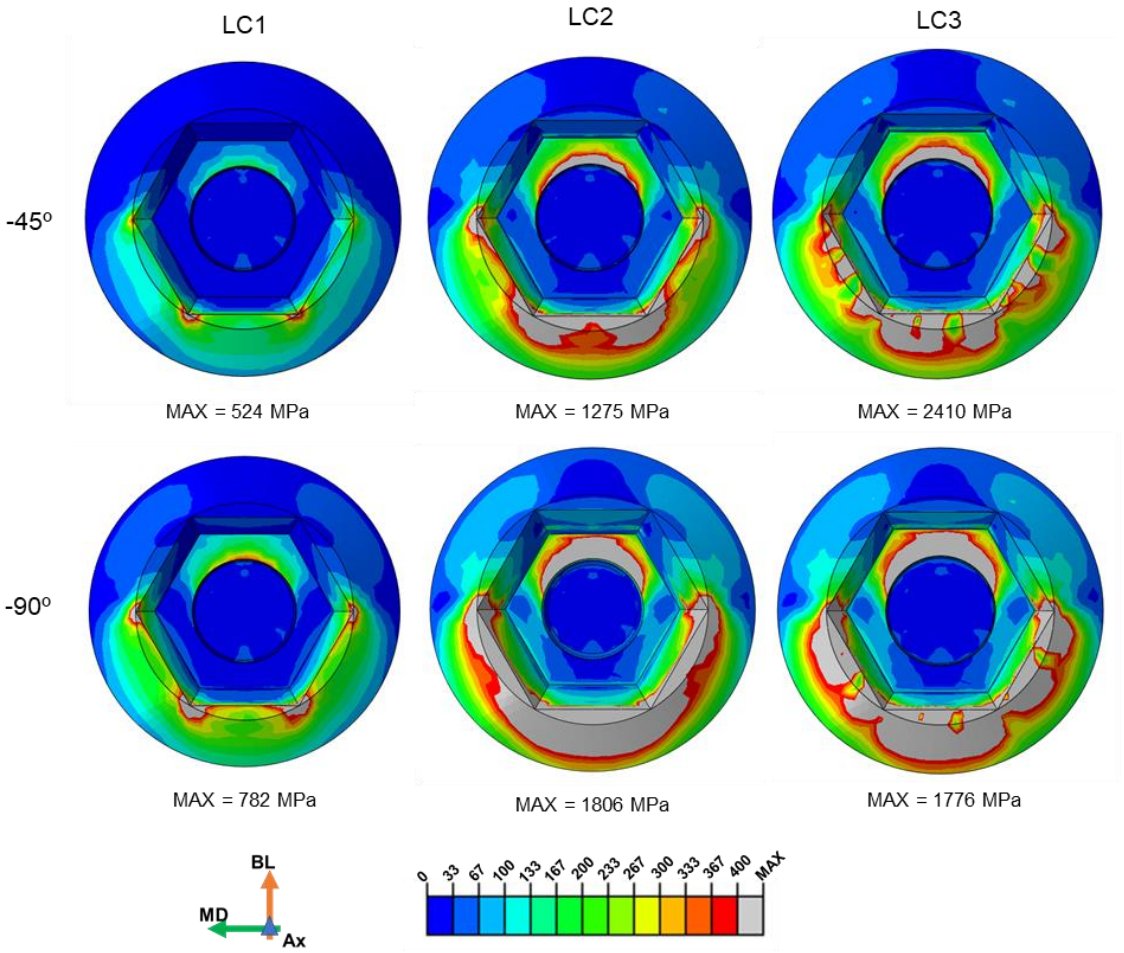

Figure 7.3. Comparison of the Von Mises stress at the implant for loading conditions LC1, LC2 and LC3, at 100 N forces with angles -45º and -90º. The global axis and scale at the bottom are equal for the six images. The maximum stress that delimits the grey area is below each image.

Figure 7.3 is a graphical approach showing the Von Mises stress distribution at the implant for the three loading scenarios and under forces with angles equal to -45º and -90º. The stress distribution is similar among the different loading conditions, with higher stress at the buccal side of the neck of the implant, to which the load is pointing towards, and at the lingual side of the bottom hexagon, resulting from the moment and the lever mechanism created between the middle abutment and implant. However, although the stress distribution is alike, there is a major difference in absolute terms between LC1 and LC2/LC3. This is clear in Figure 7.3 and in Table 7.1, as for both -45º and -90º forces, the grey area corresponding to the highest stress is significantly greater for LC2/LC3 when compared to that in LC1, for the same load angle (the color scale is the same for every image). This difference is due to LC1 not considering the bending moment caused by the buccolingual component of the force, which is included in LC2 and LC3. However this graphical approach gives comprehensive insight about the difference between LC1 and LC2/LC3, it is not completely clear what changes from LC2 to LC3. Thus, a numerical approach is needed in order to clarify undoubtedly what happens between the two loading models.

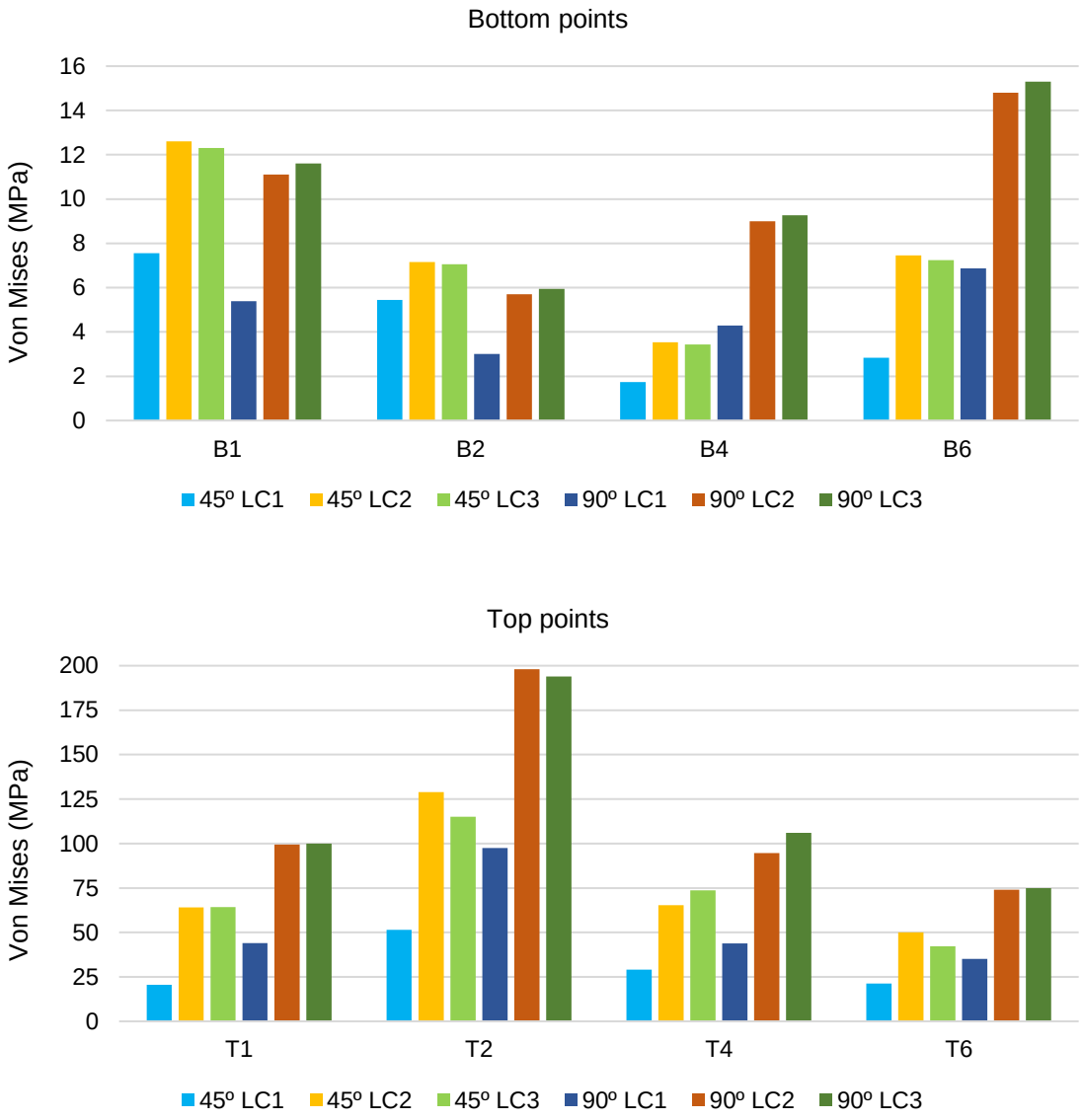

Figure 7.4. Von Mises stress (MPa) at four points from the top and four points from the bottom of the implant for LC1, LC2 and LC3, under a +45º and +90º load. For each point, the left three bars correspond to the +45º load, whereas the right three bars correspond to the +90º load. Each set of three bars in a row corresponds to LC1, LC2 and LC3, respectively.

Figure 7.4 highlights the Von Mises stress at four points at the top and four points at the bottom of the implant, under a +45º and a +90º load. There is a pattern consisting of a lower bar followed by two higher bars, corresponding to LC1, LC2 and LC3 models, respectively. LC2 and LC3 bars are relatively close to each other compared to LC1, which indicates that LC2 and LC3 have similar absolute stresses in comparison with LC1; this confirms the suspicion from the above paragraph that LC1 underestimates the stress the IAI.

Table 7.2 reports the average absolute and relative error of LC1 and LC2 compared to LC3. On the one hand, the absolute error is greater for top points than for bottom points, which is in agreement with what has been discussed when analyzing Table 7.1. Moreover, LC2 has less absolute and relative error when compared to LC1; on average, LC2 is about eight times more

accurate than LC1, when comparing to LC3 as an assumedly faithful reference for the stress distribution. Thus, it is established that LC2 is a significantly more realistic approach than LC1 to simulate a real implant with crown.

Table 7.2. Average absolute and relative errors of LC1 and LC2 compared to LC3. The "±" sign indicates that the results from -90º (-45º) and +90º (+45º) entered together in the average. Totals covering both angles were added to the relative error side.

Average absolute error (MPa)

Angle	±90º		±45º	
LC	LC1	LC2	LC1	LC2
Bottom	5.1	0.3	3.1	0.4
Top	67.5	7.5	51.5	9.0

Average relative error (%)

Angle	±90º		±45º	
LC	LC1	LC2	LC1	LC2
Bottom	53.3	3.6	46.0	6.5
Top	53.5	6.1	60.1	10.6

Total LC1 ≈ 53% ; Total LC2 ≈ 6.7%

Regarding Table 7.1, it is also important to discuss the results for the 0º load. One would expect that stress was very similar between LC1 and LC3, given that a 0º load is an axial load that would not contribute for the moment, as described for LC2, and therefore LC1 would be accurate enough to recreate LC3 in this condition. However, this important result shows that stress in LC1 is about 2.6 times less than in LC3 for top points. Thus, it suggests that even axial loads can cause a bending moment at the abutment, due to their slight misalignment from the abutment axis. Naturally this moment is smaller than that caused by buccolingual forces due to the normal distance between the center top of the abutment and the line of action of the axial component of the force being smaller than that for the buccolingual component of the force. Nevertheless, this indicates that adding an additional bending moment from axial loads would improve LC2. Therefore, by comparing the average error between ±90º and ±45º for LC2 in Table 7.2, it comes as no surprise that it is smaller for ±90º, because there is no axial component.

Nevertheless, an approximated eight-times reduction of the error from 53% to 6.7% for the more realistic non-axial loads (Table 7.2) indicates that the inclusion of a bending moments is mandatory for a more realistic analysis.

7.2 Stress distribution in single- and triple- surface occlusion

A comparison between models LC3 and LC4 allows understanding what is the effect of changing the occlusal surface from the buccal cusp alone to a wider surface including the buccal cusp and the mesial and distal fossae. Once again, 0º, +45º and +90º 100 N resultant forces were applied to each model, and Von Mises stress was evaluated at the implant. The results are shown in Figure 7.5. The most evident differences between LC3 and LC4 occur for the 0º load. Although the stress range is similar, for the LC3 case there is more stress at the buccal side of the neck of the implant, and at the lingual side of the bottom hexagon at the middle of the implant, whereas

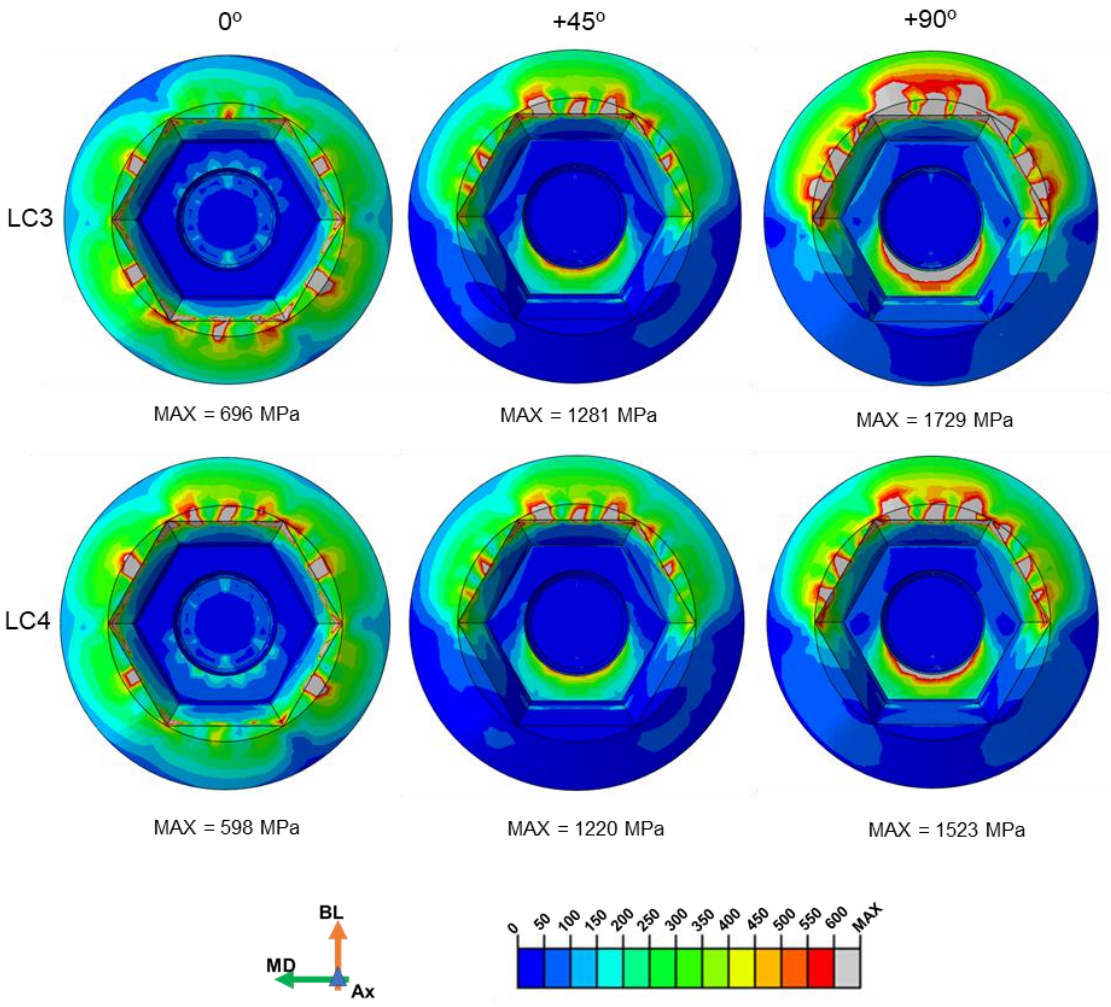

Figure 7.5. Comparison of the Von Mises stress at the implant for loading conditions LC3 and LC4, at 100 N forces with angles 0º, +45º and +90º. The global axis and scale at the bottom are equal for the six images. The maximum stress that delimits the grey area is below each image.

for the LC4 case, there is more stress at the lingual side of the neck of the implant, and at the buccal side of the bottom hexagon at the middle of the implant. This relates to the buccolingual coordinate of the point of application of the resultant force. LC3 has a single occlusion surface positioned in the buccal cusp. LC4 has three occlusion surfaces whose average buccolingual coordinate is on the lingual side. Therefore, when an axial load is applied, the top of the implant in LC3 (LC4) conditions will be loaded with more intensity on its buccal (lingual) side. On the other hand, for non-axial loads this difference does not exist, or at least is not so clear, because when the load angle increases, the axial component of the force decreases, and thus the effect of the buccolingual position of the resultant force on the stress outcome is more and more negligible.

In addition, the differences in the stress range between models is more visible for the +90º load case. For this load angle, although the stress distribution is very alike, the LC3 implant has higher stress than LC4, especially at the top of the abutment, which can be observed from the amount of red and grey areas corresponding to higher stress in this region. Oppositely to the previous case, the reason why this happens is that the axial coordinate of the resultant force, which contributes to the bending moment at the abutment. In the LC3 model, the single 100 N

force is applied at the top of the crown, at about 5.5 mm from the abutment, whereas in LC4 model, the two 33.3 N forces applied at the fossae (at 2.7 mm from the abutment) and the 33.3 N force at the buccal cusp result in a weighted height of 3.6 mm, which corresponds to a bending moment that is 65% of that in LC3. Thus, it is straightforward that a smaller moment from the buccolingual component in LC4 compared to LC3 will cause less stress as well.

7.3 Axial orientation of the implant body

The hexagonal connection between the implant and the abutment can be oriented in two ways: parallel or perpendicular to the buccolingual axis. To understand the difference between these two geometric configurations, a 100 N load was applied at a +45º and a +90º angle, using LC2 model. The resulting Von Mises stress is displayed on Figure 7.6 and 7.7, respectively. The

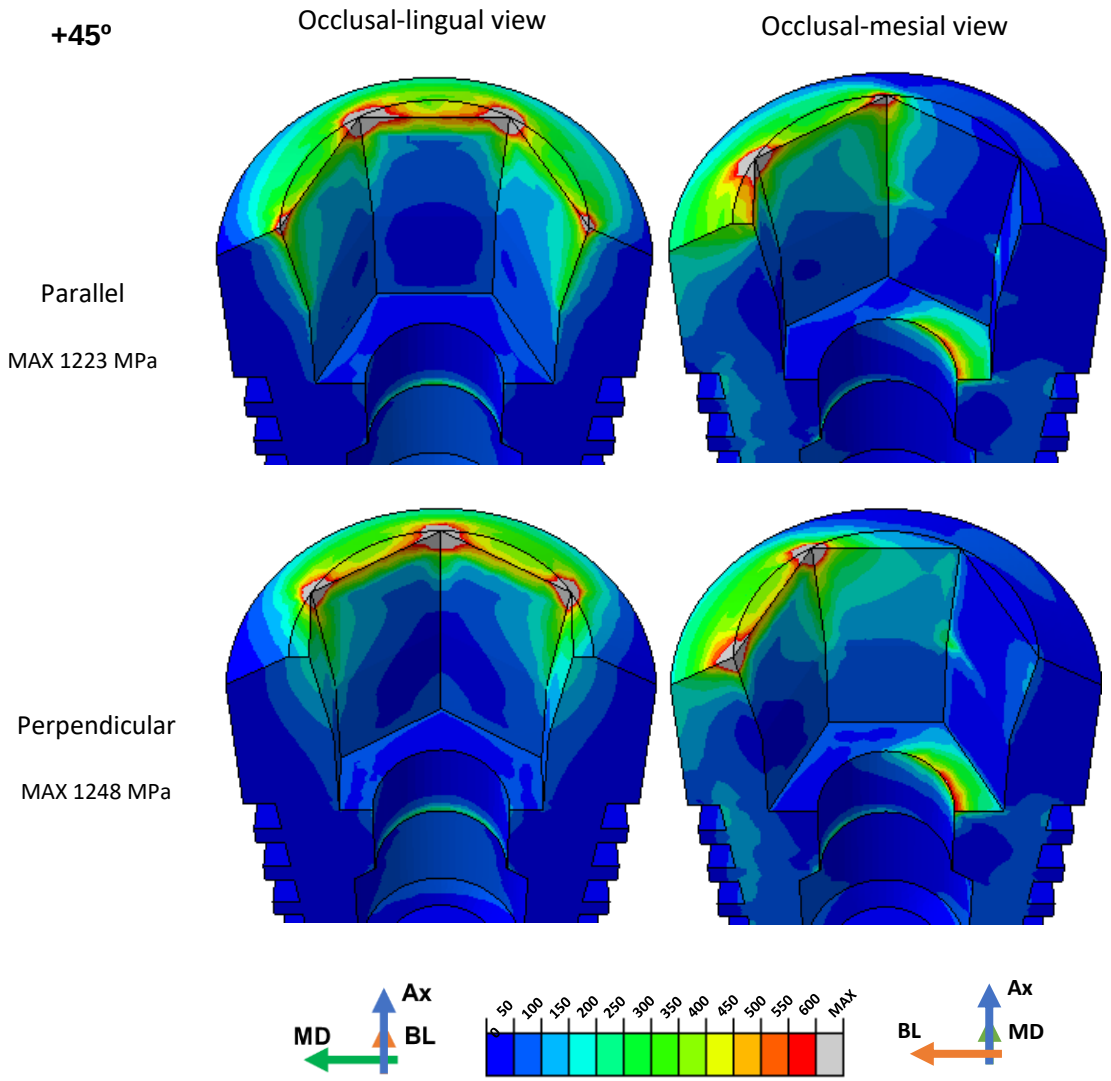

Figure 7.6. Comparison of the Von Mises stress at the implant between parallel- and perpendicular-oriented implants, under a 100 N, +45º load under LC2 conditions. (left) occlusal-buccal view and (right) occlusal-mesial view are displayed, with their respective global axes at the bottom. The color scale at the bottom is the same for the four images, and the maximum values are shown on the left below each label.

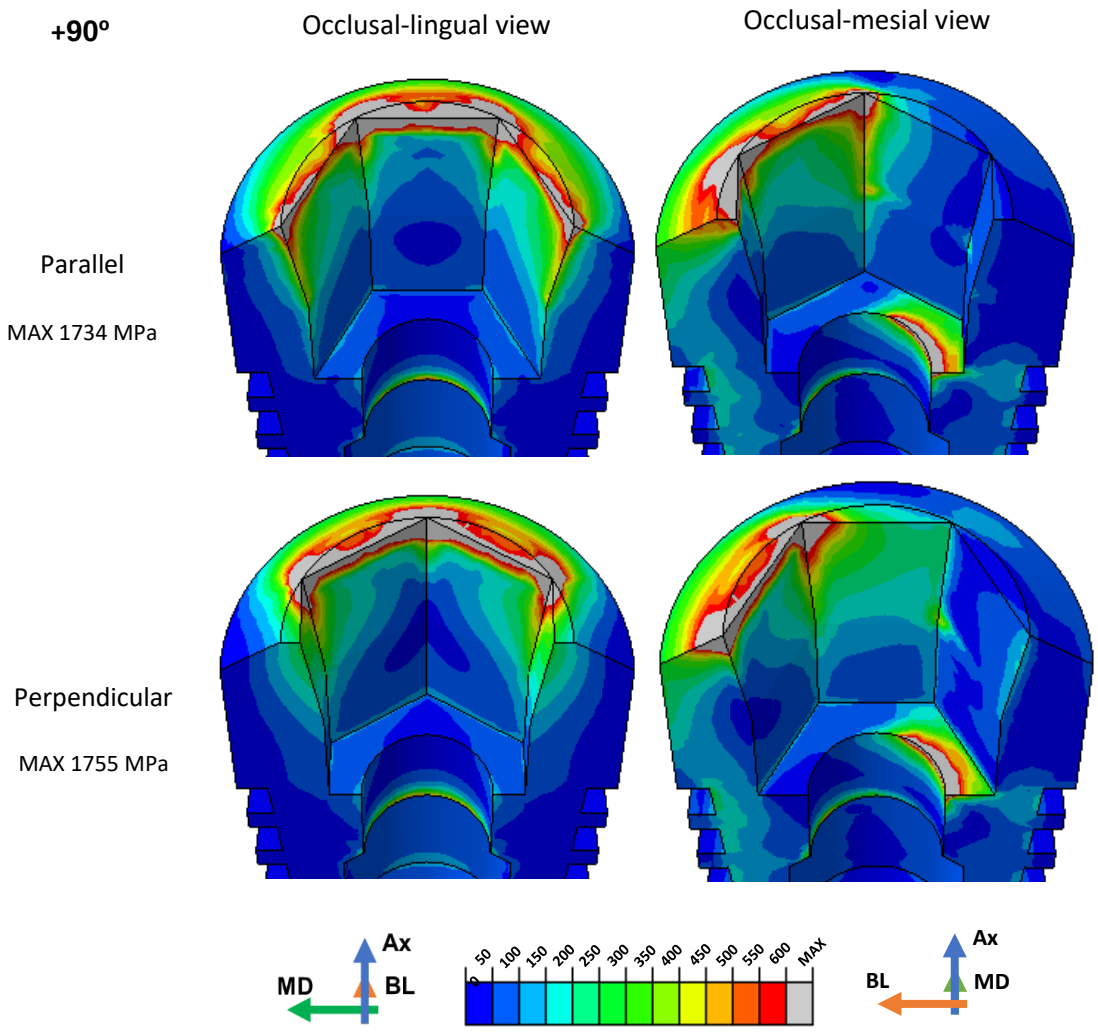

Figure 7.7. Comparison of the Von Mises stress at the implant between parallel- and perpendicular-oriented implants, under a 100 N, +90º load under LC2 conditions. (left) occlusal-buccal view and (right) occlusal-mesial view are displayed, with their respective global axes at the bottom. The color scale at the bottom is the same for the four images, and the maximum values are shown on the left below each label.

results are very similar between orientations, in a way that the stress distribution and its magnitude are nearly the same for parallel- and perpendicular-oriented implants regardless of the loading angle, as shown in both Figure 7.6 and 7.7. However, the number of edges of the top hexagon of the implant that are supporting higher stress is different between orientations. Taking Figure 7.7 as an example, three edges of the parallel-oriented implant are under higher stress (depicted as grey areas within the figure), whereas only two edges share higher stress in the perpendicular case. As a more uniform stress distribution means a more effective load transfer, it can be inferred that a parallel orientation might be a better design option. On the other hand, when looking from an occlusal-lingual view as on the left side of Figures 7.6 and 7.7, symmetry about the buccolingual axis is clear for both orientations. However, for the parallel case, the axis of symmetry divides the face at the center in two, whereas for the perpendicular case the axis of symmetry lies between two distinct faces. In other words, the stress distribution within a single

face is symmetric only for the parallel orientation. The piezoelectric sensor is a thin film attached to one or more of these faces. If the sensor is loaded uniformly over its area, then the output signal is more effectively generated than if the sensor is being applied different pressures at different locations. Thus, the parallel configuration can be a better configuration if the sensor is placed at the center face. Else, both configurations are very similar within the scope of this study.

7.4 Scoring of the points of interest

Von Mises stress, AVGAC stress and MAXAP stress were calculated at the twelve points of interest for the model LC4, under 100 and 300 N loads, at +0º, +15º, +30º, +45º, +60º and +90º angles. 2D plots relating these stress outputs to 1) the points of interest and to 2) the loading angle were made for each magnitude, region (bottom/top) and stress output. As the results are very similar between each stress output, only the results for Von Mises are shown, and the results for the remaining AVGAC and MAXAP stresses are included in Annexes II and III, respectively.

Firstly, the plots of the stress variation along the points of interest is discussed. Then, the stress variation with the load angle is analyzed.

The great similarity between the results for the points T2 and T3, as well as for the points T4 and T5, from symmetry about the buccolingual axis has been shown in the later sub-chapter, hence it will not be discussed further. However, it can still be observed on the following results, proving once more that the symmetry of the geometric model was not lost in the meshing process.

7.4.1 Stress along the points of interest

Figures 7.8 and 7.9 show the stress evolution along the bottom points of interest, for 100 N and 300 N loads, respectively. From B1 to B6 the curves corresponding to different angles do not behave similarly. For instance, at a 0º load, the stress is nearly constant among the points. However, increasing the angle from 0º to +45º results in a non-uniform stress distribution, and points closer to the lingual side of the surface present higher stress. However, when the +45º mark is crossed, and the load angle is increased from +45º to +90º, a vertical flip occurs and the points closest to the buccal side are now associated to higher stress. This is explained by the bottom location of these points. As the implant-abutment system makes a lever mechanism, when the top of the abutment is pushed horizontally towards the lingual side, its bottom moves on the opposite direction. Thus, the greater the buccolingual component of the force, which happens for greater angles, the greater will be the effect of the lever mechanism, and therefore the higher stress will be produced at the opposite direction. When the load angle is small, the lever mechanism is also small, so it can be neglected; thus, the stress distribution is simply dictated by the direction of the force. Since the force is pointing lingually, the stress is higher on the lingual side. Nonetheless, it must be understood that a strict interpretation of these results may not match the reality, due to the lack of statistical coherence for bottom points, as shown graphically by the apparently random stress distribution, and numerically further in sub-chapter 7.4.3.

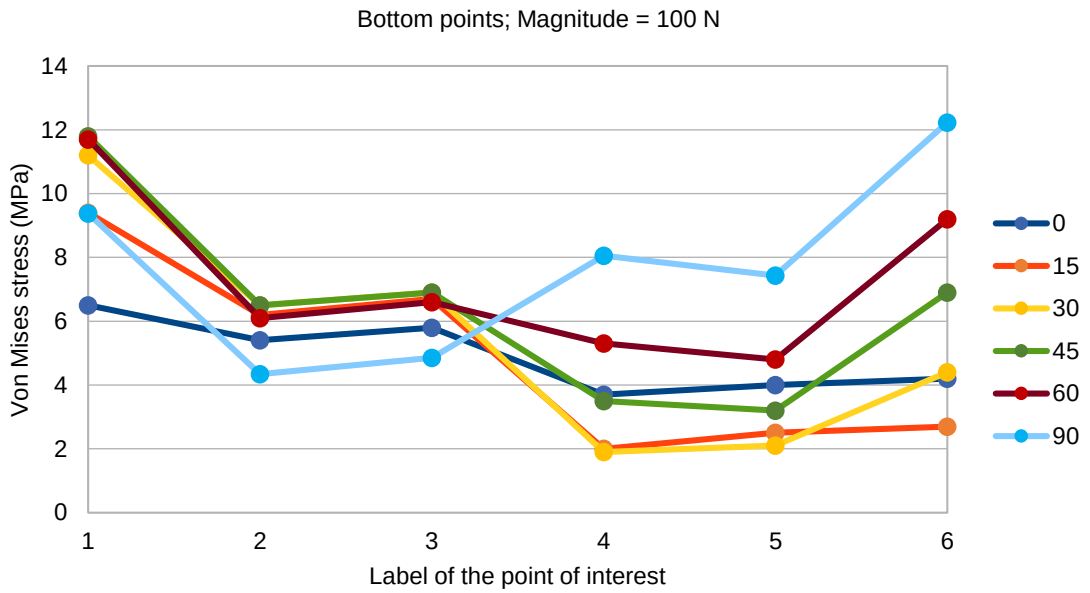

Figure 7.8. Von Mises stress at the bottom points of interest under a 100 N load at different angles. Load angles are displayed on the right in degrees.

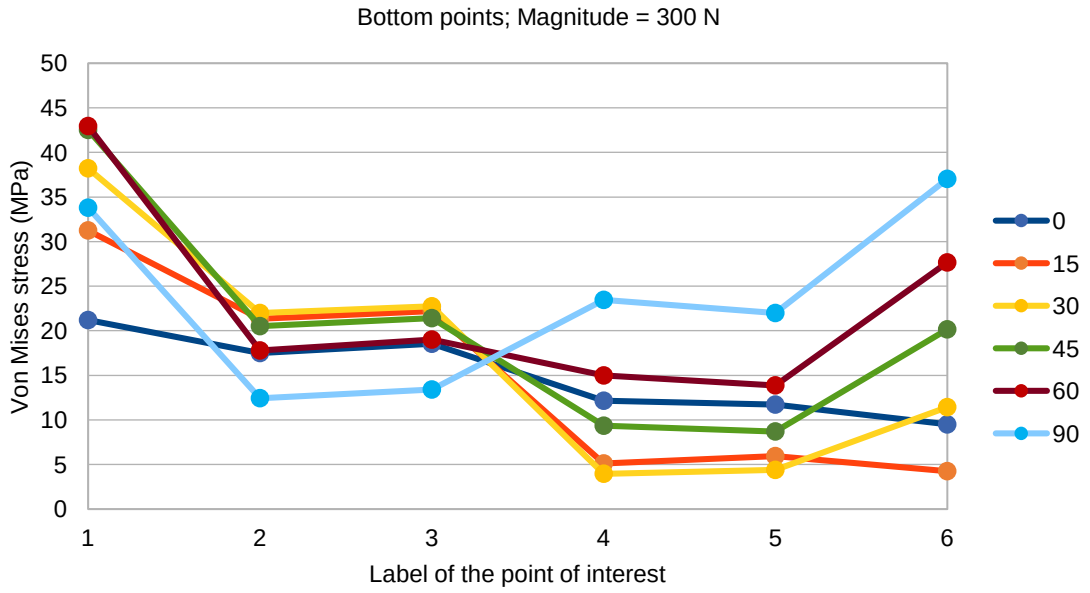

Figure 7.9. Von Mises stress at the bottom points of interest under a 300 N load at different angles. Load angles are displayed on the right in degrees.

Figures 7.10 and 7.11 show the stress evolution along the top points of interest, for 100 N and 300 N loads, respectively. Contrarily to the previous bottom points, top points present a more regular stress evolution, which is improved by increasing the magnitude. Once again, the 0º load generates a spatially uniform stress distribution. However, in this case, increasing the load angle from 0º to +90º produces a well-defined pattern in the top points. On the one hand, by observing one isolated curve (greater than 0º), one can see that the stress is higher at T2 and T3 and lower at T6; on the other hand, T1, T4 and T5 have similar stress, approximately equal to the average

of that at T2/3 and T6. Moreover, it can be observed that the curves corresponding to different load angles are vertically distributed with an approximately constant offset between each two, where the lower curve corresponds to the 0º load, and so on until the higher curve corresponding to the +90º load. This means that by increasing the load angle, the stress also increases, with the exception for point T6, which for low magnitudes may have a 0º load stress that is higher than the +30º load stress. However, the top points are readily assumed to be a better option to welcome a sensor, given the regularity and pattern they present under different loading conditions.

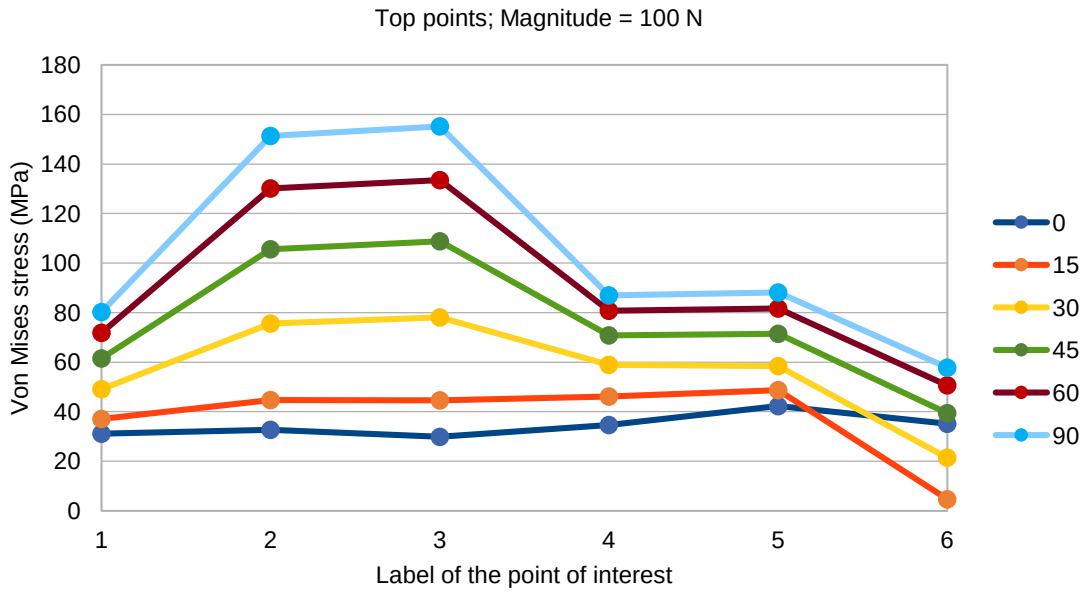

Figure 7.10. Von Mises stress at the top points of interest under a 100 N load at different angles. Load angles are displayed on the right in degrees.

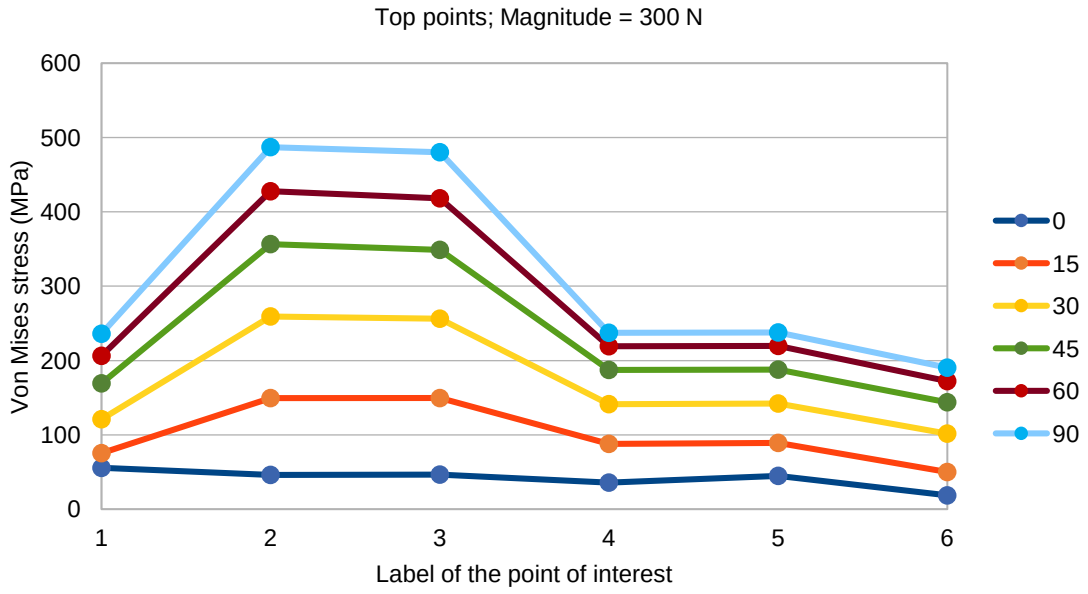

Figure 7.11. Von Mises stress at the top points of interest under a 300 N load at different angles. Load angles are displayed on the right in degrees.

7.4.2 Stress with the load angle

In the previous sub-chapter, it was analyzed how stress varies along the six points of interest for each region. However, it is also important to study the relation between stress and the load angle in depth.

Figures 7.12 and 7.13 show the stress evolution at the bottom points with varying load angle, under 100 N and 300 N loads, respectively. It was discussed before that the stress behavior for 0º–45º was different than for 45º–90º. This is much clearer in the figures, as the stress increases/decreases from 0º to 45º, and then decreases/increases from 45º to 90º, depending on the buccolingual coordinate of the points; curves of lingual points (T1–3) are concave, whereas curves of buccal points (T4–6) are convex.

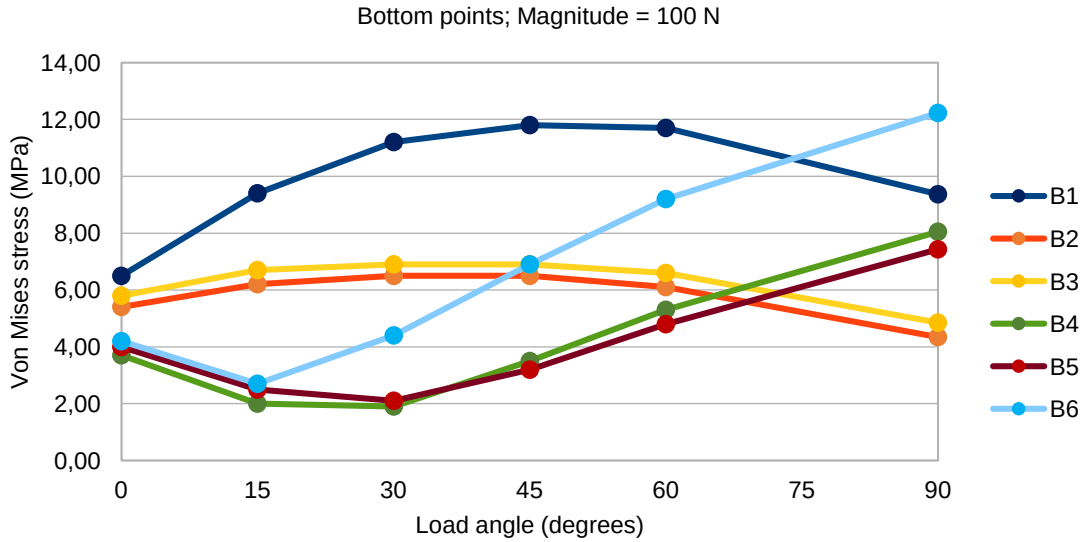

Figure 7.12. Variation of the Von Mises stress with the load angle under a 100 N load for the bottom points. Labels of the points are displayed on the right.

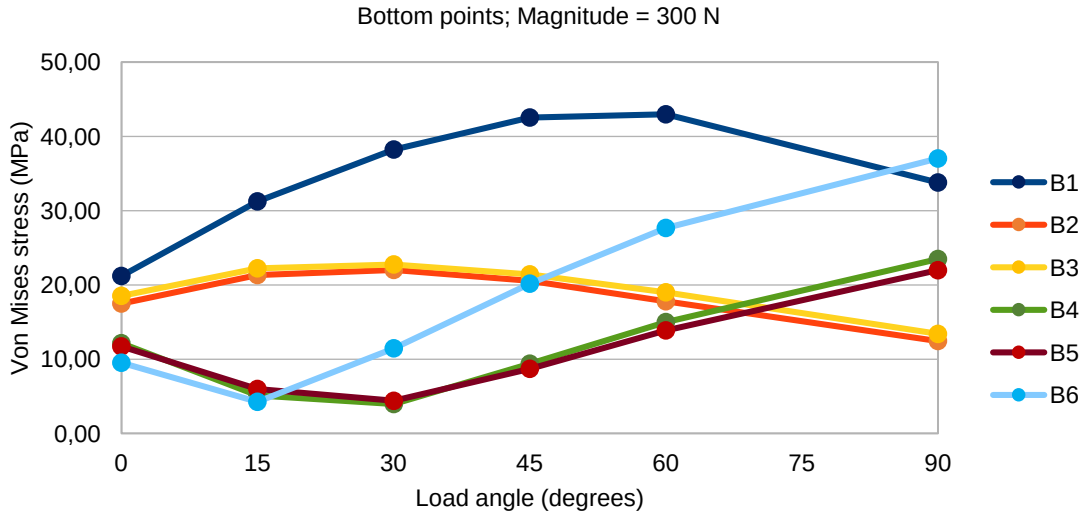

Figure 7.13. Variation of the Von Mises stress with the load angle under a 300 N load for the bottom points. Labels of the points are displayed on the right.

This makes the bottom points automatically inadequate to welcome the sensor, given that they will be exposed to non-monotonic stress, resulting in similar stress for different angles. In other words, for these points a higher stress would not imply a higher load angle, which may difficult or even disallow the input processing.

In turn, Figures 7.14 and 7.15 show the stress evolution at the top points with varying load angle, under 100 N and 300 N loads, respectively. Except for the point T6 under low magnitudes, the stress increases with the load angle. The slope is higher for points T2 and T3, thus they have a steeper stress response to the variation of the load angle. Furthermore, it can be inferred that by increasing the magnitude, point T6 starts increasing monotonically as well, in the light of the results for 300 N.

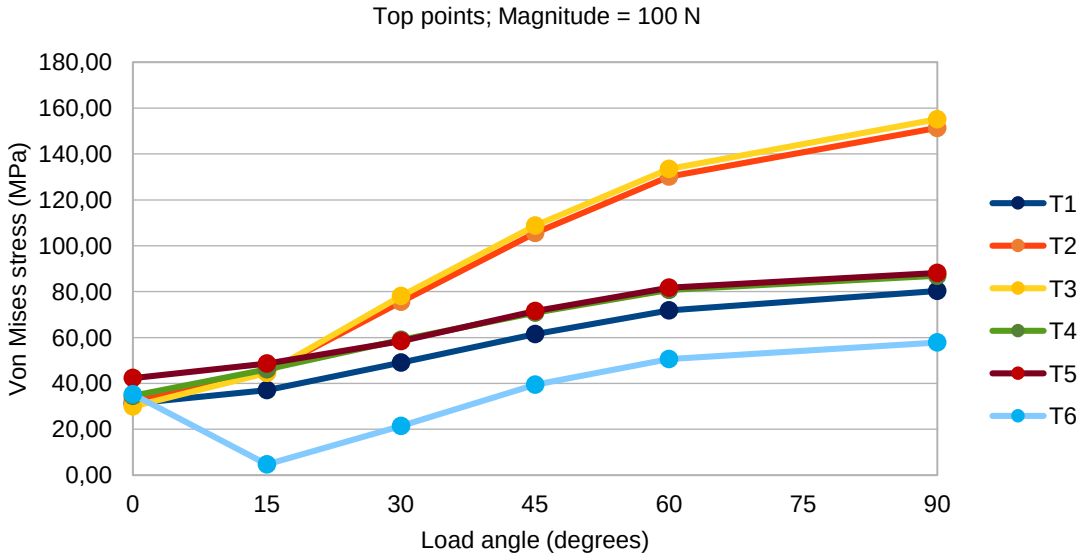

Figure 7.14. Variation of the Von Mises stress with the load angle under a 100 N load for the top points. Labels of the points are displayed on the right.

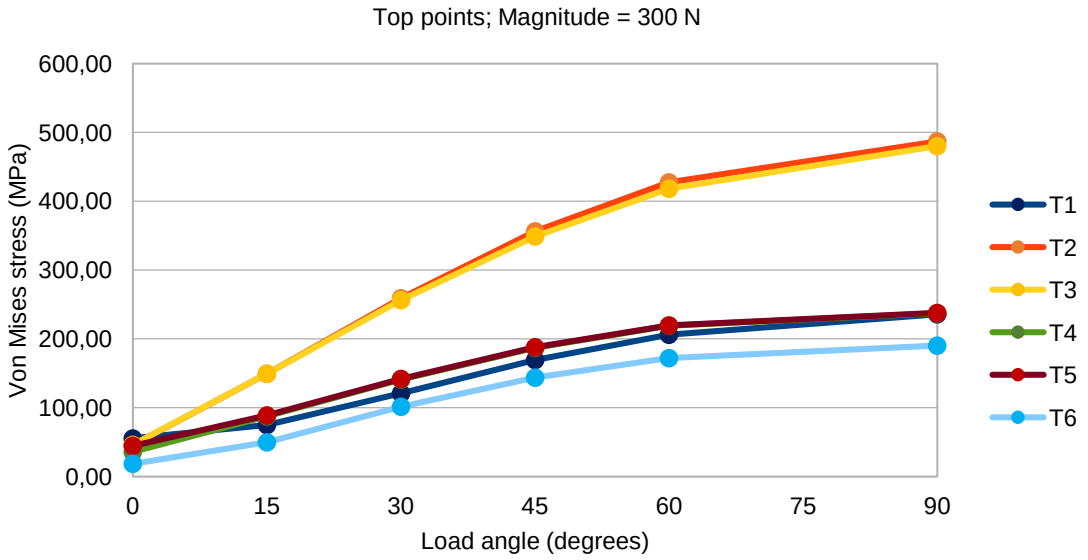

Figure 7.15. Variation of the Von Mises stress with the load angle under a 300 N load for the top points. Labels of the points are displayed on the right.

It is thus very suggestive that top points are great candidates to welcome the sensor, especially points T2/3, at which the stress increases steeply, comparing to the others, meaning that changes in the load direction can be better recognized by the sensor at these points.

Other very important result for top points is that the relation between stress and the load angle seems to be approximately linear, which would be a major advantage for the signal processing, as the stress variation would mirror the load angle variation. In order to assess this hypothesis, in the next sub-chapter, a numerical analysis considering linearity is carried out.

7.5 Linearity between stress and the load angle

Linear relations between two quantities *x* and *y* can be written in the simple form of a straight line equation

$$y(x) = mx + b \tag{7.1}$$

where *m* is the slope of the line and *b* is the y-intersect.

It has been discussed that stress appears to vary linearly with the load angle for top points. In order to test this hypothesis, each stress-load angle curve from Figures 7.12-15 (and the respective ones for AVGAC stress and MAXAP stress in annex) was fitted into a linear equation of the type of Equation 7.1 by means of a linear regression model. The results for points T2 and T3, as well as for points T4 and T5 were averaged, supported by the symmetry about the buccolingual axis of the model, continuously proved in the discussion of the previous results. Therefore, (3 stress outputs) x (2 load magnitudes) x (8 points) gave a total of 48 linear equations.

In order to ease the understanding of these linear equations, each one of the variables of Equation 1 was assigned a meaningful name. *y* is the stress output (*S*) at a given point (*P*), under a given load magnitude (*M*), and depends on the load angle (*θ*); *x* is the load angle; *m* is the sensitivity of that point to the load angle under that load magnitude ($SENS_{P,M}$); *b* is the stress output at that point for a 0º load under that load magnitude ($S_{0,P,M}$). Having this new nomenclature in mind, Equation 7.1 is then equivalent to Equation 7.2:

$$S_{P,M}(\theta) = SENS_{P,M}\,\theta + S_{0,P,M}$$

$$\begin{aligned} &S \in \{VM, MAXAP, AVGAC\}\ (MPa) \\ &M \in \{100, 300\}\ (N) \\ &P \in \{B1, B23, B45, B6, T1, T23, T45, T6\} \\ &0 \leq \theta \leq 90° \end{aligned} \tag{7.2}$$

$SENS_{P,M}$ and $S_{0,P,M}$ will be referred as *SENS* and S_0 for clarity. *SENS* and S_0 can be used together as a tool to aid the proper selection of the sensor features. *SENS* informs on the sensitivity of the sensor, thus is equal to 0 if the variation of the load angle does not affect the stress at a given point, and a high *SENS* means that the stress at that point is very sensible to

changes in the load angle; whereas S_0 is the stress for a 0º load, and thereby informs on the order of magnitude of the minimum stress that the sensor needs to be able to read. Both *SENS* and S_0 are different from point to point. There is a third parameter R^2 which is the coefficient of determination of the linear regression. It ranges from 0 to 1 and indicates the linearity of the original curve (R^2 is equal to 1 for perfect linearity).

Table 7.3 shows the coefficients of determination R^2. For bottom points, R^2 averages less than 0.6, whereas for top points it averages 0.86. Points T2/3 and T4/5 average 0.91. This means that stress at top points is significantly more linear than for bottom points, which has already been observed before. Furthermore, points T2/3 and T4/5 achieve the highest linearity compared to the rest, which makes them good candidates for welcoming the sensor. In addition, linearity increases for greater load magnitudes for point T6, which agrees to the discussion concerning this point in sub-chapter 7.4.1. Given their low R^2, bottom points cannot be meaningfully described by Equation 7.2, and therefore results for *SENS* and S_0 are shown for top points only.

Table 7.3. Coefficient of determination (R^2) of the linear regression equations. A color scale was added to each column: red and green were set to match the minimum and maximum values of the column, respectively.

Stress Output	Von Mises		Max Abs Principal		AVGAC	
Magnitude	100	300	100	300	100	300
B1	0,221	0,319	0,704	0,692	0,240	0,282
B2,3	0,214	0,425	0,002	0,576	0,413	0,273
B4,5	0,629	0,546	0,876	0,890	0,743	0,652
B6	0,897	0,905	0,972	0,954	0,948	0,927
T1	0,965	0,959	0,962	0,950	0,935	0,908
T2,3	0,963	0,942	0,967	0,948	0,979	0,964
T4,5	0,949	0,916	0,956	0,923	0,535	0,923
T6	0,563	0,925	0,498	0,924	0,174	0,923

Table 7.4 shows the results for *SENS*. On the one hand, T2/3 have the greater *SENS* among the top points, confirming the that T2/3 are more sensitive to the load angle than the rest. On the other hand, *SENS* of T4/5 is on average three times smaller than that for T2/3. This means that, for positive-angled loads, stress at both T2/3 and T4/5 increases linearly with the angle, and three times as fast for T2/3. By buccolingual symmetry, for negative-angled loads, the stress increases three times as fast for T4/5 compared to T2/3.

Table 7.5 shows the results for S_0. On the one hand, it should be the same among the top points, as an axial load results in a uniform stress distribution. However, it has been already observed that, given the occlusal surface of LC4, lingual points may have higher stress at 0º loads, this being clearer for loads with greater magnitude. This is verified in Table 5, as higher S_0 are reported to lingual points for the 300 N load.

Table 7.4. *SENS* of the linear regression equations for the top points. A color scale was added to each column: red was set to match *SENS*≤0.10 and green was set to be the maximum value of the column.

Stress Output	Von Mises		Max Abs Principal		AVGAC	
Magnitude	100 N	300 N	100 N	300 N	100 N	300 N
T1	0,59	2,18	0,71	2,78	0,32	1,25
T2,3	1,47	5	1,66	5,68	0,67	2,42
T4,5	0,58	2,28	0,51	2,23	0,09	0,73
T6	0,45	2,03	0,44	2,05	0,1	0,68

Table 7.5. S_0 of the linear regression equations for the top points. A color scale was added to each column: red and green were set to match the minimum and maximum values of the column, respectively.

Stress Output	Von Mises		Max Abs Principal		AVGAC	
Magnitude	100	300	100	300	100	300
T1	31,61	56,69	34,18	49,39	21,68	32,87
T2,3	32,19	85,5	36,73	81,04	20,13	24,03
T4,5	40,87	61,31	43,64	59,42	18,61	21,1
T6	16,87	31,46	19,46	35,3	10,85	15,43

It is vital to remind that the values for *SENS* and S_0 were obtained for positive-angled loads. The buccolingual symmetry that was discussed on later sub-chapters implies that the results for points T1 and T2/3 for positive-angled loads are nearly the same as those for points T6 and T4/5 for negative-angled loads, respectively. Hence, if a high *SENS* was reported to points T2/3, the same value would be reported for points T4/5 for negative-angled loads, and if a low *SENS* was reported to points 4/5, the same value would be reported for points T2/3 for negative-angled loads. Therefore, this symmetry is the key factor for choosing the points T2/3 and T4/5 together as the final candidates to welcome the piezoelectric sensors. T2/3 is more sensitive to positive-angled loads, whereas T4/5 is more sensitive to negative-angled loads.

In order to transform Equation 7.2 into a more general equation describing the Von Mises stress at a given point, the dependency on the load magnitude can be interpreted differently, passing *M* as a second argument of the equation. Because the materials are linear elastic, the magnitude of the load is assumed to act merely as a scale factor. Therefore, the stress outcome can be thought as a product composition of two functions $f_P(\theta)$ and $g_P(M)$, which describe the load angle and the load magnitude effect on the stress outcome:

$$VM_P(\theta, M) = f_P(\theta) g_P(M) = \left(SENS1_P(\theta)\,|\theta| + VM_{0,P}\right) SENS2(M) \quad (7.3)$$

$$P \in \{T23, T45\}$$

$$0° \leq \theta \leq 90°, M \geq 0\ N$$

SENS1$_P$ (θ) is the step-function that has only two values, one for negative load angles, and other for positive load angles, based on the results shown on Table 7.4. *SENS2*(*M*) is the scale factor which describes the magnitude influence on the stress outcome, which must be equal to zero if there is no load (*M* = 0 *N*). Figure 7.16 illustrates *SENS1* and *SENS2*(*M*). $VM_{0,P}$ times *SENS2*(*M*) is the Von Mises stress at a 0º load of magnitude *M*, and it is similar between the two points, as discussed on sub-chapter 7.1.

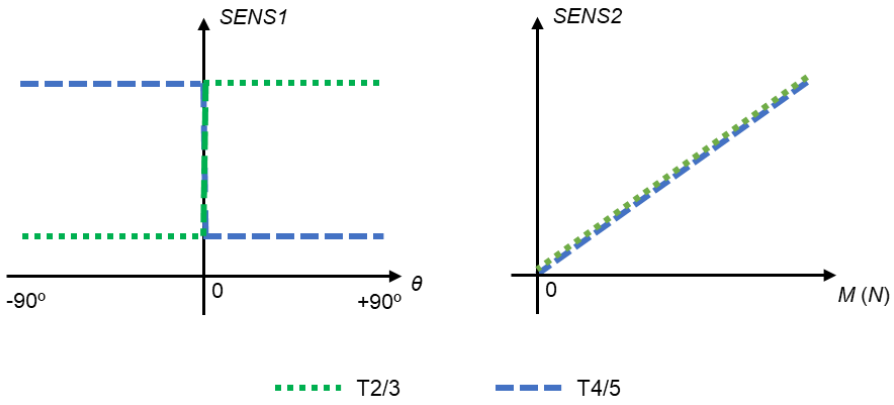

Figure 7.16. Schematic representation of parameters *SENS1* and *SENS2*. (left) *SENS1* depends on the point; for negative (positive) load angles, point T4/5 has higher (lower) sensitivity to the load angle than T2/3. (right) *SENS2* is linear monotonic because linear isotropy is assumed for all materials.

7.5.1 Combination of the stress outputs into a single signal

The electrical signals from the piezoelectric sensors at T2/3 (say, S^+) and T4/5 (say, S^-) are directly proportional to the stress, and may be combined into a single output signal whose properties are related to the load angle and magnitude. As S^+ is bigger than S^- for positive load angles, and S^- is bigger than S^+ for negative load angles due to the load sensitivity of points T2/3 and T4/5, the most natural way to combine them would be a simple differential signal S_{DIFF} equal to S^+ minus S^-. Other possibility is to divide S^+ by S^- giving an output S_{QUO}.

According to Equation 7.3 and the definition of S_{DIFF},

$$\begin{aligned} S_{DIFF}(\theta, M) &= S_+ - S_- \propto VM_+(\theta, M) - VM_-(\theta, M) \\ &= \Big(\big(SENS1_+(\theta) - (SENS1_-(\theta)\big)|\theta| + (VM_{0,+} - VM_{0,-}) \Big)\, SENS2(M) \\ &\approx \big(SENS1_+(\theta) - (SENS1_-(\theta)\big)|\theta|\, SENS2(M) \end{aligned} \qquad (7.4)$$

From Equation 7.4 and Figure 7.16, S_{DIFF} is deduced to have the same sign as the load angle. For a 0º load, S_{DIFF} is approximately 0. Furthermore, under loads of static magnitude, the absolute value of S_{DIFF} increases linearly with the load angle. Also, as it would be expected, under static angles, increasing the magnitude of the load also increases S_{DIFF} linearly. The major advantage of considering S_{DIFF} is that it is easily configured, and that if one of the properties of the load is static, the other can be linearly detected. However, as its value can increase due to changes in both direction and amplitude of the load, it may not be ideal under fully dynamic loads.

According to Equation 7.3 and the definition of S_{QUO},

$$S_{QUO}(\theta, M) = \frac{S_+}{S_-} \propto \frac{VM_+(\theta, M)}{VM_-(\theta, M)}$$

$$= \frac{SENS1_+(\theta)\,|\theta| + VM_{0,+}}{SENS1_-(\theta)\,|\theta| + VM_{0,-}} \tag{7.5}$$

$$\approx \frac{SENS1_+(\theta)\,|\theta| + VM_0}{SENS1_-(\theta)\,|\theta| + VM_0}$$

From Equation 7.5, it is straightforward that S_{QUO} does not depend on the load magnitude as the parcels *SENS2*(*M*) cancel each other. Moreover, for a 0º load angle, S_{QUO} is approximately 1. For positive load angles, as $SENS1_+$ is greater than $SENS1_-$, S_{QUO} is greater than 1. The same reasoning can be done for negative load angles, where S_{QUO} is smaller than 1 in a proportional way. Furthermore, it can be inferred that for higher angles, S_{QUO} becomes closer to $SENS1_+/SENS1_-$, which is a constant with only two different values, one greater than 1 and other that is its inverse, for positive and negative load angles, respectively. S_{QUO} is thus not able to detect changes in the load magnitude but may serve the detection of the sign of the load angle and even its value, although in a less clear way compared to in S_{DIFF}, where the relation was linear. Therefore, if the load is expected to be highly dynamic in both direction and magnitude, S_{QUO} might be employed rather than S_{DIFF}.

The next sub-chapter uses dynamic loads in order to assess the choice of T2/3 and T4/5 as the most suited candidates to welcome the sensor, and a brief analysis on the applicability of S_{DIFF} and S_{QUO} is also done.

7.6 Assessment of points T2/3 and T4/5 using dynamic loads

The later sub-chapter indicated that points T2/3 and T4/5 have a linear stress response to the load angle, and the load magnitude was also inferred to have a linear relationship to the stress outcome at each point. Two different output signals combining the outcomes for these two points were proposed in order to detect changes in the bite load. Von Mises stress at points T2/3 and T4/5 and the resulting S_{DIFF} and S_{QUO} were analyzed for the LC4 model under dynamic loading.

7.6.1 Dynamic load 1: static magnitude, dynamic angle

Figure 7.17 shows the Von Mises stress at the top points under dynamic load DYN_1, which confirms the hypothesis that points T2/3 and T4/5 have the most linear response to the load angle as they have the stress curve that most resembles the load angle curve, displayed on Annex I. Furthermore, stress at T2/3 is higher than at T4/5 for positive angles (0≤t≤1 s) and the difference between them increases and decreases with the angle. The opposite happens between T4/5 and T2/3 for negative angles, again confirming the buccolingual symmetry of the stress at the top points when the sign of the angle is reversed. Moreover, points T1 and T6 are displayed, and the

lower linearity of the point T1 at positive load angles and of the point T6 at negative load angles predicted on Table 7.3 is visible on Figure 7.17.

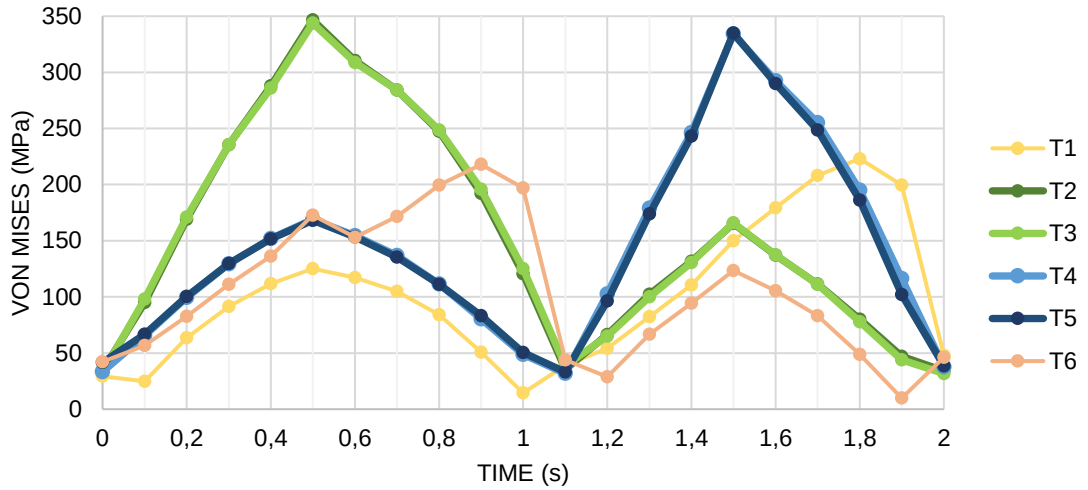

Figure 7.17. Von Mises at the top points under load DYN_1. The curves for T2/3 and T4/5 are highlighted.

Figure 7.18.1 and 7.18.2 show the output signals S_{DIFF} and S_{QUO} for DYN_1, respectively. As expected, the sign of S_{DIFF} agrees with that of the load angle and increasing the load angle also increases S_{DIFF}. On the other hand, S_{QUO} is bigger than 1 for positive angles and smaller than 1 for negative angles. However, the shape of the S_{QUO} curve does not resemble that of the load angle, having a step shape instead. This agrees with the analysis done for Equation 7.5, whereby increasing the load angle was assumed to take S_{QUO} to a constant value equal to the ratio $SENS_+/SENS_-$. Therefore, the variation of the load angle can be detected only for lower angles. However, the sign of the load angle may be accessed by S_{QUO} regardless the load angle.

Nevertheless, when the load is semi-static, S_{DIFF} is indicated to be a much better option to detect changes in the dynamic component of the load.

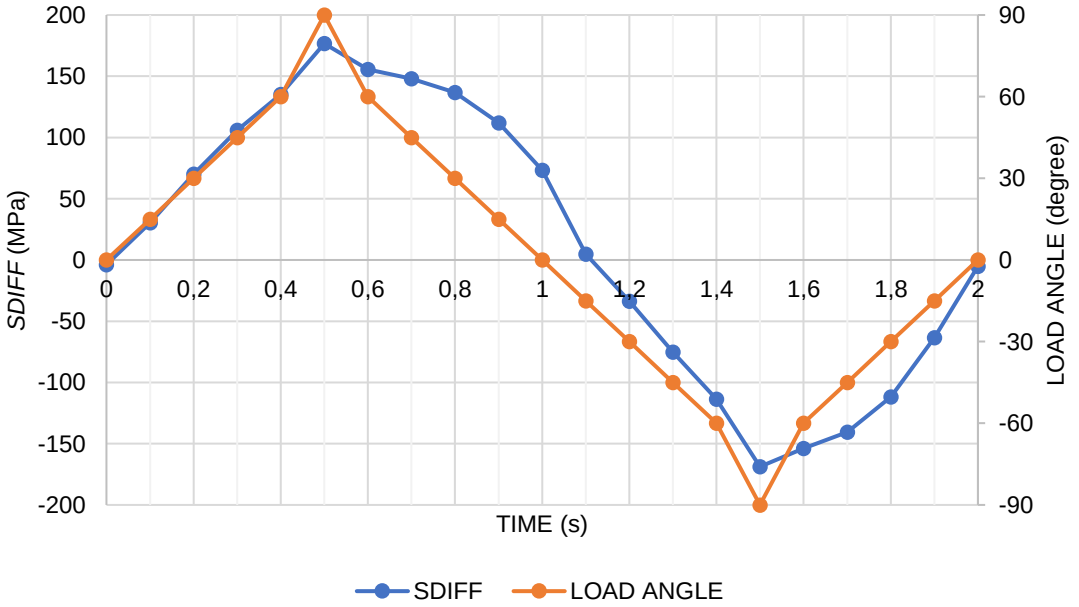

Figure 7.18.1 S_{DIFF} for dynamic load DYN_1. Load angle is displayed for comparison to the output signal.

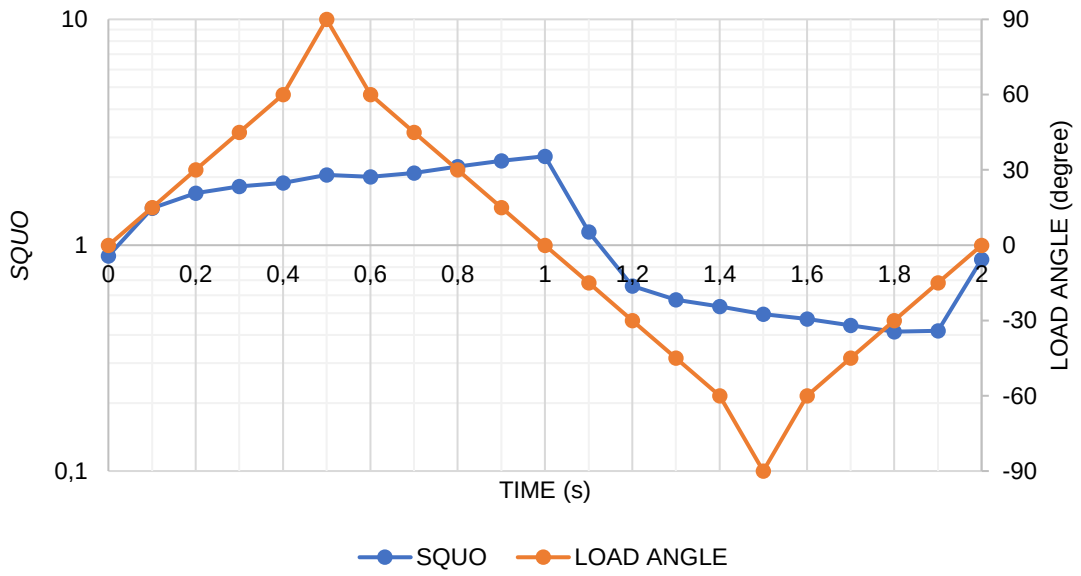

Figure 7.18.2 S_{QUO} for dynamic load DYN_1. Load angle is displayed for comparison to the output signal.

7.6.2 Dynamic load 2: dynamic magnitude, dynamic angle

It was discussed that the stress response under static magnitude loads was easily assumed to be linear, because the stress-load angle study carried out in the sub-chapter 7.4.2 was also done under one constant load magnitude. However, by changing the magnitude of the load, the stress also changes, which affects the stress response curve, modelled as a simple linear function of the load angle (Equation 7.2), into a more complex global expression involving both the load angle and the magnitude (Equation 7.3). The results for Von Mises stress at the top points are shown on Figure 7.19. On the one hand, the same conclusions for the applicability of T2/3 and T4/5 opposite to T1 and T6 for DYN_1 are applied in this case for DYN_2, that is, T2/3 and T4/5 have the most linear response to the load angle. Secondly, the stress magnitude at these points decreased compared to DYN_1. This is due to the magnitude profile of the load, which decreases

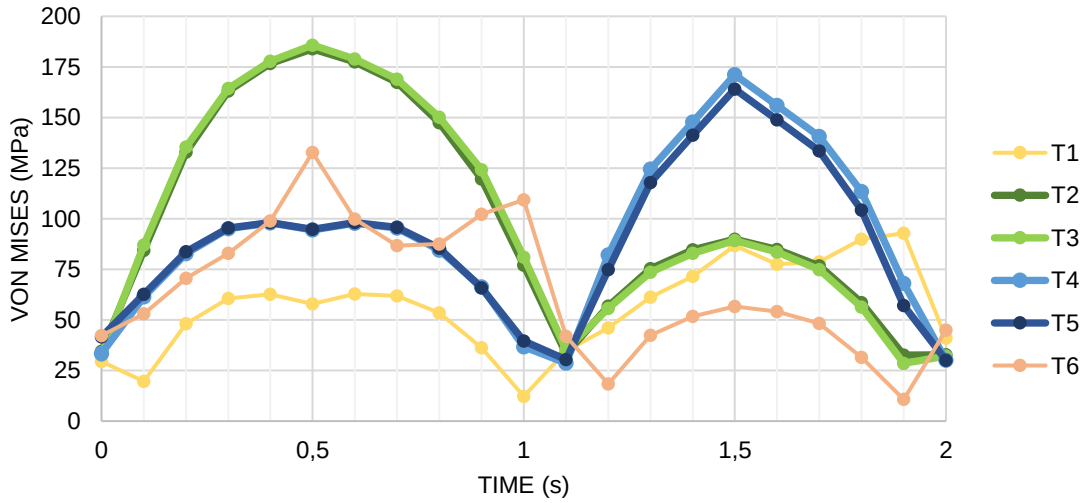

Figure 7.19. Von Mises at the top points under load DYN_2. The curves for T2/3 and T4/5 are highlighted.

from 200 N to 100 N at 0–0.5s and at 1–1.5s (Annex I). As the magnitude profile is symmetric in each one of the two steps, the stress response to the load angle remains uncorrupted in a way that the stress is again higher for higher load angles. This can be observed on Figure 7.20.1, which shows the output signal S_{DIFF} in the DYN_2 case.

S_{DIFF} is positive for positive angles and negative for negative angles, and it increases and decreases in agreement with the load angle, although the absolute value of S_{DIFF} is reduced comparing to DYN_1, again in conformity with the load magnitude decrease. Nevertheless, it is important to discuss what would happen if the magnitude of the load was not symmetric within each step and, for instance, it was continuously decreasing from 200 N to, say, 0 N in each step. As the magnitude functions as a scale factor to the stress, the stress curve would not be symmetric anymore and the right side of the parable that can be seen for T2/3 at 0–1s would not be similar to the left side. Because of the continuously decreasing magnitude, the right side of the parable would decrease, but faster. This rapid decrease could erratically lead to the interpretation that the load angle was also decreasing faster than for the left side. This is the major concern

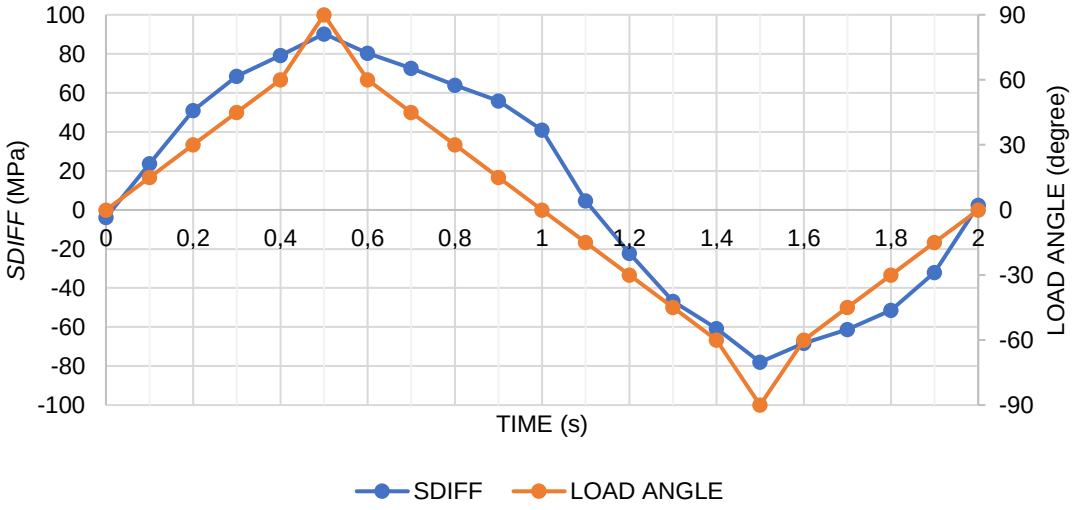

Figure 7.20.1 S_{DIFF} for dynamic load DYN_2. Load angle is displayed for comparison to the output signal.

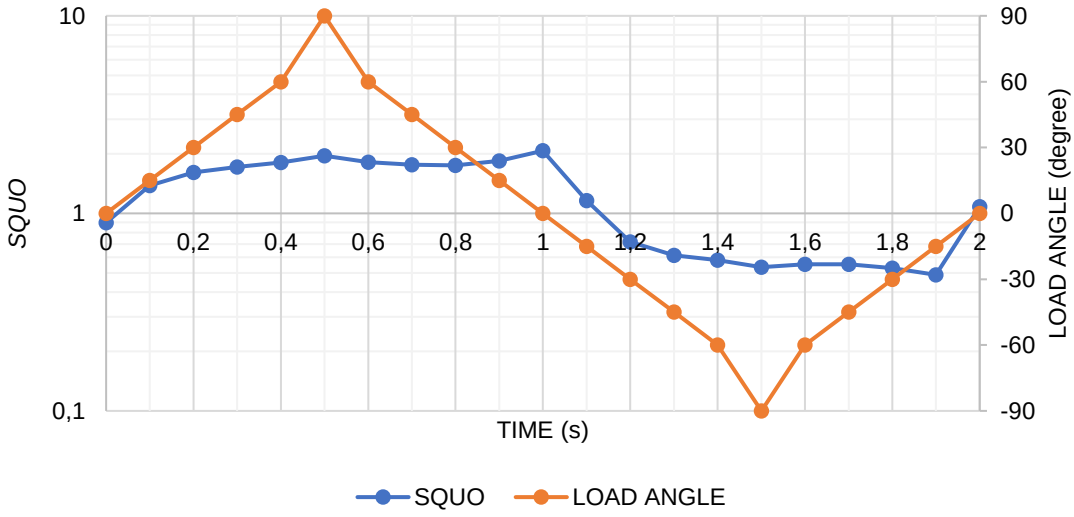

Figure 7.20.2 S_{QUO} for dynamic load DYN_2. Load angle is displayed for comparison to the output signal.

when dynamic magnitude is considered, with S_{DIFF} being affected by both the load angle and the magnitude variation. Figure 7.20.2 shows the output signal S_{QUO} in the DYN_2 case. As for S_{DIFF}, the interpretation of S_{QUO} remains similar to that done for DYN_1, with values higher than 1 meaning positive angles and values smaller than 1 meaning negative angles.

The big difference between S_{QUO} and S_{DIFF} is that the values for S_{QUO} are closer to each other between DYN_1 and DYN_2 compared to S_{DIFF}. As only the magnitude changes from DYN_1 to DYN_2, it is safe to assume that S_{QUO} is considerably less sensitive to the magnitude than S_{DIFF}, which in turn suggests that the assumption made for Equation 7.3, in which the stress function is just a product composition between an angle-sensitive factor and a global magnitude-sensitive factor is correct. Thus, several output signals may be chosen accordingly to the objective of the sensor and the expected loading conditions at the tooth. If static magnitudes or static angles are expected, S_{DIFF} is sufficient to read changes in the load direction and magnitude, respectively. In the case of full dynamic loads, more complex algebraic combination of the signals from T2/3 and T4/5 may be required to isolate the desired properties.

7.6 Summarized discussion

The stress distribution reflected the symmetry of the model about the buccolingual axis, hence proving that points with the same buccolingual coordinate can be inferred to have the same outcomes within the study. Additionally, the asymmetry about the mesiodistal axis introduced by the crown in LC3 and LC4 is neglected for high load angles, and close results can be expected between lingual points under a given positive (negative) load angle and the corresponding buccal points on the other side of the mesiodistal axis under the opposite negative (positive) load angle.

Regarding the comparison between the models LC1 and LC2, Von Mises stress at the IAI was considerably smaller in the first overall. Moreover, an averaged 6.7% relative error was calculated for LC2, against 53.2% in LC1. Therefore, it becomes clear that if one chooses not to include the crown in the model, it should be replaced by a bending moment at the abutment, in order to better simulate the effect of loading the crown in the complete model.

The stress distribution for LC3 and LC4 was very similar regardless the load angle, although higher stress at the implant-abutment interface was reported for LC3 at greater load angles. The main consideration when choosing LC3 or LC4 is the axial coordinate of the resultant force together with the magnitude of the buccolingual component, which are both included in the production of the bending moment at the abutment, which in turn will increase the stress at the interface with the implant. The greater the axial coordinate and the magnitude, the greater the moment and higher the stress.

The analysis of the stress at the points of interest included a graphical and numerical approach, followed by a linear model to represent the stress variation with the load angle. The bottom region may not be adequate to welcome the sensor due to the low linearity of the results. On the other hand, points T2 and T3 of the top region had great linearity and a distinctive

sensitivity to varying load angles. In addition, points T4 and T5 also demonstrated good linearity and a smaller sensitivity compared to the later.

The selected points demonstrated great applicability under semi-static load, with faithful stress response to the load angle and magnitude. However, for full dynamic loads, a more complex sensor configuration might need to be developed in order to isolate the magnitude information from the angle information.

Chapter 8

Conclusions and future work

8.1 Conclusions

The present work achieved with success each one of the proposed goals. The innovative objective suggestion of locations within the IAI to place the piezoelectric sensor, together with insightful examples on how the signals arising from these sensors may be combined in order to obtain a meaningful output that informs on the properties of the bite forces, were the main results of this work. In addition, a profound analysis on the influence of geometry and loading conditions on the stress distribution at the implant allowed robust description of the advantages and limitations associated to the modeling of the crown and occlusal area, which should be considered by investigators of the computational implant dentistry field.

In the first place, this worked demonstrated that the decision of not including the crown in the model does not retrieve unfaithful results as long a bending moment is added to the abutment, whose magnitude and direction are in conformity with that of the bite forces. If both the crown and a bending moment are not considered, stress may be severely underestimated depending on the loading conditions.

Secondly, if the crown is included in the model, the occlusal area should not be arbitrarily chosen, as a wider occlusal area may result in decreased stress at the top of the implant. If more data on the real physiologic occlusal area can be accessed from a given tooth or patient, it should be encouraged in order to obtain more accurate results.

Finally, this work provided solid evidence that the top region of the IAI has a linear stress response to the bite force angle and magnitude, namely at points T2/3 and T4/5, which strongly suggests that if one or more sensors are to be placed at this region, signals from each sensor can be combined into a meaningful output signal that is closely related to the bite force properties.

This pioneering result represents a substantial breakthrough in the field of smart dental implants, enforcing the possibility and viability of the development of an implant prototype with integrated piezoelectric sensors at the IAI.

8.2 Future work

This work has some limitations that need further developments to be overcome and even more faithful results and conclusions can be obtained. From the FE modeling of the dental implant to the selection of the target regions, there are some details that could be improved with more exhaustive and refined investigation, although the simplifications used in this study are justified and serve the purpose of the work.

Regarding the geometry of the crown and the possibility of replacing this component with a bending moment acting on the abutment, one could conduct a comparative study where models of standard dental implants of the four different types of tooth (incisive, canine, premolar and molar) would be under a set of different physiological loads with varying magnitudes and directions, with the objective of explicitly define the bending moment that would have to be applied to the center of the abutment in order to recreate the effect of the crown. Although this study has already given valuable insight on what the factors that define the moment are, a more global and stronger conclusion could be achieved if the geometry of the crown was retrieved from imaging techniques, and different types of crown were studied.

Concerning the occlusal area and the mastication cycle, most models diverge from each other which makes it harder to choose loading conditions with real physiological significance. Thus, a statistical study evaluating the occlusion in a group of healthy people with the objective of defining the principal occlusal areas and the direction and magnitude of the bite force at those areas would provide prized knowledge used by FE investigators when modeling mastication.

Moreover, one may refer the choice of not including the piezoelectric sensors together with the implant on this model as a huge limitation of this work. In truth, it seems straightforward that the introduction of new components in the model could change the stress distribution at their locations. However, given the micro and nano dimensions of sensors in the market, together with their thin film geometry, suggests that the stress at their surfaces would not change drastically from that observed at the internal walls of the implant, from where the points of interest were extracted. Nevertheless, the modeling of these structures is encouraged for further studies, and perhaps together with the circuitry box where the signal from the sensor is processed and wireless sent to the stimulation unit by the alveolar nerve branches. One suggestion is that the circuitry is integrated in the implant body in a way that only the sensor is left outside at the implant-abutment interface.

Bibliography

[1] Joseph, Angel & Joseph, Suja & Mathew, Nicholas & Koshy, Ashwin. (2018). Small things have a big impact: new trends in implant dentistry. The Libyan Dental Journal. 8.

[2] Gaille, B. (2018, August 5). 17 dental implant industry statistics and trends. Report retrieved from http://brandongaille.com/17-dental-implant-industry-statistics-and-trends

[3] Sadowsky, Steven. (2019). Occlusal overload with dental implants: a review. International Journal of Implant Dentistry. 5.

[4] Pereira, B. (2018). Dental Pressure Detection and Nerve Stimulation Demonstration Prototype. Faculdade de Engenharia da Universidade do Porto, Porto, Portugal.

[5] Mosby's Medical Dictionary, 9th edition. © 2009, Elsevier. Retrieved September 11, 2019 from https://medical-dictionary.thefreedictionary.com/stomatognathic+system

[6] Tooth. (2018). In Encyclopaedia Britannica Online. Retrieved September 11, 2019 from https://www.britannica.com/science/tooth-anatomy

[7] Christensen, A. M., & Passalacqua, N. V. (2018). Osteology and Odontology. A Laboratory Manual for Forensic Anthropology, 7–34.

[8] Dean, R. (2017). The periodontal ligament development anatomy and function. Oral Health and DEntal Management 16(6).

[9] Brand, R. (2017). Anatomy of Orofacial Structures E-Book: A Comprehensive Approach.

[10] Trulsson, M. (2006). Sensory-motor function of human periodontal mechanoreceptors. Journal of Oral Rehabilitation, 33(4), 262–273.

[11] Piancino, M. G., Isola, G., Cannavale, R., Cutroneo, G., Vermiglio, G., Bracco, P., & Anastasi, G. P. (2017). From periodontal mechanoreceptors to chewing motor control: A systematic review. Archives of Oral Biology, 78, 109–121.

[12] Türker, K. S., Sowman, P. F., Tuncer, M., Tucker, K. J., & Brinkworth, R. S. A. (2007). The role of periodontal mechanoreceptors in mastication. Archives of Oral Biology, 52(4), 361–364.

[13] Mioche, L. (2004). Mastication and Food Texture Perception: Variation with Age. Journal of Texture Studies, 35(2), 145–158.

[14] Oropharynx. (2013). Canine and Feline Gastroenterology, 540–569

[15] Fillmore, E. P., & Seifert, M. F. (2015). Anatomy of the Trigeminal Nerve. Nerves and Nerve Injuries, 319–350.

[16] Salame, T. H., Biomed J Sci & Tech Res (2018). The Role of Mechanoreceptors in and Around the Oral Cavity on Occlusal Function in Overdenture Wearer: A Case Report. Biomedical Journal of Scientific & Technical Research, 5(2).

[17] Cuccia, A., & Caradonna, C. (2009). The relationship between the stomatognathic system and body posture. Clinics, 64(1).

[18] Lugade, V., & Kaufman, K. (2014). Dynamic stability margin using a marker based system and Tekscan: a comparison of four gait conditions. Gait & posture, 40(1), 252–254.

[19] Mastication and cognitive function. (2011). Dental Abstracts, 56(4), 211–214.

[20] Zhao, Y., Wang, W., Xin, H., Zang, S., Zhang, Z., & Wu, Y. (2013). The remodeling of alveolar bone supporting the mandibular first molar with different levels of periodontal attachment. Medical & Biological Engineering & Computing, 51(9), 991–997.

[21] Palareti, G., Legnani, C., Cosmi, B., Antonucci, E., Erba, N.,& Poli, D. (2015). Comparison between different D-Dimer cutoff values to assess the individual risk of recurrent venous thromboembolism: analysis of results obtained in the DULCIS study. International Journal of Laboratory Hematology, 38(1), 42–49.

[22] Maurer, C., Stief, F., Jonas, A., Kovac, A., Groneberg, D. A., Meurer, A., & Ohlendorf, D. (2015). Influence of the Lower Jaw Position on the Running Pattern. PLOS ONE, 10(8)

[23] Okeson, J. (2012). Management of Temporomandibular Disorders and Occlusion.

[24] Regalo, S. C., Santos, C. M., Vitti, M., Regalo, C. A., de Vasconcelos, P. B., Mestriner, W., et al. (2008). Evaluation of molar and incisor bite force in indigenous compared with white population in Brazil. Archives of Oral Biology, 282-286.

[25] Van Der Bilt, A., Tekamp, A., Van Der Glas, H., & Abbink, J. (2008). Bite force and electromyograpy during maximum unilateral and bilateral clenching. European Journal of Oral Sciences, 217-222.

[26] Suzana Varga, Stjepan Spalj, Marina Lapter Varga, Sandra Anic Milosevic, Senka Mestrovic, Mladen Slaj, (2011) Maximum voluntary molar bite force in subjects with normal occlusion, European Journal of Orthodontics, Volume 33, Issue 4, Pages 427–433,

[27] Duyck, J. (2000). Three-dimensional force measurements on oral implants: a Methodological study. Journal of Oral Rehabilitation, 27(9), 744.

[28] Howell, A. H., & Brudevold, F. (1950). Vertical Forces Used During Chewing of Food. Journal of Dental Research, 29(2), 133–136.

[29] Howell, A. H., & Manly, R. S. (1948). An Electronic Strain Gauge for Measuring Oral Forces. Journal of Dental Research, 27(6), 705–712.

[30] Las Casas, E. B. de, Almeida, A. F. de, Cimini Junior, C. A., Gomes, P. de T. V., Cornacchia, T. P. M., & Saffar, J. M. E. (2007). Determination of tangential and normal components of oral forces. Journal of Applied Oral Science, 15(1), 70-6.

[31] Stress Analysis of Hybrid Implant Using Finite Element Method - Scientific Figure on ResearchGate. Available from: https://www.researchgate.net/figure/Type-of-dental-Implant_fig1_245571729 [accessed 20 Sep, 2019]

[32] Reinhardt, B., & Beikler, T. (2014). Dental Implants. Advanced Ceramics for Dentistry, 51–75.

[33] Yenumula, Manikyamba & Sajjan, M C Suresh & Raju, Rama & Professor, A & Rao, Donimukkala & Nair, Chandrasekharan. (2017). Implant thread designs: An overview. 8.

[34] Warreth, Abdulhadi & Ibieyou, Najia & O'Leary, Ronan & Cremonese, Matteo & Abdulrahim, Mohammed. (2017). Dental implants: An overview. Dental Update. 44. 596-620.

[35] Katagiri M. Dental implants. History and tissue reactions of implants [Absrtact]. (1989). Shigaku 77(SPEC):1152-61.

[36] Immediate load implants. Thermal effects during abutment preparation - Scientific Figure on ResearchGate. Available from: https://www.researchgate.net/figure/One-piece-implant-Nobel-Direct-Nobel-Biocare_fig1_265280931 [accessed 20 Sep, 2019]

[37] 3 D-2 D registration of histological images with micro CT volumes using Chamfer Matching and simulated annealing – Scientific Figure on Semantic Scholar. Available from: https://www.semanticscholar.org/ [accessed 20 Sep, 2019]

[38] Rismanchian, M., Bajoghli, F., Gholamreza, T., & Razavi, M. (2014). Dental Implants: Early Versus Standard Two-Stage Loading (Animal Study). Journal of Oral Implantology, 40(1), 84–92.

[39] Svoboda, E.L. (2015). The Evolution from Stock to Custom Abutments Allows for a Better Prosthesis Design that can Control the Gingival Effects and thus the flow of Excess Cement.

[40] Natali, Arturo & Carniel, Emanuele & Pavan, Piero. (2009). Dental implants press fit phenomena: Biomechanical analysis considering bone inelastic response. Dental materials: official publication of the Academy of Dental Materials. 25. 573-81.

[41] Bolind, Pia & Johansson, Carina & Becker, William & Langer, Laureen & Sevetz, Edward & Albrektsson, Tomas. (2005). A descriptive study on retrieved non-threaded and threaded implant designs. Clinical oral implants research. 16. 447-55.

[42] Huang, H.-L., Hsu, J.-T., Fuh, L.-J., Tu, M.-G., Ko, C.-C., & Shen, Y.-W. (2008). Bone stress and interfacial sliding analysis of implant designs on an immediately loaded maxillary implant: A non-linear finite element study. Journal of Dentistry, 36(6), 409–417.

[43] Misch, C. E., Strong, J. T., & Bidez, M. W. (2015). Scientific Rationale for Dental Implant Design. Dental Implant Prosthetics, 340–371.

[44] Strong JT, Misch CE, Bidez MW, et al (1998). Functional surface area: thread form parameter optimization for implant body design. Compend Contin Educ Dent 19:4–9.

[45] Bahat, O. (1993). Treatment planning and placement of implants in the posterior maxillae: report of 732 consecutive Nobelpharma implants. The International journal of oral & maxillofacial implants, 8 2, 151-61 .

[46] Duraisamy, Velmurugan. (2017). Dental Implant Materials, Implant Design, And Role Of Fea-A Brief Review. Journal of Evolution of Medical and Dental Sciences. 6.

[47] Olate, Sergio & Lyrio, Mariana & Moraes, Márcio & Mazzonetto, Renato & Moreira, Roger. (2010). Influence of Diameter and Length of Implant on Early Dental Implant Failure. Journal of oral and maxillofacial surgery : official journal of the American Association of Oral and Maxillofacial Surgeons. 68. 414-9.

[48] Spiekermann, H., Jansen, V.K., & Richter, E. (1995). A 10-year follow-up study of IMZ and TPS implants in the edentulous mandible using bar-retained overdentures. The International journal of oral & maxillofacial implants, 10(2), 231-43 .

[49] Andersen, E.E., Saxegaard, E., Knutsen, B.M., & Haanaes, H.R. (2001). A prospective clinical study evaluating the safety and effectiveness of narrow-diameter threaded implants in the anterior region of the maxilla. The International journal of oral & maxillofacial implants, 16(2), 217-24 .

[50] Ozdiler, A., Bakir-Topcuoglu, N., Kulekci, G., & Isik-Ozkol, G. (2018). Effects of Taper Angle and Sealant Agents on Bacterial Leakage Along the Implant-Abutment Interface: An In Vitro Study Under Loaded Conditions. The International Journal of Oral & Maxillofacial Implants.

[51] El-Gendy, A. M., Nassar, M. M., & Saudi, H. I. (2014) Immediate hollow versus solid screw implants augmented with bone graft in the extracted socket of hemisected mandibular molars: Clinical and radiographic study. Tanta Dental Journal, 11(1), 56-62.

[52] Telleman, Gerdien & Meijer, Henny & Raghoebar, Gerry. (2006). Long-Term Evaluation of Hollow Screw and Hollow Cylinder Dental Implants: Clinical and Radiographic Results After 10 Years. Journal of periodontology. 77. 203-10.

[53] Kim, Do-Gyoon & Kim, Kyoung-Hwa & Jo, YeHyeon & Lee, Jue & Park, Yoon & Chung, Chong & Seol, Yang-Jo & Han, Jung-Suk. (2019). Bone regeneration into side openings and hollow inner channel of a dental implant. Journal of the Mechanical Behavior of Biomedical Materials.

[54] Dental implants-associated release of titanium particles: A systematic review. Scientific Figure on ResearchGate. Available from: https://www.researchgate.net/ [accessed 20 Sep, 2019]

[55] Sadaqah, Nasrin & Al-Wahadni, Ahed & Alhaija, Elham. (2010). Implant Abutment Types: A Literature Review – Part 1.

[56] Influence of the implant-abutment connection design and diameter on the screw joint stability - Scientific Figure on ResearchGate. Available from: www.researchgate.net [accessed 20 Sep, 2019]

[57] Comparison of Angled and Standard Abutments and Their Effect on Clinical Outcomes: A Preliminary Report – Scientific Figure on Semantic Scholar. Available from https://www.semanticscholar.org [accessed 20 Sep, 2019]

[58] Clelland, N.L., Gilat, A.L., Mcglumphy, E.A., & Brantley, W.A. (1993). A photoelastic and Strain gauge analysis of angled abutments for an implant system. The International journal of oral & maxillofacial implants, 8 5, 541-8.

[59] Sethi, A., Kaus, T.M., & Sochor, P. (2000). The use of angulated abutments in implant dentistry: five-year clinical results of an ongoing prospective study. The International journal of oral & maxillofacial implants, 15(6), 801-10 .

[60] Yildirim, M., Fischer, H., Marx, R., & Edelhoff, D. (2003). In vivo fracture resistance of implant supported ceramic restorations. Journal of prosthetic dentistry, 90(4), 325-31.

[61] Van Staden, R. C., Guan, H., & Loo, Y. C. (2006). Application of the finite element method in dental implant research. Computer Methods in Biomechanics and Biomedical Engineering, 9(4), 257–270

[62] Alper, B., Gultekin, P., & Yalci, S. (2012). Application of Finite Element Analysis in Implant Dentistry. Finite Element Analysis - New Trends and Developments

[63] Van Oosterwyck H, Duyck J, Vander Sloten J, Van der Perre G, De Cooman M, Lievens S, et al. (1998) The influence of bone mechanical properties and implant fixation upon bone loading around oral implants. Clin Oral Implants Res. 9(6), 407-18.

[64] Rieger MR, Mayberry M, Brose MO. (1990) Finite element analysis of six endosseous implants. J Prosthet Dent. 63, 671-6

[65] Meijer GJ, Starmans FJM, de Putter C, van Blitterswijk CA. (1995) The influence of a flexible coating on the bone stress around dental implants. J Oral Rehabil; 22:105-11.

[66] Sertgöz A. (1997) Finite element analysis study of the effect of superstructure material on stress distribution in an implant-supported fixed prosthesis. Int J Prosthodont;10:19-27

[67] Geng, J.-P., Tan, K. B. C., & Liu, G.-R. (2001). Application of finite element analysis in implant dentistry: A review of the literature. The Journal of Prosthetic Dentistry, 85(6), 585–598.

[68] Heckmann, Siegfried & Karl, Matthias & Wichmann, Manfred & Winter, Werner & Graef, Friedrich & Taylor, Thomas. (2006). Loading of bone surrounding implants through three-unit fixed partial denture fixation: A finite-element analysis based on in vitro and in vivo strain measurements. Clinical oral implants research. 17. 345-50.

[69] Nagasao T, Miyamoto J, Jin H, Tamaki T, Isshiki Y, Kaneko T, et al. (2006) The dynamics in implantation for patients with clefts. Cleft Palate Craniofac J. 43:84–91.

[70] Ozçelik T, Ersoy AE. (2007) An investigation of tooth/implant-supported fixed prosthesis designs with two different stress analysis methods: an in vitro study. J Prosthodont. 16:107–116.

[71] Lin CL, Lin YH, Chang SH. (2010) Multi-factorial analysis of variables influencing the bone loss of an implant placed in the maxilla: prediction using FEA and SED bone remodeling algorithm. J Biomech. 43:644–651.

[72] Lin CL, Lin YH, Chang SH. (2010) Multi-factorial analysis of variables influencing the bone loss of an implant placed in the maxilla: prediction using FEA and SED bone remodeling algorithm. J Biomech. 43:644–651.

[73] Hasan I, Röger B, Heinemann F, Keilig L, Bourauel C. (2012) Influence of abutment design on the success of immediately loaded dental implants: experimental and numerical studies. Med Eng Phys. 34:817–825.

[74] Desai, S.R., Desai, M.S., Katti, G., & Karthikeyan, I. (2012). Evaluation of design parameters of eight dental implant designs: a two-dimensional finite element analysis. Nigerian journal of clinical practice, 15(2), 176-81.

[75] Inglam S, Chantarapanich N, Suebnukarn S, Vatanapatimakul N, Sucharitpwatskul S, Sitthiseripratip K. (2013) Biomechanical evaluation of a novel porous-structure implant: finite element study. Int J Oral Maxillofac Implants. 28: 48–56.

[76] Huang, Y., Chou, I., Jiang, C., Wu, Y., & Lee, S. (2014). Finite element analysis of dental implant neck effects on primary stability and osseointegration in a type IV bone mandible. Bio-medical materials and engineering, 24(1), 1407-15.

[77] Rezende CE, Chase-Diaz M, Costa MD, Albarracin ML, Paschoeto G, Sousa EA, et al. (2015) Stress distribution in single dental implant system: three-dimensional finite element analysis based on an in vitro experimental model. J Craniofac Surg. 26:2196–2200.

[78] Zhang, G., Yuan, H., Chen, X., Wang, W., Chen, J., Liang, J., & Zhang, P. (2016). A Three-Dimensional Finite Element Study on the Biomechanical Simulation of Various Structured Dental Implants and Their Surrounding Bone Tissues. International Journal of Dentistry, 2016, 1–9.

[79] Chang SH, Huang SR, Huang SF, Lin CL. (2016) Mechanical response comparison in an implant overdenture retained by ball attachments on conventional regular and mini dental implants: a finite element analysis. Comput Methods Biomech Biomed Engin. 19: 911–921.

[80] Cicciù, Marco & Cervino, Gabriele & Milone, Dario & Risitano, Giacomo. (2018). FEM Investigation of the Stress Distribution over Mandibular Bone Due to Screwed Overdenture Positioned on Dental Implants. Materials. 11.

[81] Moeen, F., & Nisar, S. (2014). A Step By Step Guide To Finite Element Analysis In Dental Implantology.

[82] Chang, H.-S., Chen, Y.-C., Hsieh, Y.-D., & Hsu, M.-L. (2013). Stress distribution of two commercial dental implant systems: A three-dimensional finite element analysis. Journal of Dental Sciences, 8(3), 261–271.

[83] Topkaya, Tolga & Solmaz, Murat & Dundar, Serkan & Eltas, Abubekir. (2015). Numerical analysis of the effect of implant geometry to stress distributions of the three different commercial dental implant system. Cumhuriyet Dental Journal. 18.

[84] Liang, R., Guo, W., Qiao, X., Wen, H., Yu, M., Tang, W., … Tian, W. (2014). Biomechanical analysis and comparison of 12 dental implant systems using 3D finite element study. Computer Methods in Biomechanics and Biomedical Engineering, 18(12), 1340–1348.

[85] Hisam, M. J., Lim, J. Y., Kurniawan, D., & Nor, F. M. (2015). Stress Distribution Due to Loading on Premolar Teeth Implant: A Three Dimensional Finite Element Analysis. Procedia Manufacturing, 2, 218–223.

[86] Jalali, S. K., Yarmohammadi, R., & Maghsoudi, F. (2016). Finite element stress analysis of functionally graded dental implant of a premolar tooth. Journal of Mechanical Science and Technology, 30(11), 4919–4923.

[87] Dhatrak, P., Shirsat, U., Sumanth, S., & Deshmukh, V. (2018). Finite Element Analysis and Experimental Investigations on Stress Distribution of Dental Implants around Implant-Bone Interface. Materials Today: Proceedings, 5(2), 5641–5648.

[88] Aumnakmanee, S., Yodpiji, N., Jantong, N., & Jongprasithporn, M. (2018). Finite element analysis of dental implant prosthetics. Materials Today: Proceedings, 5(3), 9525–9534

[89] Shash, M., Nazha, H., & Abbas, W. (2019). Influence of Different Abutment Designs on the Biomechanical Behavior of One-Piece Zirconia Dental Implants and Their Surrounding Bone: A 3D-FEA. IRBM.

[90] García-Braz, Prados-Privado, Zanatta, Calvo-Guirado, Prados-Frutos, & Gehrke. (2019). A Finite Element Analysis to Compare Stress Distribution on Extra-Short Implants with Two Different Internal Connections. Journal of Clinical Medicine, 8(8), 1103.

[91] Zhou X, Zhao Z, Zhao M, Fan Y (1999) The boundary design of mandibular model by means of the three dimensional finite element method. Hua Xi Kou Qiang Yi Xue Za Zhi.17(1):29-32.

[92] Teixeira, E. R., Sato, Y., Akagawa, Y., & Shindoi, N. (1998). A comparative evaluation of mandibular finite element models with different lengths and elements for implant biomechanics. Journal of Oral Rehabilitation, 25(4)

[93] Cheng, Y., Lin, D., Jiang, C., & Lee, S. (2015). Design improvement and dynamic finite element analysis of novel ITI dental implant under dynamic chewing loads. Bio-medical materials and engineering, 26 Suppl 1, S555-61.

[94] Chen, L. (2012). Finite Element Analysis of the Stress on the Implant-Bone Interface of Dental Implants with Different Structures. Finite Element Analysis - New Trends and Developments.

[95] Nemati, S., & Khorramymehr, S. (2019). Three Dimensional Evaluation of a Dental Implant in Different Angles by Finite Element Method.

[96] Cheng, Y., Jiang, C., & Lin, D. (2019). Finite element based optimization design for a one-piece zirconia ceramic dental implant under dynamic loading and fatigue life validation. Structural and Multidisciplinary Optimization, 59, 835-849.

[97] Staden, Rudi & Loo, Yew-Chaye & Johnson, Newell & Ivanovski, Saso & Meredith, Neil. (2009). Influence of Bone and Dental Implant Parameters on Stress Distribution in the Mandible: A Finite Element Study. The International journal of oral & maxillofacial implants. 24. 866-76.

[98] Eskitascioglu, G., Usumez, A., Sevimay, M., Soykan, E., & Unsal, E. (2004). The influence of occlusal loading location on stresses transferred to implant-supported prostheses and supporting bone: a three-dimensional finite element study. The Journal of Prosthetic Dentistry, 91(2), 144–150.

[99] Massoumi, F., Taheri, M., Mohammadi, A., & Amelirad, O. (2018). Evaluation of the Effect of Buccolingual and Apicocoronal Positions of Dental Implants on Stress and Strain in Alveolar Bone by Finite Element Analysis. Journal of dentistry (Tehran, Iran), 15(1), 10–19.

[100] Jafarian, M., Mirhashemi, F.S., & Emadi, N. (2019). Finite element analysis of stress distribution around a dental implant with different amounts of bone loss: An in vitro study. Dental and medical problems, 56(1), 27-32.

[101] Chu CM, Huang H L, Hsu JT, Fuh LJ. (2012) Influences of internal tapered abutment designs on bone stresses around a dental implant: three-dimensional finite element method with statistical evaluation. J Periodontol. 83: 111-18.

[102] Jörn, Daniela & Kohorst, Philipp & Besdo, Silke & Rücker, Martin & Stiesch, Meike & Borchers, Lothar. (2014). Influence of lubricant on screw preload and stresses in a finite element model for a dental implant. The Journal of prosthetic dentistry. 112

[103] Mahajan, S.S., & Patil, P.R. (2016). Application of finite element analysis to optimizing dental implant

[104] Kim, W. H., Lee, J.-C., Lim, D., Heo, Y.-K., Song, E.-S., Lim, Y.-J., & Kim, B. (2019). Optimized Dental Implant Fixture Design for the Desirable Stress Distribution in the Surrounding Bone Region: A Biomechanical Analysis. Materials, 12(17), 2749

[105] Chun, Heoung-Jae & Shin, Ha-Shik & Han, Chong-Hyun & Lee, Soo-Hong. (2005). Influence of implant abutment type on stress distribution in bone under various loading conditions using finite element analysis. The International journal of oral & maxillofacial implants. 21. 195-202.

[106] Pakdel, Z. (2007). Characterization, Modeling of Piezoelectric Pressure Transducer for Facilitation of Field Calibration.

[107] Button, V. L. D. S. N. (2015). Pressure and Force Transducers. Principles of Measurement and Transduction of Biomedical Variables, 221–270

[108] Puers, R. (1993). Capacitive sensors: When and how to use them. Sensors and Actuators A: Physical, 37-38, 93–105.

[109] Nie, M., Bao, H., & Huang, Q.-A. (2015). Capacitive Pressure Sensors. Wiley Encyclopedia of Electrical and Electronics Engineering, 1–13

[110] Pritchard, E., Mahfouz, M., Evans, B., Eliza, S., & Haider, M. (2008). Flexible capacitive sensors for high resolution pressure measurement. 2008 IEEE Sensors.

[111] Regtien, P. P. L., & Dertien, E. C. (2018). Sensors for Mechatronics 2nd edition. (2 ed.) Amsterdam: Elsevier.

[112] Meti, Shwetha & Balavalad, Kirankumar & Sheeparamatti, Basavaprabhu. (2016). MEMS Piezoresistive Pressure Sensor: A Survey. IJERA. 6.

[113] Zhang, P. (2010). Sensors and actuators. Advanced Industrial Control Technology, 73-116.

[114] A new approach for error minimization of piezoelectric sensor output variations using fuzzy logic - Scientific Figure on ResearchGate. Available from: https://www.researchgate.net/figure/Block-diagram-of-Piezoelectric-Sensor_fig1_283021198 [accessed 11 Oct, 2019]

[115] Tadigadapa, S., & Mateti, K. (2009). Piezoelectric MEMS sensors: state-of-the-art and perspectives.

[116] Kutiš, V., Dzuba, J., Paulech, J., Murín, J., & Lalinský, T. (2012). MEMS Piezoelectric Pressure Sensor-modelling and Simulation. Procedia Engineering, 48, 338–345.

[117] Pooja A N, Dr. Bindu A Thomas (2018). Design And Comparison of Piezoelectric High Pressure Sensor by using COMSOL Multiphysics, International Journal Of Engineering Research & Technology (IJERT) 6(13)

[118] Kim, W., Song, E., Ju, K., Lee, J.-H., Kim, M., Lim, D., & Kim, B. (2019). Finite Element Analysis of Novel Separable Fixture for Easy Retrievement in Case with Peri-mplantitis. Materials, 12(2), 235.

Annex I – Dynamic load configuration

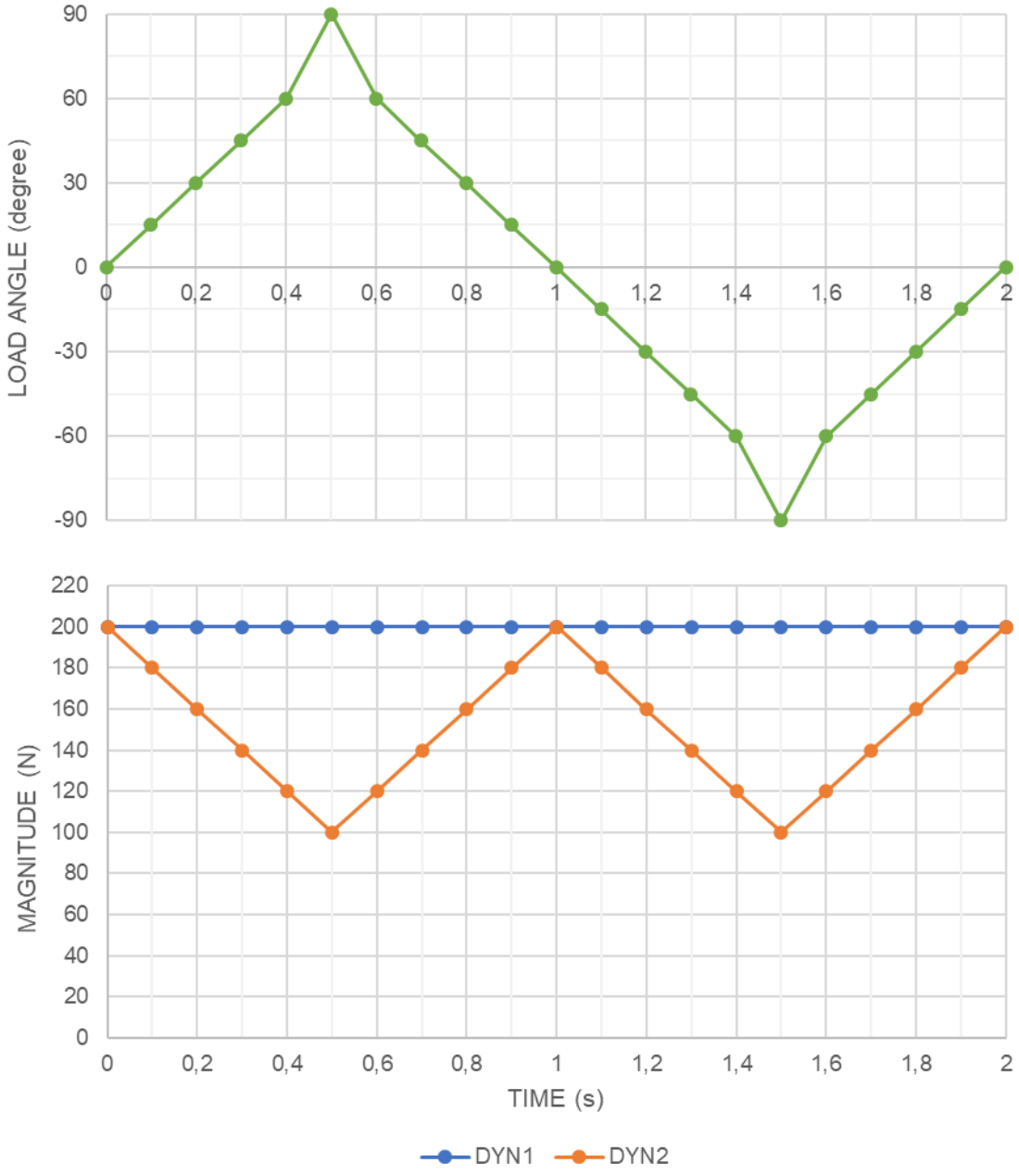

Figure I.1. Dynamic loads configuration used in this work to simulate mastication. (*above*) Dynamic load 1 (DYN_1) and dynamic load 2 (DYN_2) have the same angle variation in time. (*below*) DYN_1 has a static magnitude of 200 N, whereas DYN_2 magnitude is maximal for 0º load angle and decreases to one half at ±90º.

Annex II – Average absolute compressive stress at the points of interest

II.1 AVGAC stress *versus* point of interest plots

II.1.1 Bottom points of interest

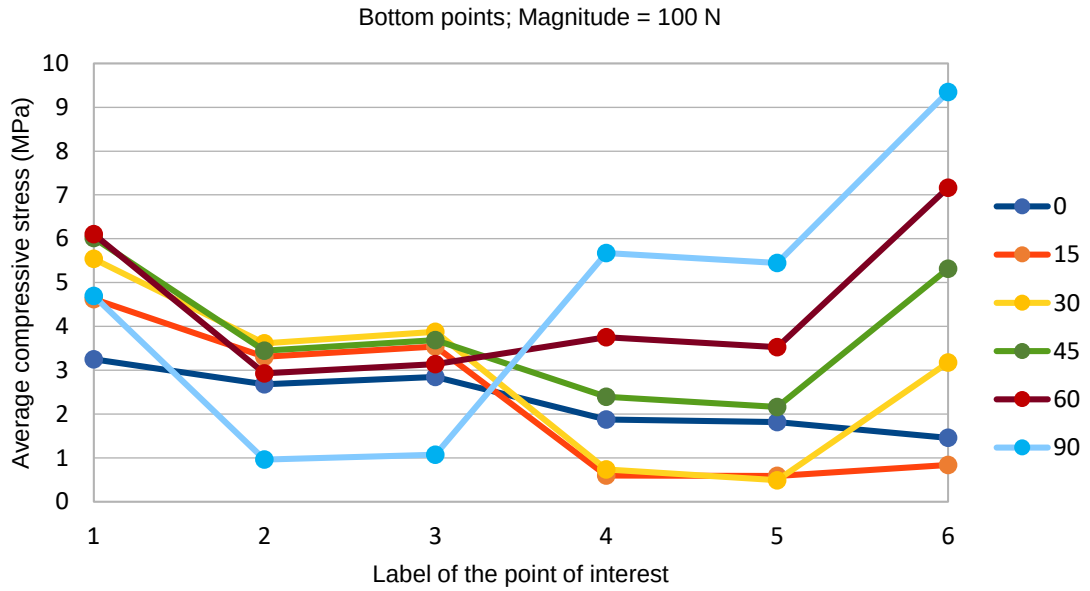

Figure II.1. AVGAC stress at the bottom points of interest under a 100 N load at different angles. Load angles are displayed on the right in degrees.

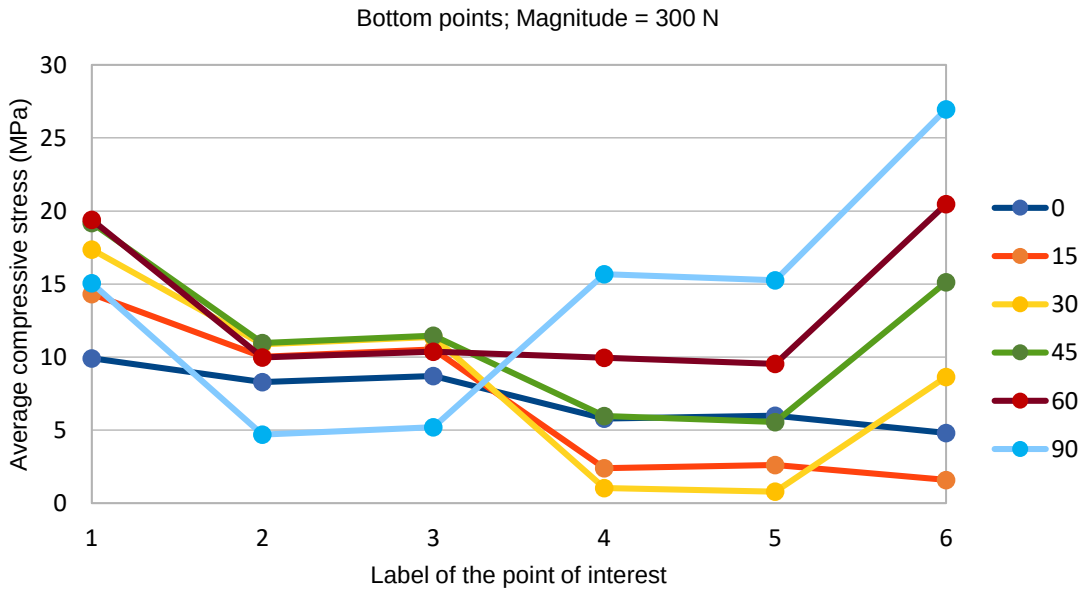

Figure II 2. AVGAC stress at the bottom points of interest under a 300 N load at different angles. Load angles are displayed on the right in degrees.

II.1.2 Top points of interest

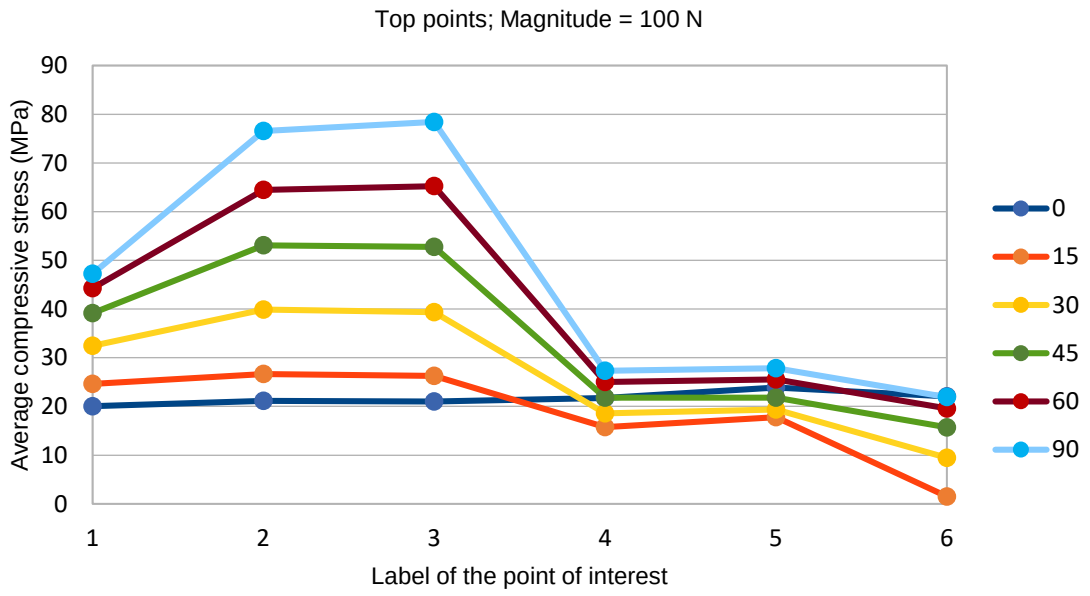

Figure II.2. AVGAC stress at the top points of interest under a 100 N load at different angles. Load angles are displayed on the right in degrees.

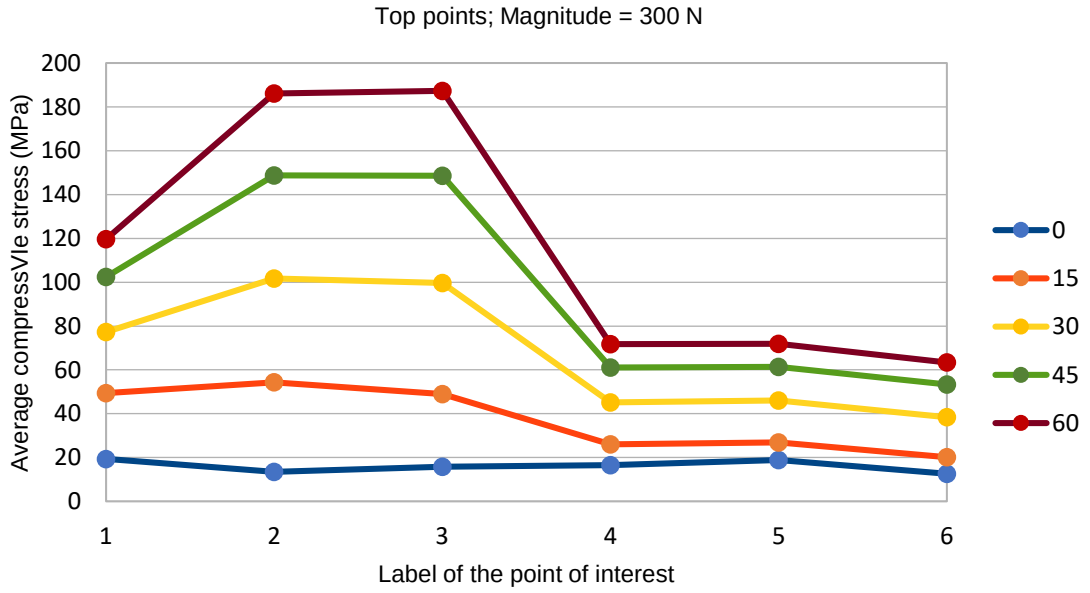

Figure II.3. AVGAC stress at the top points of interest under a 300 N load at different angles. Load angles are displayed on the right in degrees.

II.2 AVGAC stress *versus* load angle plots

II.2.1 Bottom points of interest

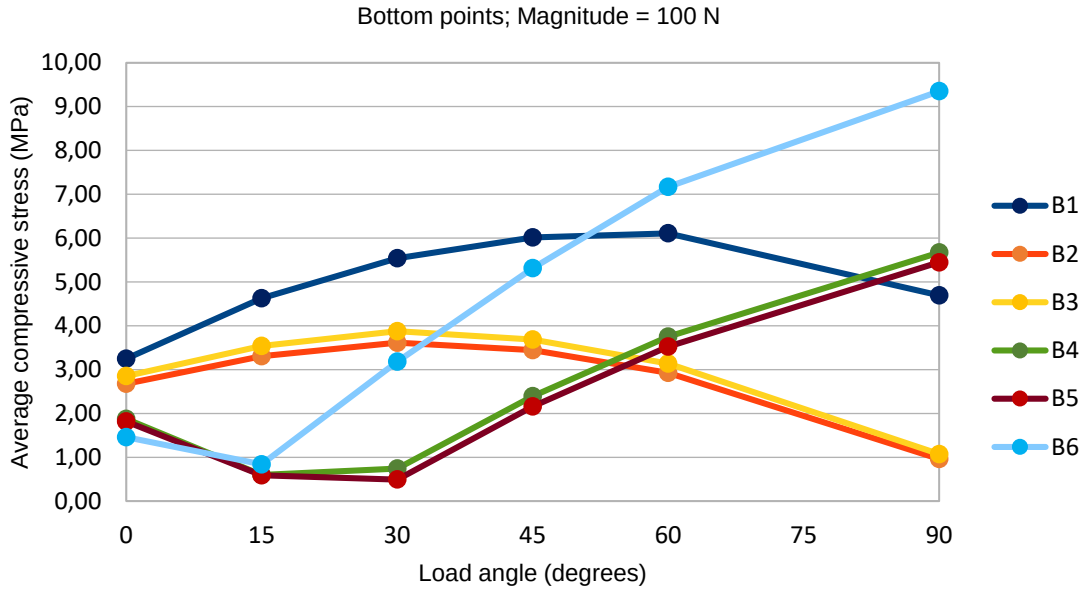

Figure II.5. Variation of the AVGAC stress with the load angle under a 100 N load for the bottom points. Labels of the points are displayed on the right.

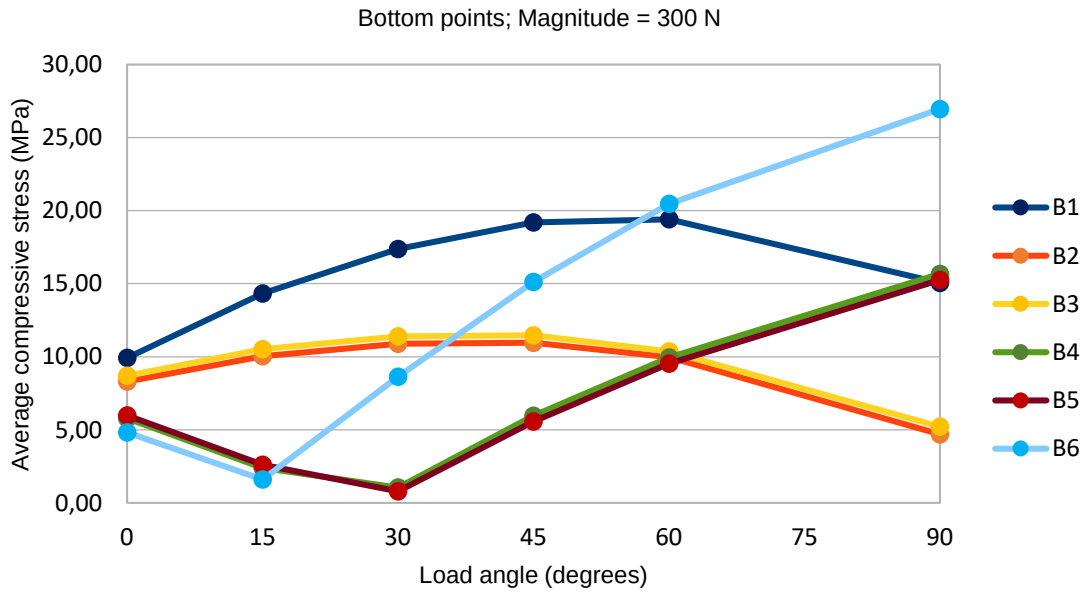

Figure II.6. Variation of the AVGAC stress with the load angle under a 300 N load for the bottom points. Labels of the points are displayed on the right.

II.2.2 Top points of interest

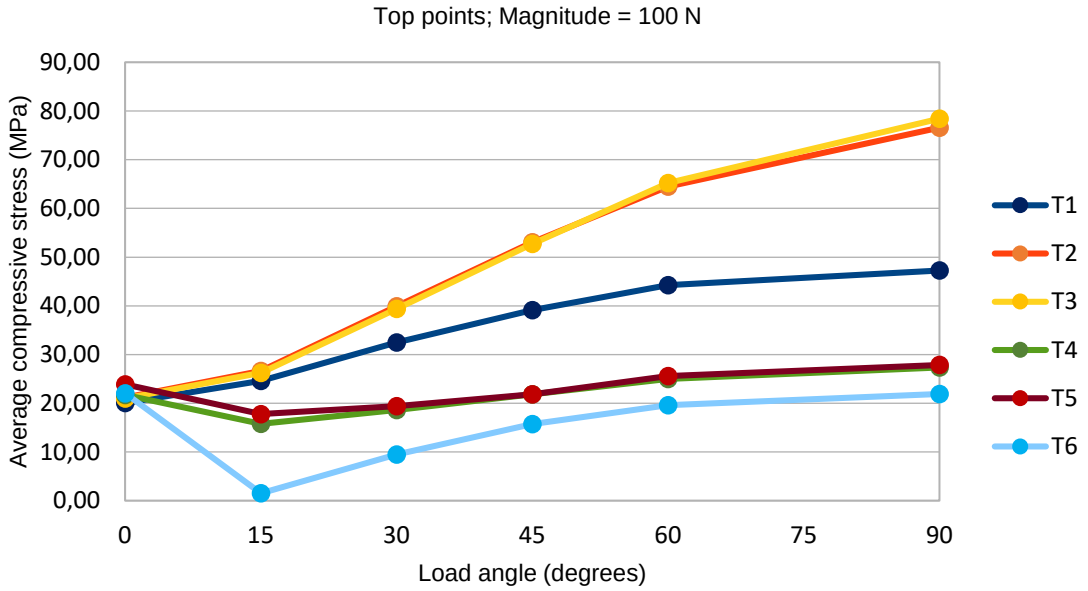

Figure II.7. Variation of the AVGAC stress with the load angle under a 100 N load for the top points. Labels of the points are displayed on the right.

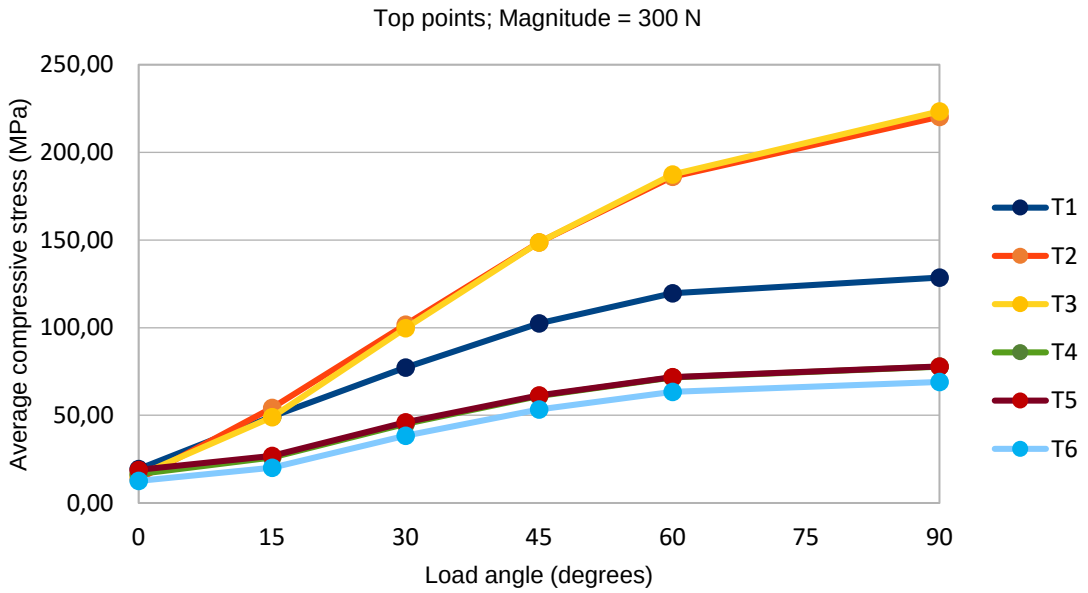

Figure II.8. Variation of the AVGAC stress with the load angle under a 300 N load for the bottom points. Labels of the points are displayed on the right.

Annex III – Maximum absolute principal stress at the points of interest

III.1 Max absolute principal stress *versus* point of interest plots

III.1.1 Bottom points of interest

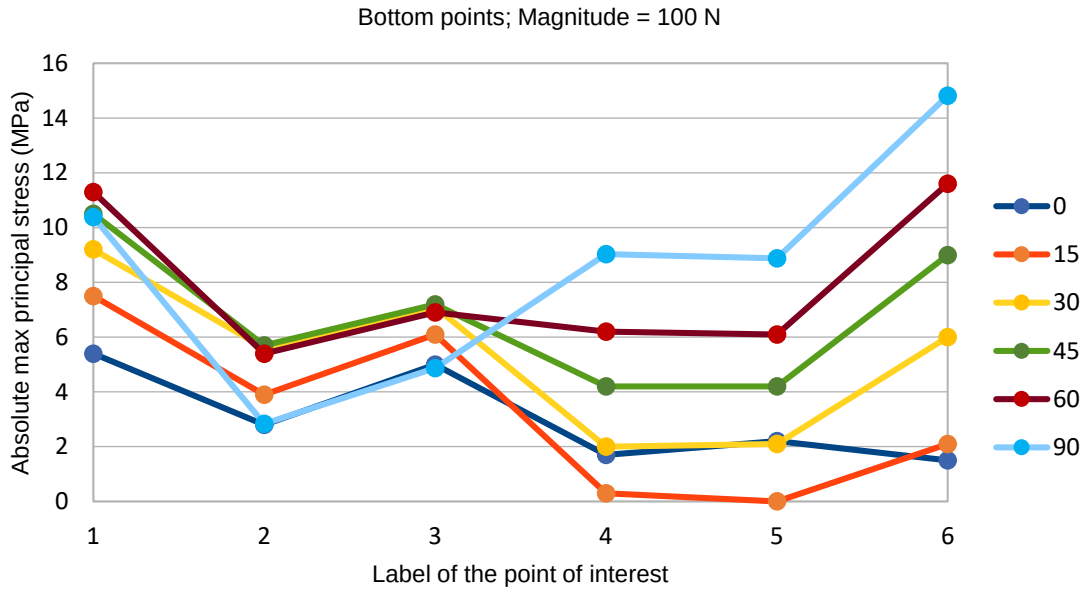

Figure III.1. Max absolute principal stress at the bottom points of interest under a 100 N load at different angles. Load angles are displayed on the right in degrees.

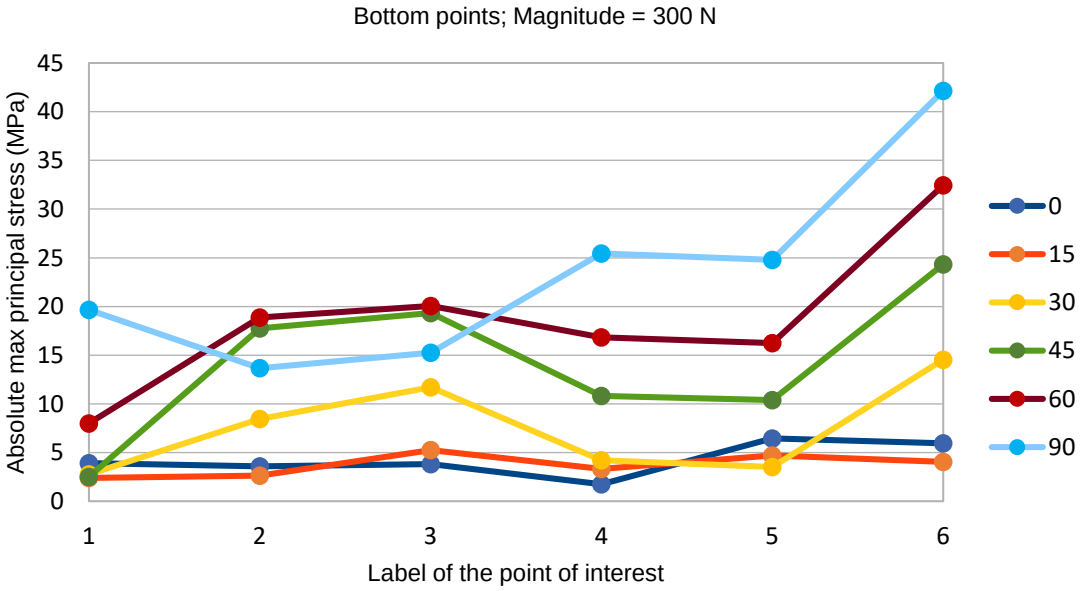

Figure III.2. Max absolute principal stress at the bottom points of interest under a 300 N load at different angles. Load angles are displayed on the right in degrees.

III.1.2 Top points of interest

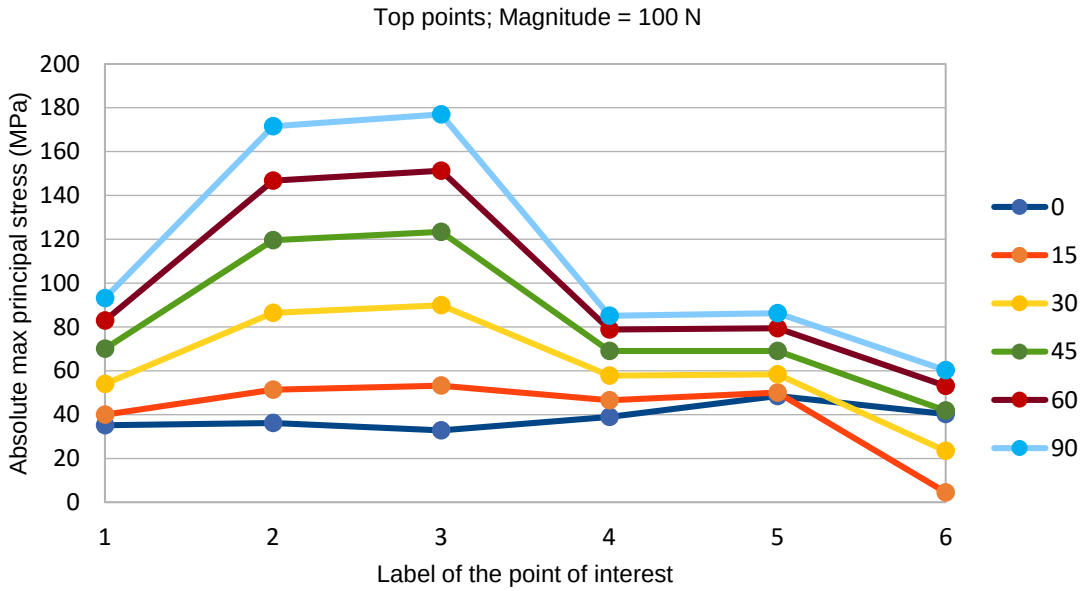

Figure III.3. Max absolute principal stress at the top points of interest under a 100 N load at different angles. Load angles are displayed on the right in degrees.

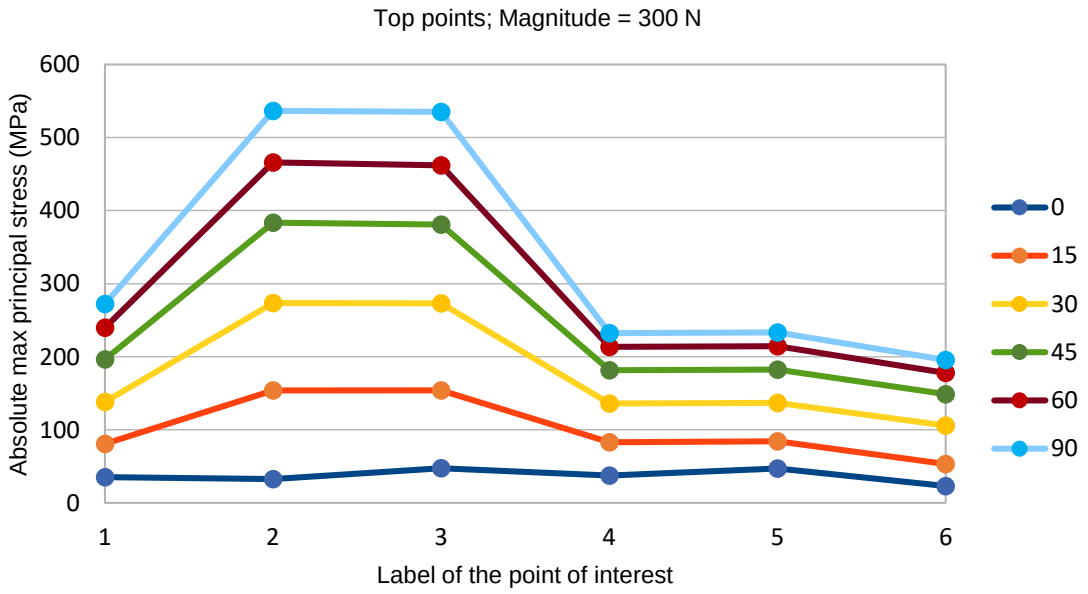

Figure III.4. Max absolute principal stress at the top points of interest under a 300 N load at different angles. Load angles are displayed on the right in degrees.

III.2 Max absolute principal stress *versus* load angle plots

III.2.1 Bottom points of interest

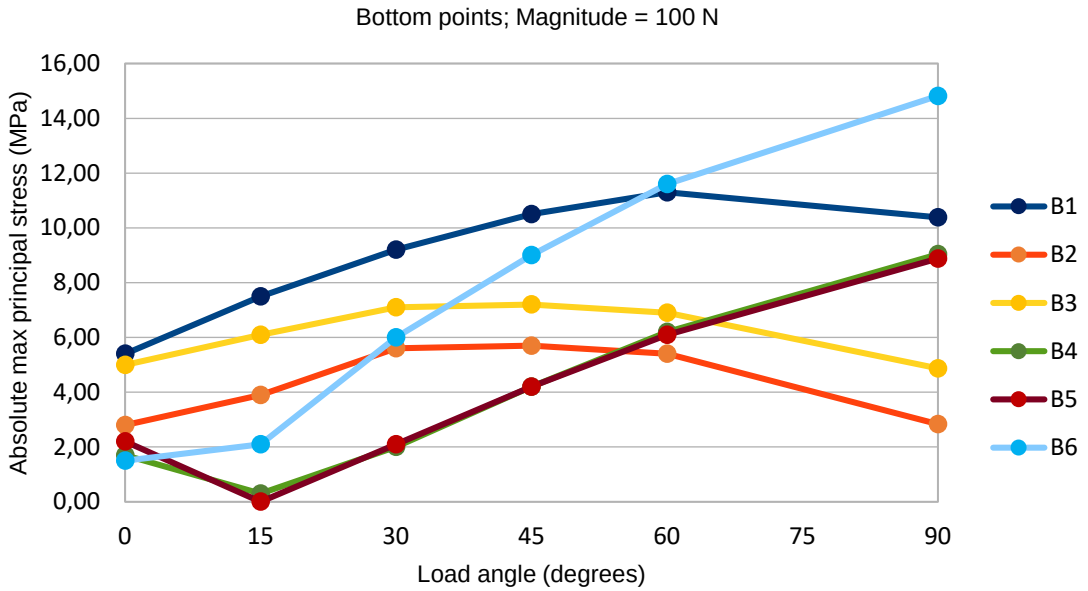

Figure III.5. Variation of the max absolute principal stress with the load angle under a 100 N load for the bottom points. Labels of the points are displayed on the right.

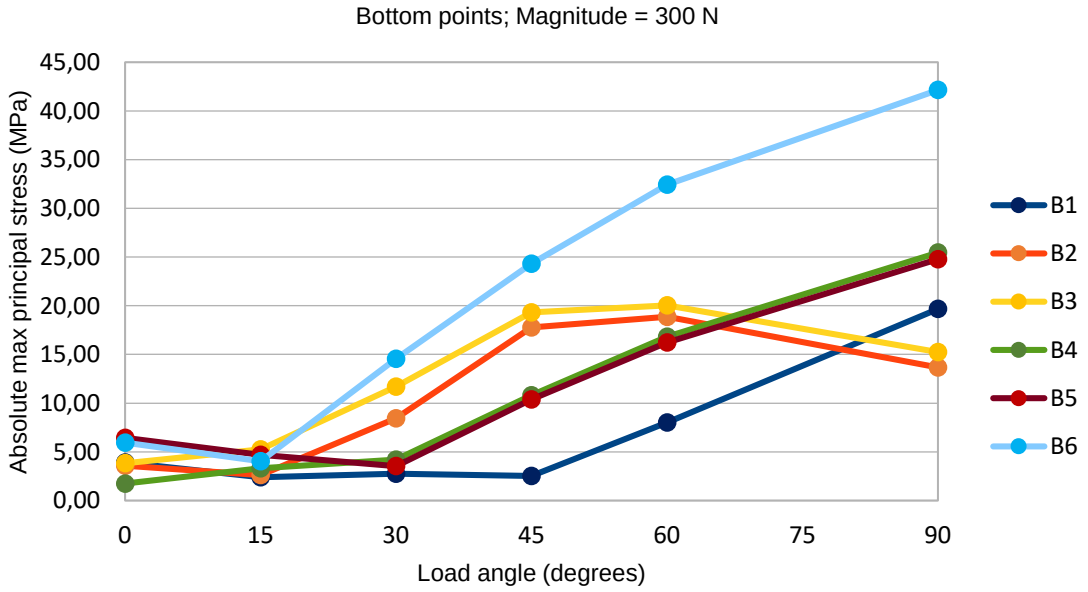

Figure III.6. Variation of the max absolute principal stress with the load angle under a 300 N load for the bottom points. Labels of the points are displayed on the right.

III.2.2 Top points of interest

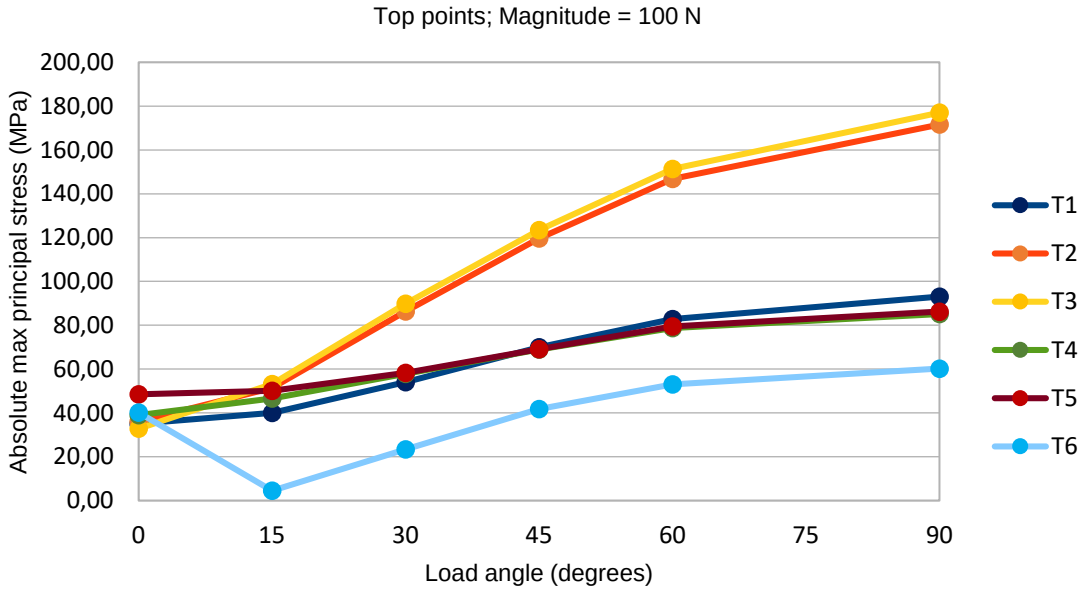

Figure III.7. Variation of the max absolute principal stress with the load angle under a 100 N load for the top points. Labels of the points are displayed on the right.

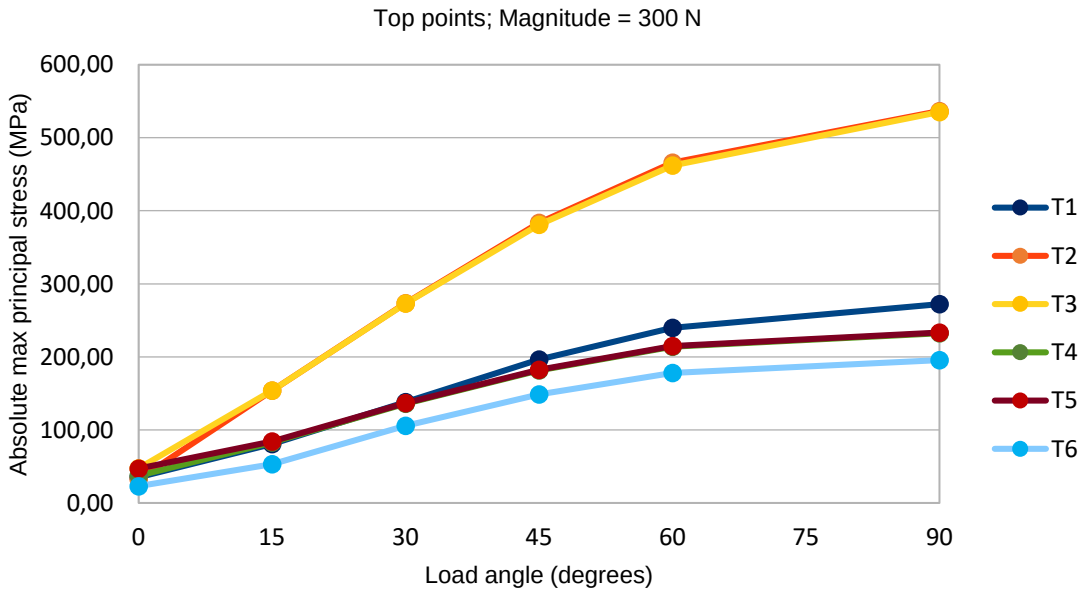

Figure III.8. Variation of the max absolute principal stress with the load angle under a 300 N load for the bottom points. Labels of the points are displayed on the right.